THE EFFECT OF CHANNELING ON THE DRYOUT OF HEATED PARTICULATE BEDS IMMERSED IN A LIQUID POOL

by

ALFRED WALTERS REED

B.S., University of New Mexico
(1974)

M.S., University of New Mexico
(1976)

SUBMITTED TO THE DEPARTMENT OF MECHANICAL ENGINEERING IN PARTIAL FULFILLMENT OF THE REQUIREMENTS FOR THE DEGREE OF

DOCTOR OF PHILOSOPHY

at the

MASSACHUSETTS INSTITUTE OF TECHNOLOGY

February 1982

Signature of Author_____
Department of Mechanical Engineering
January 6, 1982

Certified by_____
Warren M. Rohsenow
Thesis Supervisor

Accepted by_____
Warren M. Rohsenow
Chairman, Department Committee

THE EFFECT OF CHANNELING ON THE DRYOUT OF HEATED PARTICULATE BEDS IMMERSED IN A LIQUID POOL

by

ALFRED WALTERS REED

Submitted to the Department of Mechanical Engineering
on January 6, 1982 in partial fulfillment of the
requirements for the Degree of Doctor of Philosophy in
Mechanical Engineering

ABSTRACT

A loss-of-flow accident in a liquid metal fast breeder reactor could cause the formation of a bed of fuel and steel particles immersed in liquid sodium. Under certain conditions, decay heat from the uranium oxide fuel can dry out the bottom of the bed and subsequently melt the fuel-steel matrix. The conditions leading to dryout are of interest.

A two region model to predict dryout is proposed. The equations of two phase flow in porous media are used to describe the flow in the bottom of the bed. The depth of the upper channeled region and the flow description therein are derived from the principles of soil mechanics. Experimental data confirms the prediction of channel depth.

Predictions of the model are compared to existing dryout data. Uncertainties in the model are discussed as well as projected difficulties in the experimental determination of dryout.

Thesis Supervisor: Dr. Warren M. Rohsenow
Title: Professor of Mechanical Engineering

ACKNOWLEDGEMENTS

My thanks go to my advisors, Professors Warren M. Rohsenow, Peter Griffith, and Mujid Kazimi for their suggestions, guidance, and friendship.

I am also grateful for the friendship of Dr. John Bowan, Dr. Foster Nickerson, Dr. Andre By, Dr. Wayne Hill, and Dr. Chris Calia.

Special thanks go to Dr. Lawrence Hull for his participation in the technical arguments and beer drinking which made this thesis possible.

This work was made possible by Sandia National Laboratories.

DEDICATION

To my Parents who taught me to ask and work

To Mommoo who taught me to read

To Gramps and Grandmother who taught me to see

TABLE OF CONTENTS

LIST OF FIGURES

NOMENCLATURE

Symbol	Meaning	Units
A	area	m^2
$\bar{d}$	average particle diameter	m
g	gravitational constant	m/s^2
h	channel depth	m
h_{f_g}	enthalpy of evaporation	J/kg
k	laminar permeability	m^2
k_ℓ	laminar relative permeability of liquid	
k_v	laminar relative permeability of vapor	
K	stress ratio of vapor	
$\underline{K}$	thermal conductivity	W/m-K
ℓ	liquid	
L	height of porous bed	m
P	pressure	Pa
P_c	capillary pressure	Pa
P	dimensionless capillary pressure	
$\underline{P}(R)$	radius population distribution	m^{-1}
q	superficial velocity	m/s
$\dot{q}$	heat flux	W/m^2
$\ddot{q}$	volumetric heat generation	W/m^3
R	radius	m
S	saturation = $\frac{\text{Volume of liquid}}{\text{Volume of non-solid}}$	
S_e	effective saturation	

Symbol	Meaning	Units
v	vapor	
V	velocity	m/s
z	vertical distance	m
ε	void fraction	
η	dimensionless vertical distance	
κ	turbulent permeability	m
κ_ℓ	turbulent relative permeability of liquid	
κ_v	turbulent relative permeability of vapor	
μ	absolute viscosity	Ns/m^2
ν	kinematic viscosity	m^2/s
Π	dimensionless group	
ρ	density	kg/m^3
τ	tortuosity	
σ	surface tension	N/m
σ_v	vertical stress	N/m^2
σ_h	horizontal stress	N/m^2

I. INTRODUCTION

Accident Scenario

One hypothetical core disruptive accident (HCDA) which is postulated for liquid metal fast feeder reactors (LMFBR) starts with a failure of power to the pumps.[1,2] The resultant loss of flow (LOF) is accompanied by a failure of the safety system to scram the reactor. Under such a combination of conditions, a large scale core meltdown would be possible.

The meltdown would be preceded by boiling of the sodium coolant in the core. This would drive most of the coolant from the core into the upper and lower plenums (Fig. 1). The fuel would continue to increase in temperature past its melting point until it started to boil. The vapor pressure of the boiling fuel-steel mixture would increase, driving the molten mixture from the core into the upper and lower plenums where it would contact the liquid sodium.

It has been experimentally determined[3,4] that small particles of solid fuel are formed when molten fuel is quenched in liquid sodium. The particles range in diameter from about 100 μm to greater than 1000 μm. In the accident scenario under consideration, these particles would sink through the liquid sodium, settle on the horizontal surfaces of the plenums, and form an unconsolidated matrix of liquid sodium and solid fuel/steel particles known as a debris bed.

The fuel particles in the debris bed would still produce decay heat. If the fuel particles stay below the fuel melting point, then the configuration is assumed to be stable and the accident scenario ends.

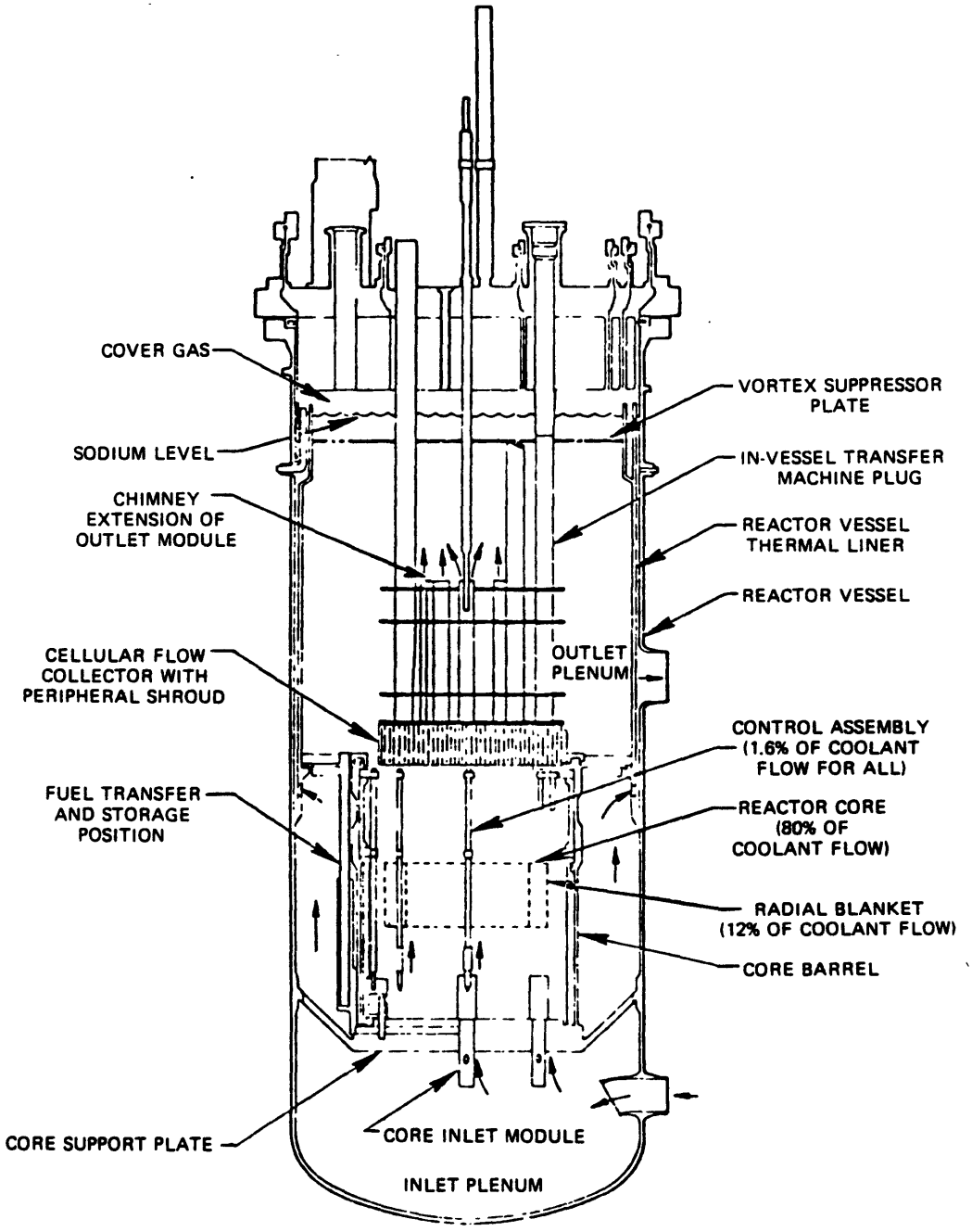

Fig. 1. Schematic diagram for the Clinch River Breeder Reactor (CRBR) (Ref. 1)

If the fuel particles melt, then the plenum may be penetrated, and the accident scenario continued. Knowledge of the conditions leading to melting of the fuel particles is therefore necessary for an analytical evaluation of this hypothetical accident.

The melting point of uranium fuel is much greater than the boiling point of sodium. Therefore, the presence of liquid sodium at a particular level in the debris bed implies that the fuel is still solid at that level. Until recently, the complement has also been assumed; in the absence of significant sodium vapor velocities, heat conduction through a dry debris bed cannot adequately cool the fuel particles. For a debris bed covered by a liquid sodium pool at the saturation temperature, the heat transfer mechanism consists of a downward flow of sodium from the pool through the bed, evaporation of the liquid due to the fuel heat generation, and upward flow of sodium vapor through the bed into the pool. At some decay heat level, the liquid cannot flow downward fast enough and the lower region of the bed "dries out." This decay heat level is known as the dryout flux.

Recent experiments[5] indicate that dryout does not lead directly to melting of the fuel particles. However, the ability to predict the decay heat level at which a debris bed will dry out is still necessary for any further analysis.

Current Status of Experimental and Analytical Efforts

The first experiments to produce dryout in an unconsolidated porous bed were initiated at Argon National Laboratory in 1971.[4] During

the first phase of the experiments, simulated debris beds (composed of UO2-sodium, UO2-water, and sand-water combinations) were heated from the bottom. Typical results are seen in Fig. 2. For deep beds, the dryout flux increases gradually with decreasing depth. When the bed becomes sufficiently-shallow, the dryout flux increases drastically.

The sand-water bed was observed visually during the boiling process. The vapor escaped from the bed through channels in the bed (Figs. 3 and 4). When the bed depth was under two inches, the channels extended to the bottom of the bed. For bed depths greater than two inches, the channels penetrated to a depth less than the bed height.

The observation was combined with the data for dryout flux to categorize beds into two configurations: deep beds, where the channels penetrate partially, and shallow beds, where the channels penetrate completely. The implication of this categorization is that, when the channels reach the bottom of the bed, the dryout heat flux increased drastically with decreasing bed depth.

In order to determine the nature of the liquid flow pattern, a dye was added to the overlying water pool at the beginning of the experiment. The dye was seen to flow uniformly down through the bed and not through the channels. From this, it was concluded that no significant downward liquid flow existed in the channels.

A particle circulation pattern was observed during boiling. Particles descended along the test section wall and ascended along the channel walls. Some particles were entrained behind the bubbles.

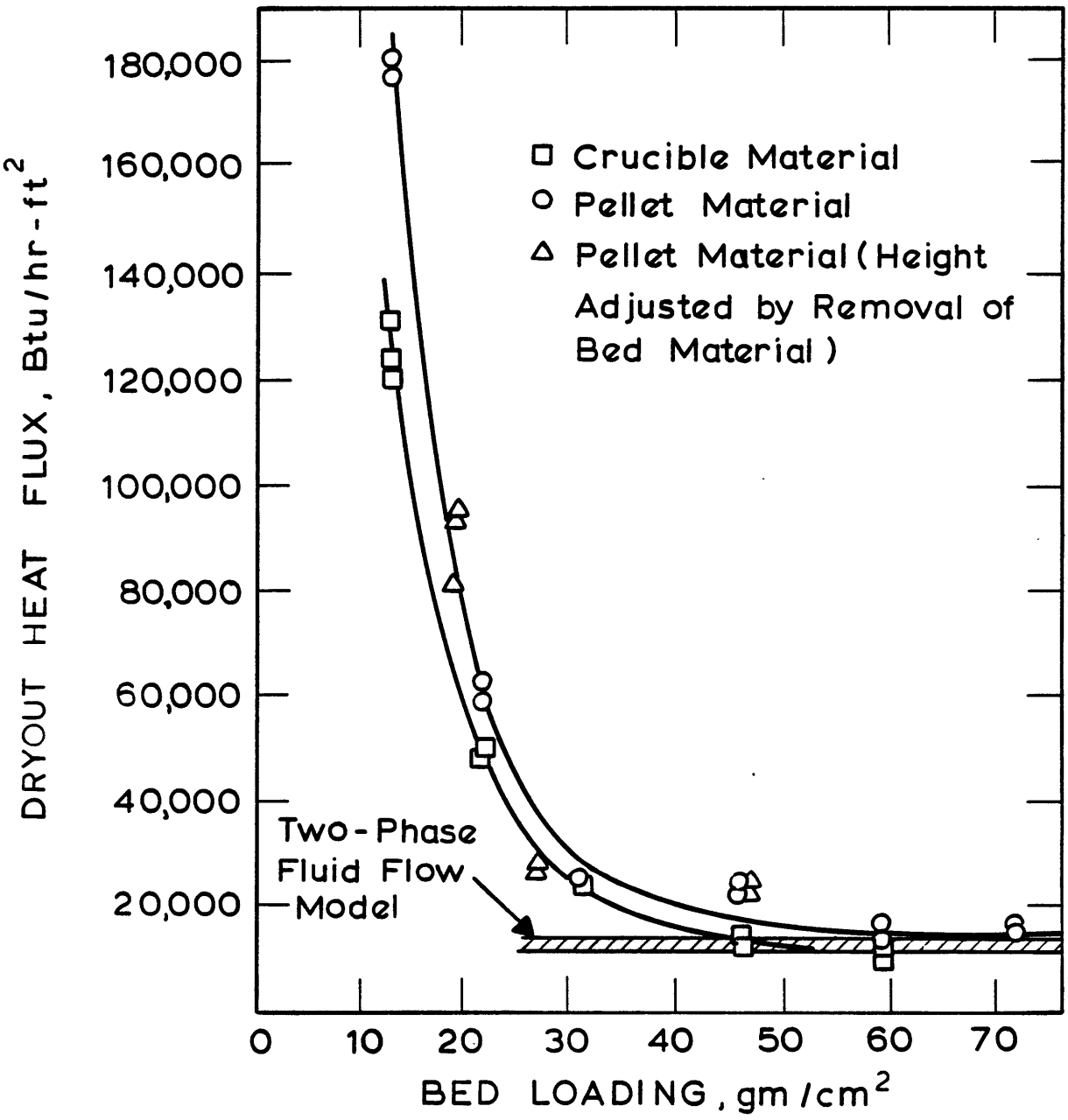

Fig 2 Comparison of Two-Phase Fluid Flow Model with Data for Dryout Heat Fluxes from UO_2-Water Beds (Ref. 4)

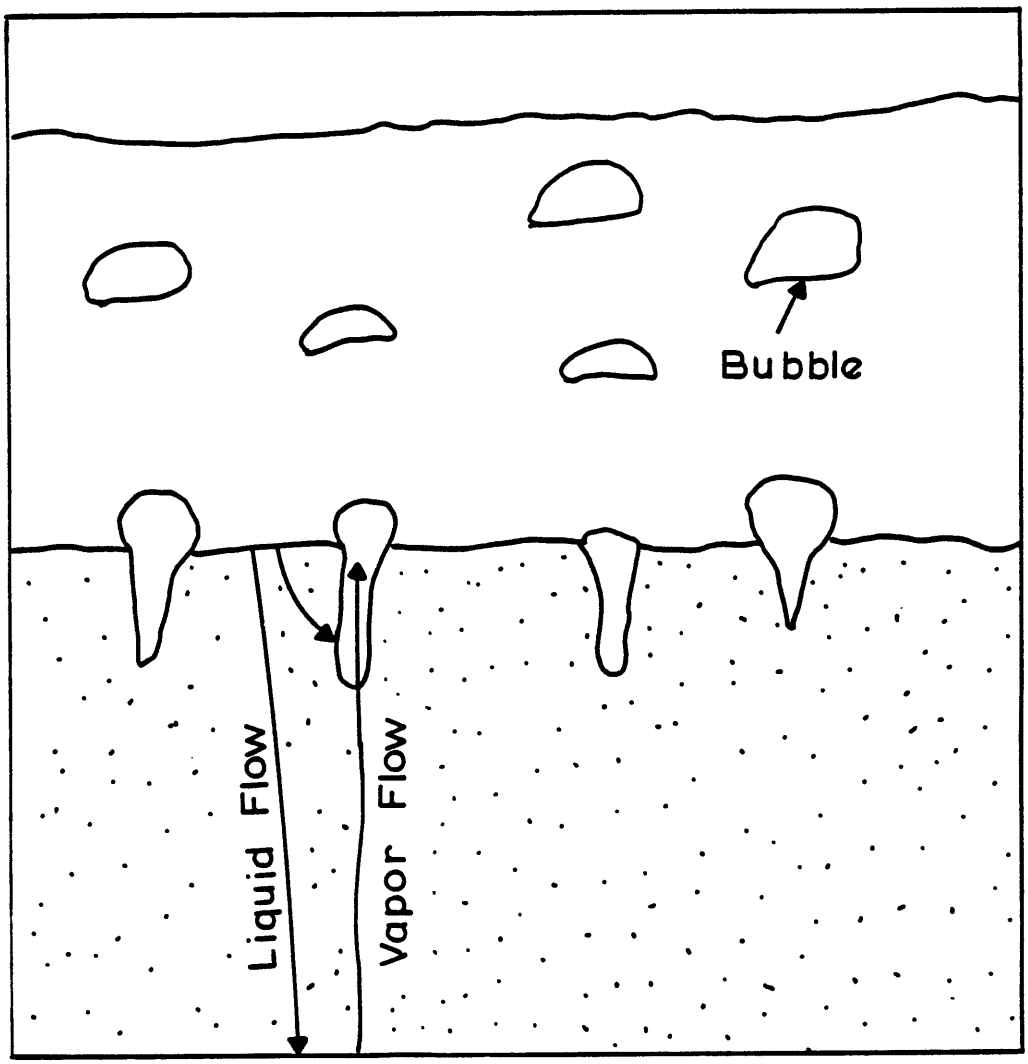

Fig 3. Observed Mechanism of Water Boiling in Deeper UO_2 Beds (Ref 4)

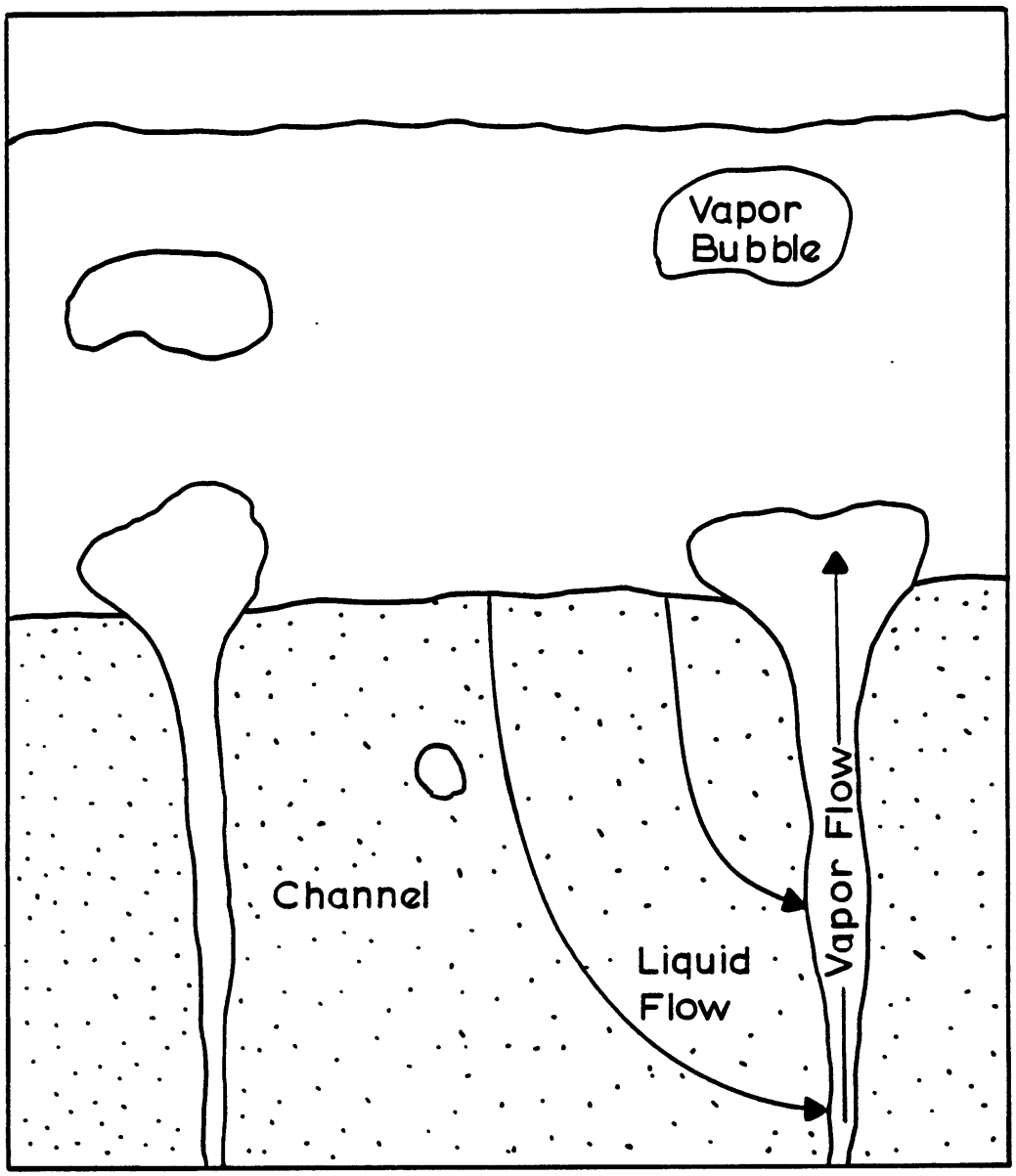

Fig 4 Observed Mechanism of Water Boiling in Sand Beds and Shallow UO_2 Beds (Ref. 4)

Three analyses were used to predict dryout flux. For deep beds, a two phase porous media counter flow medel was constructed based on the correlation of Brown and Associates[6]. The model is claimed to work reasonably well. It is sensitive to parameters such as porosity, and therefore will yield a reasonably large uncertainty band.

A characteristic of this model is that the dryout flux is predicted to be independent of bed height. The data collected in these experiments suggest a dependence between the two. Later data demonstrate a more pronounced dependence. The addition of capillary forces to the model would predict this effect.

For beds in which channeling is significant, a model based on downward flow of liquid in the interstices and upward flow of vapor through tubes was proposed. However, the model requires a knowledge of the channel population density (channels/cm2), channel diameter and depth, and the appropriate friction factor to use in the channel. The equation derived for this model evidently can be fitted to the data, but there has been no data presented, then or since, which confirms the universality of the fit.

Calculations indicate that this model predicts dryout fluxes an order of magnitude too large when the channels reach the bottom. It is probably for this reason that an upper bound on dryout flux was proposed. The correlation used is for flooding of packed towers[7]. This correlation agrees with the sand-water data (particles 690 microns in diameter) but does not agree with any other data. The flooding

correlation itself is based on data outside the range of interest for this application and is of questionable validity here.

A subsequent set of tests used Joule heating of the liquid. While some interesting observations were made using this technique, the method itself is questionable. It seems likely that the volumetric heat generation would be proportional to the saturation, thus breaking the analogy to heat generation in solids. Also, since this would imply a lack of heat generation in the dryout zone, dryout would be difficult to detect using thermocouples.

The second set of experiments to produce dryout in an unconsolidated porous bed were conducted at U.C.L.A. in 1974.[8] The experimental apparatus inductively heated steel and lead shot in water. Unfortunately, data generated at a later time[9] using the same equipment are inconsistent with the former data. This latter report also has data on dryout flux using acetone and methanol.

In the analysis conducted by Dhir and Catton[9], the major fault is the assumption that the flow of the vapor through the porous material is inviscid. As will be seen in chapter 2, the vapor creates an adverse pressure gradient in the liquid which must be overcome by the liquid body forces. The problem is disguised by the nondimensionalization of the integrated dryout flux with Zuber's critical heat flux. The suggestion is made that the limiting value of the integrated dryout flux is the pool boiling critical heat flux. This may prove to be the case, however, the physical reasoning justifying the statement has not been presented. Additionally, most dryouts occur sufficiently below this upper bound so that its use is limited.

As part of their qualitative observations, Dhir and Catton[9] characterized the channeled portion of the debris bed as being fluidized. This created some controversy. Strictly speaking, fluidization occurs when the drag forces of a fluid acting on a group of solid particles overcome the body forces acting on those particles. This can occur in the vapor channels, but the liquid in this part of the bed must be moving downward. Hence the liquid drag on the particles is in the same direction as the gravity vector. This is not the classical form of fluidization.

Experiments conducted at Sandia Laboratories[10,11] used joule heating of water. This analysis proposed with this set of data is essentially a restatement of the deep bed analysis presented by Gabor et. al.[4] with different models used for the various fudge factors. The model is still inaccurate for shallow beds.

Shires and Stevens[12] were the first to include the effects of surface tension in their predictive model. In other respects, this model is more simple than that of Hardee and Nilson.[11] The experiments[13] associated with this effort used direct heating of the particles via current flow through the particles. The particle diameters ranged from 0.68 mm to 2.0 mm, which is somewhat larger than in previous tests.

Several interesting observations were made in these experiments. First, dryout was seen to begin somewhere in the main body of the bed rather than at the bottom. Also it was claimed that dryout was not as sensitive to porosity or particle diameter as had been previously claimed.

Lipinski[14,15,16] has proposed a model for deep beds that basically is a restatement of the Hardee and Nilson model with capillarity and turbulence added. Effects of channeling are not considered.

In-pile experiments are currently being conducted at Sandia Labs.[17,18,19,20] using sodium and uranium fuel. For all data sets generated to date, the overlying sodium pool has been subcooled and the debris has been inhomogeneous in particle size. The attempt here is to create dryout in "real" configurations. In some cases, the dryout flux for extremely subcooled sodium is less than that for sodium with less subcooling. This has been attributed to the collapse of vapor channels. However, in the absence of a model for channels, this has not been proven.

Problem Statement

To date, all attempts to quantify the effects of channeling have failed. In fact, the physical causes of channeling have not yet been identified. It is the intent of this work to explore the physics of channeling. This will lead to a model for liquid and vapor flow in the channeled region. Also, the equations for two phase flow in unchanneled porous media will be developed. These equations will be similar to the ones developed by Lipinski, but will differ in some aspects. The two submodels will then be combined to form a two-region one-dimensional model for dryout in a heat-generating unconsolidated porous media.

II. TWO PHASE FLOW IN UNCHANNELED POROUS MEDIA

Constitutive Equations

The constitutive equations describing two phase flow in porous media are well documented.[21,22] Lipinski has manipulated these equations to construct a model for dryout in unchanneled debris beds. Certain coefficients which appear in these equations are empirical in nature, and a choice among correlations must often be made. In order to pinpoint the alternatives for coefficients and to gain insight into the physics of the flow phenomena, the dryout equations will be developed.

Single phase porous flow can be described by the Ergun equation[23]

$$-\frac{d\hat{P}}{dz} = \frac{\mu}{k} q + \frac{\rho}{\kappa} q |q| \qquad 2.1$$

where

$$k = \frac{d^2 \varepsilon^3}{150 (1-\varepsilon)^2}$$

$$\kappa = \frac{\varepsilon^3 \bar{d}}{1.75 (1-\varepsilon)} \qquad 2.2$$

and

$$\hat{P} = P + \rho g z$$

The superficial velocity of the fluid (q) is the volume flow rate per total cross-section area. The laminar and turbulent permeabilities are k and κ respectively. The equation is semi-empirical.

When both liquid and vapor phases are present, the pressure gradient is greater than that expressed by equation 2.1. To account for the coexistence of liquid and vapor, equation 2.1 may be modified by introducing factors k_v , k_ℓ , κ_v , κ_ℓ , which are functions of the fractional saturation, S , and have magnitudes between 0 and 1. These factors are called "relative permeabilities." The following equations are written in the form Lipinski[21] used.

$$-\frac{d\hat{P}_\ell}{dz} = \frac{\mu_\ell}{kk_\ell} q_\ell + \frac{\rho_\ell}{\kappa \kappa_\ell} |q_\ell| q_\ell$$

$$-\frac{d\hat{P}_v}{dz} = \frac{\mu_v}{kk_v} q_v + \frac{\rho_v}{\kappa \kappa_v} |q_v| q_v \qquad 2.3$$

(see Fig. 5)

where

$$\begin{aligned} k_v &= k_v(S) \\ k_\ell &= k_\ell(S) \\ \kappa_v &= \kappa_v(S) \\ \kappa_\ell &= \kappa_\ell(S) \end{aligned} \qquad 2.4$$

The difference between the vapor and liquid pressures is the capillary pressure. According to Leverett[24]

$$\frac{P_c}{\sigma \cos\theta} \left(\frac{k}{\varepsilon}\right)^{1/2} = \mathcal{P}(S)$$

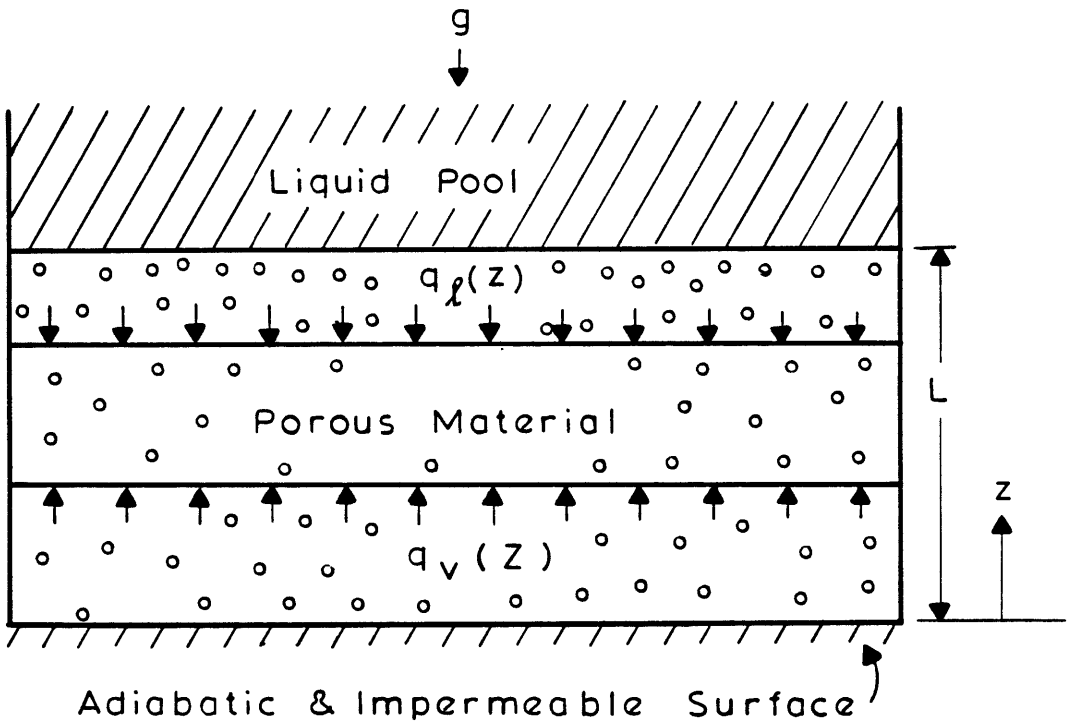

Fig 5 Schematic of Liquid - Vapor Counter-flow in Porous Media

Where $P_c = P_v - P_\ell$, and $P(S)$ is the empirical relationship known as the Leverett J-curve (Fig. 6). The data base for this correlation is a set of experiments using washed sands of small diameter. There does not appear to be any set of correlated data on capillary pressure curves for unconsolidated small particles. Interest in geologic circles is in cemented formations. The chemical industry is typically interested in larger particles.

The shape of the capillary pressure-saturation curve is of interest. The existance of a finite capillary pressure at a saturation of unity in the drainage experiment can be explained by comparing the porous media to a collection of parallel capillary tubes initially filled with a wetting liquid. When the liquid and vapor pressures are equal, the interface between phases is flat. (See Fig. 7). As the vapor pressure is increased, the phase interface becomes increasingly concave until the minimum radius of curvature in the largest tube is reached. At this point, the vapor pressure is sufficiently large to push the liquid from the largest tubes. As the vapor pressure is increased beyond this point, smaller tubes can be evacuated and the saturation decreases.

The S-shape of the Leverette curve has been well established, but the actual values of $P(S)$ depend upon the porous material.[25,26,27] Measurements of this curve have been made principally for consolidated geologic media. There is a paucity of data for unconsolidated materials. Therefore the Leverett data will be used, even though the particle diameters of interest are greater than those in the

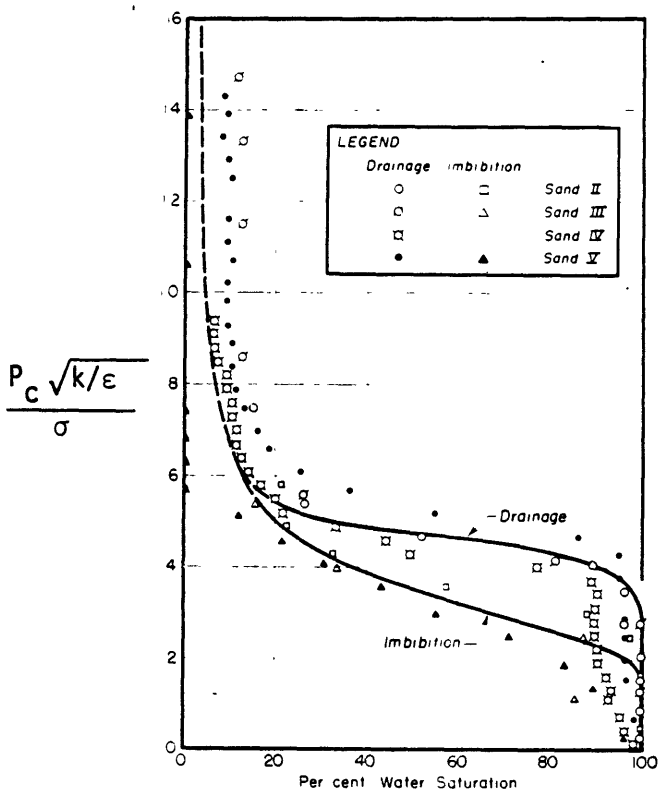

Fig. 6. Correlation of Data from Height-Saturation Experiments on Clean Unconsolidated Sands. (Ref. 24)

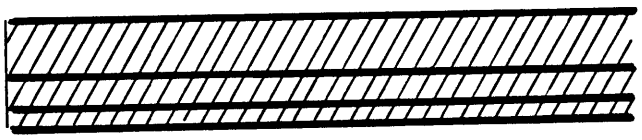

$$P_c = 0 = P_v - P_\ell$$

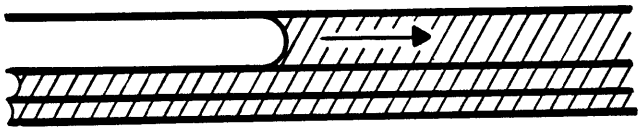

$$P_c = P_v - P_\ell = \frac{2\sigma \cos \phi}{r_{max}}$$

$$P_c = P_v - P_\ell = \frac{2\sigma \cos \phi}{r}, \quad r < r_{max}$$

Fig. 7
Drainage of Tubes via Vapor Pressure Increase

experiment. The curve can be approximated by the equation

$$P(S) = a\, S_e^{-b} \qquad 2.6$$

where

$$S_e = \frac{S - S_r}{1 - S_r} \qquad 2.7$$

and S_r is the residual saturation. For the drainage curve,

$$a = 0.3771$$

$$b = 0.2430$$

$$S_r = 0.03 \qquad 2.8$$

For the imbibition curve

$$a = 0.2353$$

$$b = 0.4230$$

$$S_r = 0.02 \quad . \qquad 2.9$$

The relative permeabilities, k_v , k_ℓ , κ_v , κ_ℓ , are functions of the saturation (S). This is somewhat surprising in that phase interactions having to do with the relative velocity of the two fluids might be expected. This is not the case. It must therefore be concluded that the phases occupy different portions of the porous media, and that, as a consequence, interphase shear forces are unimportant when compared to the influence of the solid material. This is contradictory to the commonly held view that the two phases frequently occupy the same flow channel.

There is some uncertainity concerning the values of the relative permeabilities. Lipinski[14] uses a correlation for laminar coefficients

which appears in Scheidegger.[21]

$$k_\ell = S^3$$
$$k_v = 1 - 1.11\ S \qquad 2.10$$

The relationship is based on oil-water data. The relative permeability might be expected to vary with different porous materials and different fluid combinations.

An alternative correlation for laminar relative permeability was advanced by Brooks and Corey.[26,27] Their approach related the relative permeabilities to the capillary pressure-saturation curve in a semi-empirical manner. Using the relationships they proposed and equation 2.6

$$k_\ell = S_e^{\,2b+3}$$
$$k_v = (1 - S_e)^2\ (1 - S_e^{\,2b\,+\,1}) \qquad 2.11$$

(see Appendix I).

Little data has been generated on turbulent relative permeability.[21] For this reason, three models will be mentioned and the predictions will be compared to determine sensitivity to this parameter. If only the one-dimensional flow area is considered

$$\kappa_\ell = S^2$$
$$\kappa_v = (1 - S)^2 \qquad 2.12$$

Lipinski[14] proposes that

$$\kappa_\ell = S^3$$
$$\kappa_v = (1 - S)^3 \qquad 2.13$$

but gives no justification. A third model can be obtained in a manner similar to that of Brooks and Corey. (Appendix I)

$$\kappa_\ell = S_e^{5+b}$$
$$\kappa_v = (1 - S_e)^3 (1 - S_e^{1+b/2}) \qquad 2.14$$

If the overlying liquid exists at the saturation temperature, and temperature increases in the vapor are ignored, then the energy and continuity equations become

$$q_{\ell_z} = \int_0^z \frac{-\ddot{q} (1 - \varepsilon)}{\rho_\ell h_{fg}} dz$$

and

$$q_{v_z} = \int_0^z \frac{\ddot{q} (1 - \varepsilon)}{\rho_v h_{fg}} dz \qquad 2.15$$

where $\ddot{q}$ is the volumetric energy generation in the solid (W/m^3 of solid).

Saturation Equation

Having the constitutive equations, one can derive a differential equation for the saturation as a function of position. Writing the vapor pressure as the sume of the liquid and capillary pressures and differentiating

$$\frac{dP_v}{dz} = \frac{dP_\ell}{dz} + \frac{dP_c}{dz} \qquad 2.16$$

Equation 2.5 can be differentiated to obtain the capillary pressure gradient.

$$\frac{dP_c}{dz} = \sigma \cos\Theta \left(\sqrt{\frac{\varepsilon}{k}} \frac{dP}{dS} \frac{dS}{dz} + P \frac{d\sqrt{\varepsilon/k}}{dz} \right) \qquad 2.17$$

Substituting 2.3 and 2.17 into 2.16 and rearranging, the differential equation for saturation in terms of superficial velocity is found.

$$\frac{dS}{dz} = \frac{1}{\frac{dP}{dS}\sqrt{\varepsilon/k}} \left\{ \frac{1}{\sigma \cos\Theta} \left[(\rho_\ell - \rho_v)g + \frac{1}{k} \left(\frac{\mu_\ell}{k_\ell} q_\ell - \frac{\mu_v}{k_v} q_v \right) + \frac{1}{\kappa} \left(\frac{\rho_\ell}{\kappa_\ell} |q_\ell| q_\ell - \frac{\rho_v}{\kappa_v} |q_v| q_v \right) \right] - P \frac{d\sqrt{\varepsilon/k}}{dz} \right\} \qquad 2.18$$

Using the energy/continuity equations (2.15) to eliminate the superficial velocities, and assuming that q is independent of position

$$\frac{dS}{dz} = \frac{1}{\sqrt{\varepsilon/k}\frac{dP}{dS}} \left\{ \frac{1}{\sigma \cos\Theta} \left\langle (\rho_\ell - \rho_v)g - \frac{\ddot{q}}{kh_{fg}} \left[\int_0^z (1-\varepsilon)dz \right] \cdot \left(\frac{\nu_\ell}{k_\ell} + \frac{\nu_v}{k_v} \right) + \frac{1}{\kappa} \left(\frac{\ddot{q}}{h_{fg}} \right)^2 \left[\int_0^z (1-\varepsilon)dz \right]^2 \cdot \left(\frac{1}{\rho_\ell \kappa_\ell} + \frac{1}{\rho_v \kappa_v} \right) \right\rangle - P \frac{d\sqrt{\varepsilon/k}}{dz} \right\} \qquad 2.19$$

Nondimensionalizing

$$\frac{dS}{d\eta} = \left(\sqrt{\frac{\Pi_k}{\varepsilon}} / \frac{dP}{dS} \right) \left\{ \frac{1}{\sigma \cos\Theta} \left\langle \Pi_g (1 - \Pi_{\rho_v}) - \frac{\Pi \ddot{q}}{\Pi_k} \left[\int_0^\eta (1-\varepsilon)d\eta \right] \cdot \left(\frac{1}{k_\ell} + \Pi_\nu / k_v \right) \frac{\Pi^2 \ddot{q}}{\Pi_\kappa} \left[\int_0^\eta (1-\varepsilon)d\eta \right]^2 \left(\frac{1}{\kappa_\ell} + \frac{1}{\Pi_{\rho_v} \kappa_v} \right) \right\rangle - P \frac{d\sqrt{\varepsilon/\Pi_k}}{d\eta} \right\} \qquad 2.20$$

where

$$\Pi_k = \frac{k}{L^2} \qquad \Pi_g = \frac{\rho_\ell \, g \, L^2}{\sigma}$$

$$\Pi_\kappa = \frac{\kappa \, \rho_\ell \, \nu_\ell \, L}{\sigma \, L^2} \qquad \Pi_{\rho_v} = \frac{\rho_v}{\rho_\ell} \qquad 2.21$$

$$\Pi_{\ddot{q}} = \frac{\ddot{q} \, \nu_\ell \, L}{\sigma \, h_{f_g}} \qquad \Pi_\nu = \frac{\nu_v}{\nu_\ell}$$

$$\eta = z/L$$

Boundary Conditions

The saturation-position equation (2.20) is first order and nonlinear. A single boundary condition is needed for a given energy generation rate. The condition to be specified is the saturation at z = L. Once determined, equation (2.20) can be integrated from z = L to z = 0 to determine the saturation at the bottom (S(z=0)). (See Appendix II for a more rigorous definition of dryout). The energy generation rate can then be adjusted until the saturation at the bottom equals zero.

The saturation at the top of the porous media is determined by examining the pressure difference between the liquid and the vapor in

the overlying liquid pool. When a porous stone is the medium of interest, jets of vapor having a finite radius can be seen at the stone-pool interface. For this case

$$P_v(z = L) - P_\ell (z = L) = P_c (z = L) = \frac{\sigma}{r_{jet}} \quad . \qquad 2.22$$

This same pressure difference must exist on both sides of the interface. Therefore

$$P_c (z = L) = \frac{\sigma \cos\Theta}{\sqrt{k/\varepsilon}} P(S)\Big|_{z=L} = \frac{\sigma}{r_{jet}} \quad . \qquad 2.23$$

Substituting 2.6 for $P(S)$

$$S(z = L) = \left(\frac{1}{a} \sqrt{k/\varepsilon} \quad \frac{1}{r_{jet} \cos\Theta} \right)^{-1/b} \qquad 2.24$$

When vapor exits from an unconsolidated porous medium, jets are not seen. Instead, large bubbles are observed immediately above the solid particles, indicating that the pressure difference between the liquid and vapor is small when compared to the minimum capillary pressure in the porous material. The obvious conclusion to which one leaps is that the capillary pressure at the top of the bed is zero. Consequently, the saturation at the top is unity. This creates an interesting anomaly. If the equations of porous flow apply at the top, and a finite vapor flux is expected, then the superficial velocity must be infinite to cancel the effect of a vapor flow area equal to zero.

The problem here is more than just a mathematical artifice. It is, in fact, the key to vapor channeling in unconsolidated porous

materials. In the channeled region, the vapor flow is not described by the Ergun equations. This suggests that the debris bed should be divided into two regions for the purpose of analysis. In the region

$$0 \leq z \leq L - h$$

the equations of two phase counterflow apply. In the region

$$L - h \leq z \leq L$$

the vapor flow is described by a different set of equations. The saturation at the interface of these two regions ($S(z = L - h)$) will be less than unity.

In order to determine the saturation at the bottom of the debris bed, the differential equation for saturation (2.19) must be integrated from $z = L - h$ to $z = 0$. The analysis of the channeled region will provide values for the channel depth (h) and the saturation at the bottom of the channels ($S(z = L - h)$).

III. CHANNELED REGION

Saturation at the Bottom of the Channel

One of the observations universal to all the visualization experiments is that particles which appear in the channels are carried up into the overlying liquid pool by the vapor. The vapor must therefore have a minimum velocity equal to the terminal velocity in the channels. To translate this into an estimate for saturation at the bottom of a channel, a clear picture of the relative positions of the liquid and vapor within the porous matrix is needed.

Versluys first catagorized partially saturated media into two states, the pendular and the funicular (Fig. 8). The former corresponds to the residual saturation, where the individual pockets of liquid are unconnected and liquid flow is impossible. The pendular regime corresponds to the state where liquid can flow and the vapor exists in small channels which tortuously wind through the liquid. The funicular state has been observed.[29] The pendular state is a mental fiction and is demonstrably incorrect. Such a model predicts that the capillary pressure should increase with increasing saturation. The Leverett curve (Fig. 6) demonstrates exactly the opposite behavior. This incorrect visualization of partial saturation has survived[21,22] despite visual studies[29] which deny its existance.

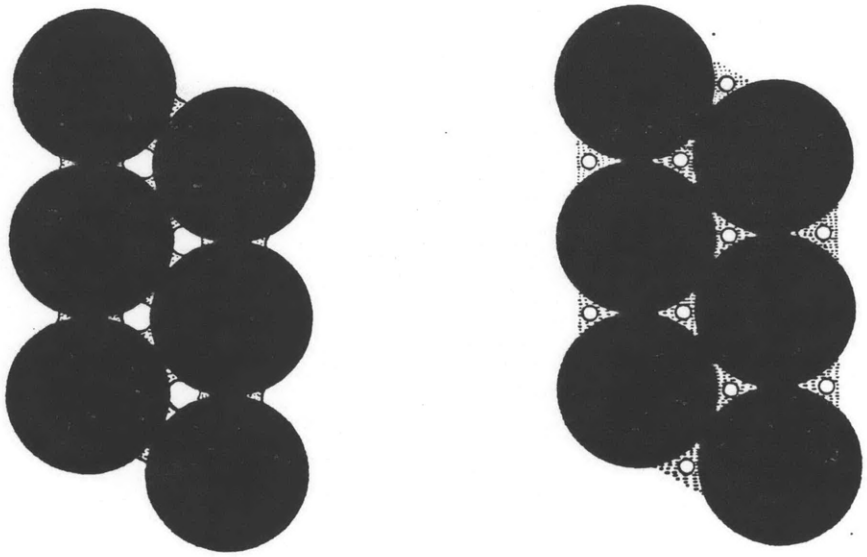

Fig. 8. Drawing of pendular(a) and funicular(b) saturation regimes for an idealized porous medium consisting of packed spheres (after Versluys 1931). (Ref. 28)

The flow regime which exists in the unchanneled region is what Chatenever[24] calls, rather unfortunately, channel flow. In this regime, the liquid and vapor occupy separate regions of the particle bed. Each region contains particles. The intersticies that the wetting fluid occupies are smaller than those occupied by the nonwetting fluids. This is consistent with the tube bundle model analogy that predicts the nature of the capillary pressure-saturation curve. The flow paths of each phase may be circuitious. (See Fig. 9).

Figure 10 depicts a possible liquid-vapor geometry at the base of a channel. As the vapor rises, the saturation increases, the flow area for the vapor decreases, and the interstical vapor velocity increases. When the vapor velocity is sufficiently large, particles can be entrained by the vapor and a channel is possible.

The average interstical velocity in the z direction immediately below the channel is

$$V_{\text{vapor } i} = \frac{q_v}{(1 - S_m)\varepsilon} \tag{3.1}$$

where S_m is the saturation immediately below the channel. If the vapor feeds into the bottom of the channel only, then the average vapor velocity in the channel is

$$\begin{aligned} V_{\text{vapor } c} &= V_{\text{vapor } i}\,(1 - \varepsilon) \\ &= \frac{q_v\,(1 - \varepsilon)}{(1 - S_m)\varepsilon} \\ &\simeq \frac{(1 - \varepsilon)}{(1 - S_m)\varepsilon} \int_0^L \frac{\ddot{q}\,(1 - \varepsilon)}{\rho_v\, h_{fg}} \end{aligned} \tag{3.2}$$

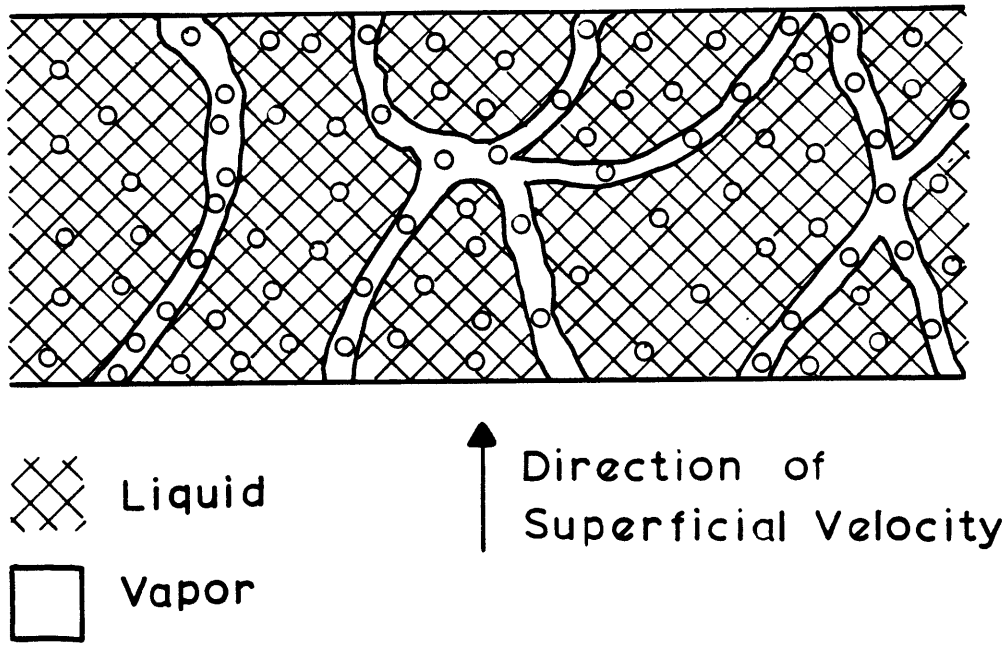

Fig 9 Vapor Flow in a Partially Saturated Porous Media

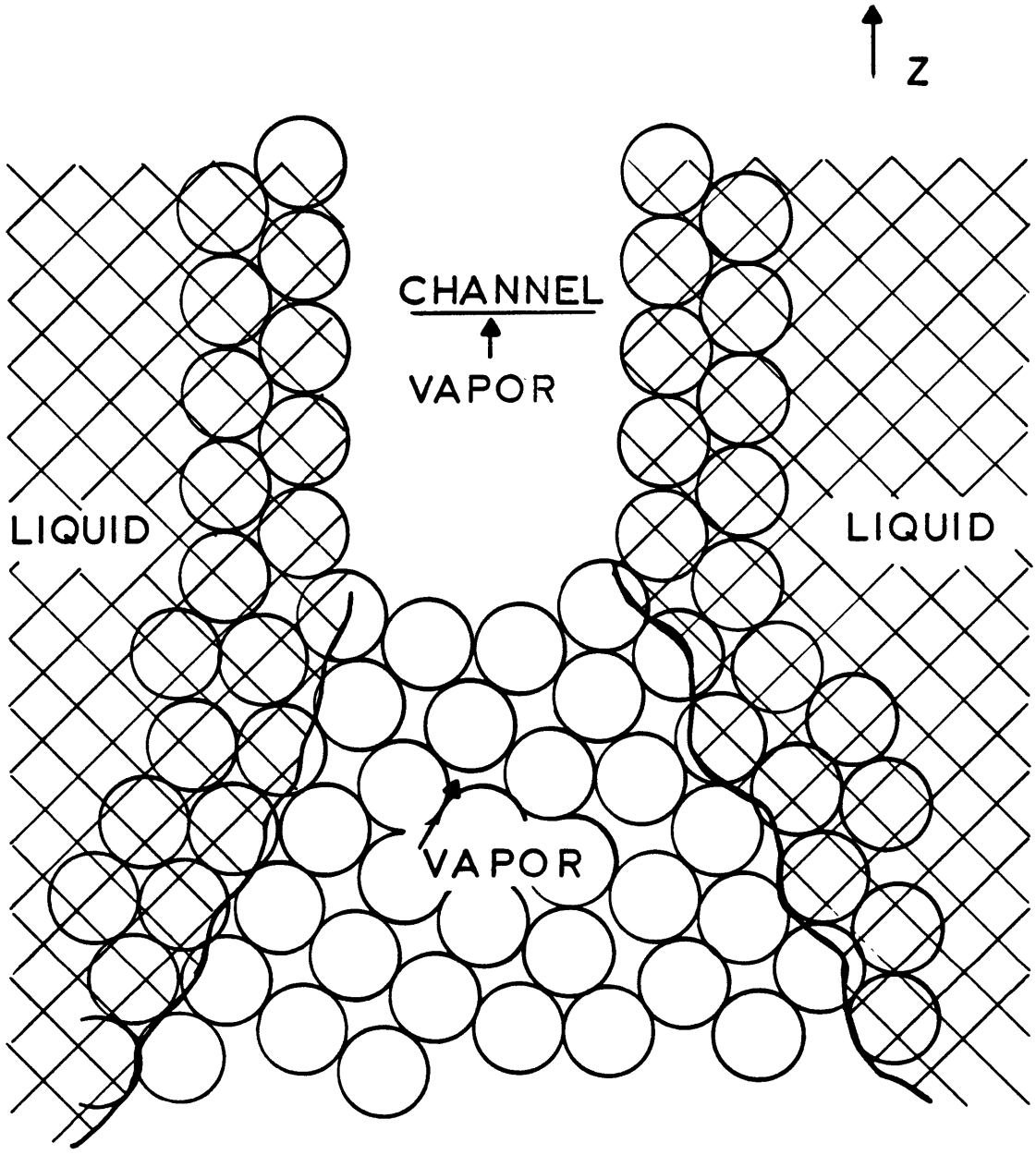

Fig 10. Schematic of Vapor Feeding into a Channel

If the average vapor velocity is set equal to the terminal velocity of the solid particle, then equation 3.2 may be solved for S_m.

Consider the specific case of 300 micron glass particles (ρ_s=2500) kg/m^3) immersed in water. The terminal velocity of a single particle in steam at one atmosphere is about 3.3 m/S. Assume a bed height of 15 cm, a porosity of 0.4, and a energy generation rate of 10^7 W/m^3. Using equation 2.26, S_m is approximately equal to 0.7. This particular case is conservative in the extreme. Metal particles have a higher terminal velocity which yields a larger value for S_m.

The actual value of interest is the capillary pressure at the bottom of the channel. The ratio of the capillary pressure at a saturation of 0.7 to that at a saturation of 0.99 is 1.09. This means a good approximation for the saturation at the bottom of the channel is

$$S_m \approx 0.99 \quad . \qquad 3.3$$

Channel Depth

A bound on the channel depth can be obtained by examining the geometry of a channel, drawing a freebody of the solids, and applying the principles of soil mechanics. Figure 11 is a schematic of a vertical channel wall. Vapor in the channel contacts both liquid and solid surfaces. The liquid, which exists at a lower pressure than the vapor, is held in place by surface tension. The difference between the liquid and vapor pressures is transmitted as a compressive horizontal stress to the solid matrix. The body forces acting

MICROSCOPIC VIEW OF CHANNEL INTERFACE

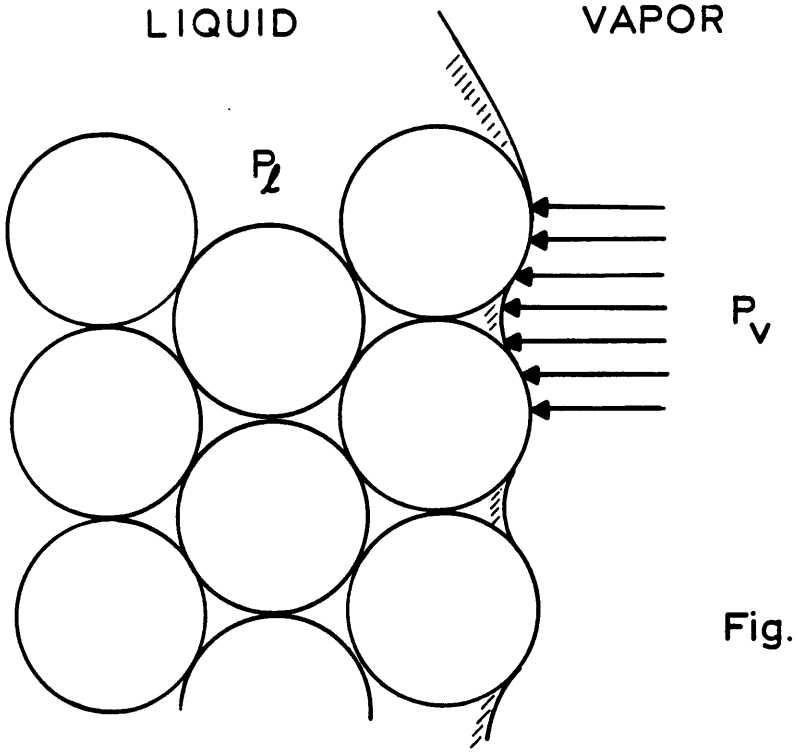

Fig. 11

FREEBODY OF ELEMENT OF POROUS MATERIAL

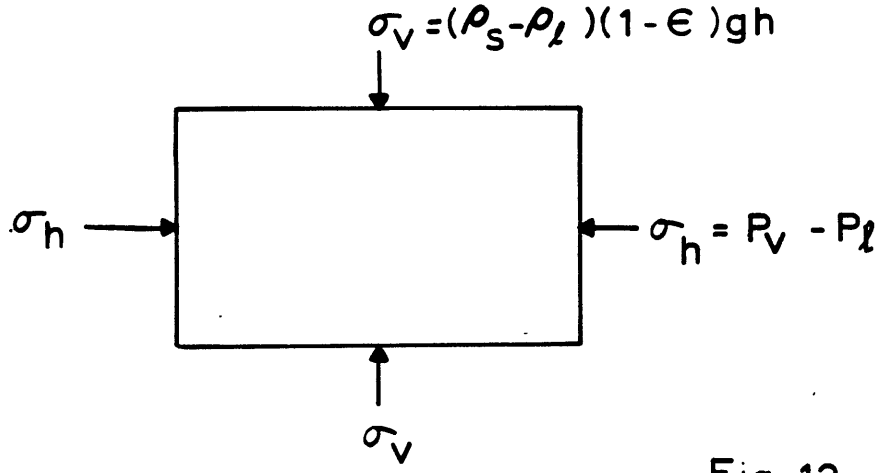

Fig. 12

upon the solid immersed within the liquid produce a vertical stress on the solid matrix (Fig. 12). The shear stress on the channel wall is assumed to be negligible.

$$\sigma_v = (\rho_s - \rho_\ell)(1 - \varepsilon)g(L - z) \qquad 3.4$$

$$\sigma_h = P_v - P_\ell = P_c \qquad 3.5$$

$$\tau = 0 \qquad 3.6$$

The porous matrix next to a channel can fail in two ways. If the vapor pressure is too low, the particles will slide inward and the channel will collapse. Alternatively, if the vapor pressure is too large, the particles will be forced outward and the channel will expand.

For unconsolidated particulate beds, the failure limits are described by the Mohr-Coulomb failure law.[30] The failure criteria is described by the failure curve on the Mohr diagram (Fig. 13) which is approximately linear for small loads. The angle of the failure curve is known as the friction angle. This angle can vary from about 25^o to 50^o, depending upon the particle size, porosity, saturation, and solid properties.

A state of stress described by a Mohr's circle which lies below the failure curve is stable. A Mohr's circle which crosses the failure curve describes a state which will fail. A state of impending failure is described by a Mohr's circle which is tangent to the failure curve.

MOHR - COULOMB FAILURE LAW

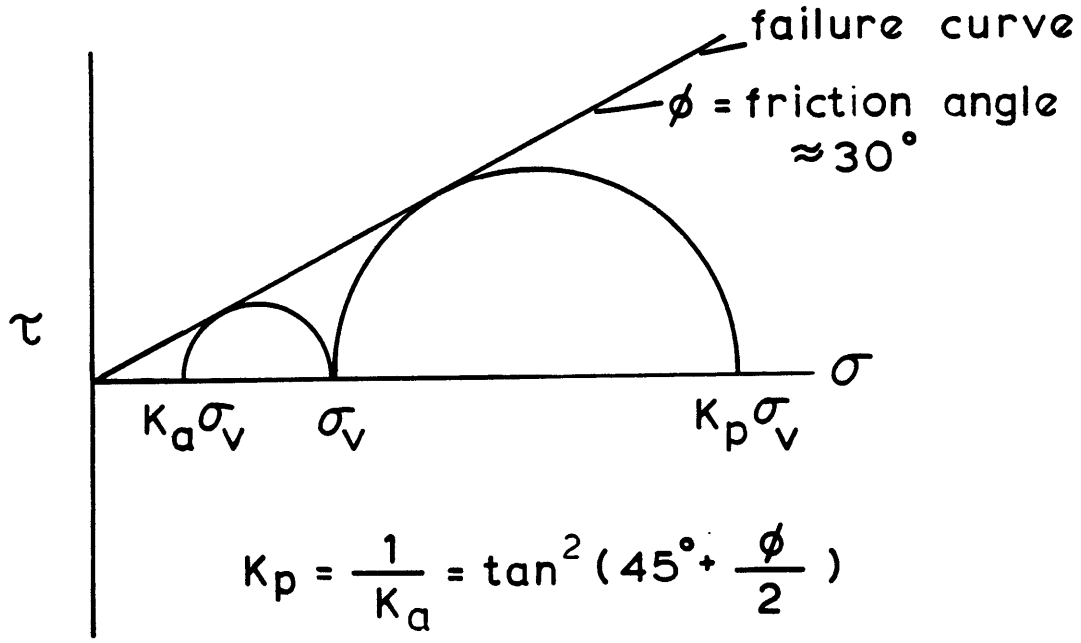

$$K_p = \frac{1}{K_a} = \tan^2\left(45° + \frac{\phi}{2}\right)$$

IF $\sigma_h \leq K_a \sigma_v$ THE CHANNEL WILL COLLAPSE

IF $\sigma_h \geq K_p \sigma_v$ THE MATERIAL SURROUNDING THE CHANNEL WILL FAIL

Fig 13

For the given value of vertical stress, there are two possible states of failure. The Rankine active state occurs when

$$\frac{\sigma_h}{\sigma_v} = K_a = \tan^{-2}(45^o + \phi/2) . \qquad 3.7$$

This is the state of impending channel collapse. The Rankine passive state occurs when

$$\frac{\sigma_h}{\sigma_v} = K_p = \tan^{2}(45^o + \phi/2) . \qquad 3.8$$

This is the state of impending channel expansion. Combining equations 3.7 and 3.8

$$K_a \sigma_v \leq \sigma_h \leq K_p \sigma_v \qquad 3.9$$

Using equations 3.4 and 3.5

$$K_a(\rho_s - \rho_\ell)(1 - \varepsilon)g(L - z) \leq P_c \leq K_p(\rho_s - \rho_\ell)(1 - \varepsilon)g(L - z) \qquad 3.10$$

At the bottom of channel,

$$L - z = h$$

and

$$P_c \cong P_c\,(S = 0.99) . \qquad 3.11$$

Substituting

$$K_a(\rho_s - \rho_\ell)(1 - \varepsilon)gh \leq P_c\,(S = .99) \leq K_p(\rho_s - \rho_\ell)(1 - \varepsilon)gh . \qquad 3.12$$

The unknown in the above equation is the channel depth (h).

Rearranging

$$\frac{1}{K_p}\ h_o \leq\ h \leq\ \frac{1}{K_a}\ h_o$$

where

$$h_o = \frac{P_c\ (S = 0.99)}{(\rho_s - \rho_\ell)(1 - \varepsilon)g} \qquad 3.14$$

The value of the capillary pressure at a saturation of 0.99 is calculated from the Leverett curve.

$$P_c\ (S = .99) \approx a\ \sigma\cos\theta\sqrt{\varepsilon/k} \qquad 3.15$$

$$= 0.3771\ \sigma\ \cos\theta\ \sqrt{\varepsilon/k} \qquad 3.16$$

The problem with this analysis is that it only bounds the channel depth. For a friction angle of 30^o,

$$K_a(\phi = 30^o) = 0.33$$

$$K_p(\phi = 30^o) = 3.00\ .$$

The uncertainty in the channel depth is too large.

Experiment

Since a theoretical analysis could only bound the channel depth, it was decided to try to measure the depth directly. A thin transparent test section (Fig. 14) was built with a gas plenum at its base. At the bottom of the test sextion was a layer of 16 mesh nylon screening material. A mixture of liquid and solid shot was poured into the test section and allowed to settle. Liquid was added to increase the depth of the overlying liquid pool. The section was then lightly

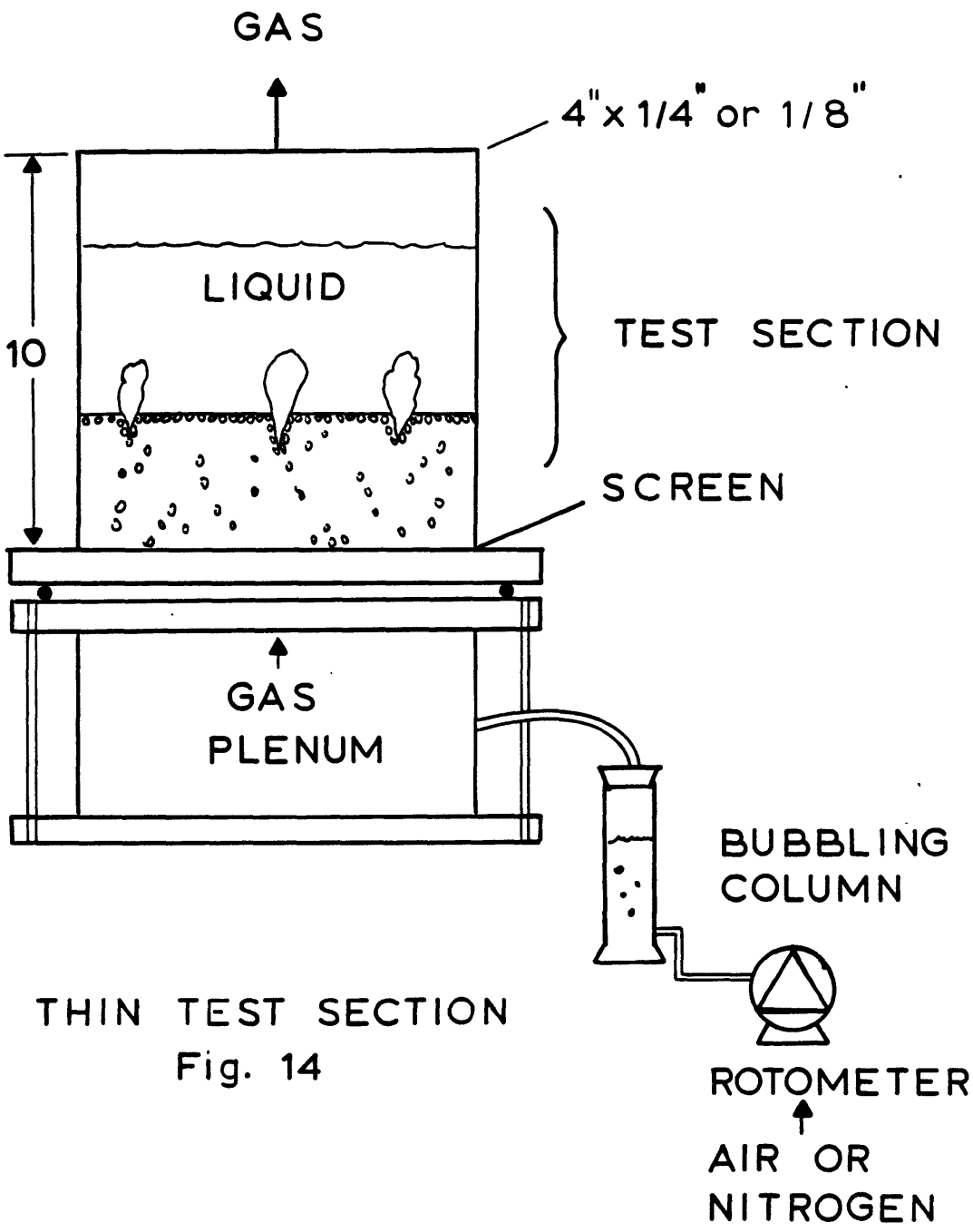

THIN TEST SECTION
Fig. 14

tapped several times to help the solids settle further. The particles, although smaller than the openings in the screen, did not pass through because of the surface tension of the liquid.

During the experiment, gas (air or nitrogen) was piped into the plenum after being saturated with the liquid vapor in the bubbling column. From the plenum, the gas penetrated the mesh, percolated through the particulate bed, bubbled into the overlying liquid pool, and escaped through the top of the test section to the atmosphere.

Initially, spherical glass shot were used in the hope that the translucent nature of the glass-liquid matrix would make the identification of channels easier. This did not prove to be the case. Individual channels were frequently smaller than the test section thickness, and were difficult to see. However, two distinct saturation zones (Figs. 15, 16, 17) could be seen. The upper zone was completely saturated with liquid. The saturation of the lower zone decreased with increasing gas flow rate. With one exception, the depth of top zone did not change with gas flow rate.

To evaluate the significance of this observed double zone, consider the differential equation for saturation in the unchanneled zone as it applies to this experiment.

$$\frac{dS}{dz} = \left(\frac{1}{\frac{dP}{dS}\sqrt{\varepsilon/k}}\right)\left\{\frac{1}{\sigma\cos\theta}\left[(\rho_\ell - \rho_v)g + \frac{1}{k}\left(\frac{\mu_\ell}{k_\ell}q_\ell - \frac{\mu_v}{k_v}q_v\right) + \frac{1}{\kappa}\left(\frac{\rho_\ell}{\kappa_\ell}|q_\ell|q_\ell - \frac{\rho_v}{\kappa_v}|q_v|q_v\right)\right] - P\,\frac{d\sqrt{\varepsilon/k}}{dz}\right\} \qquad 3.17$$

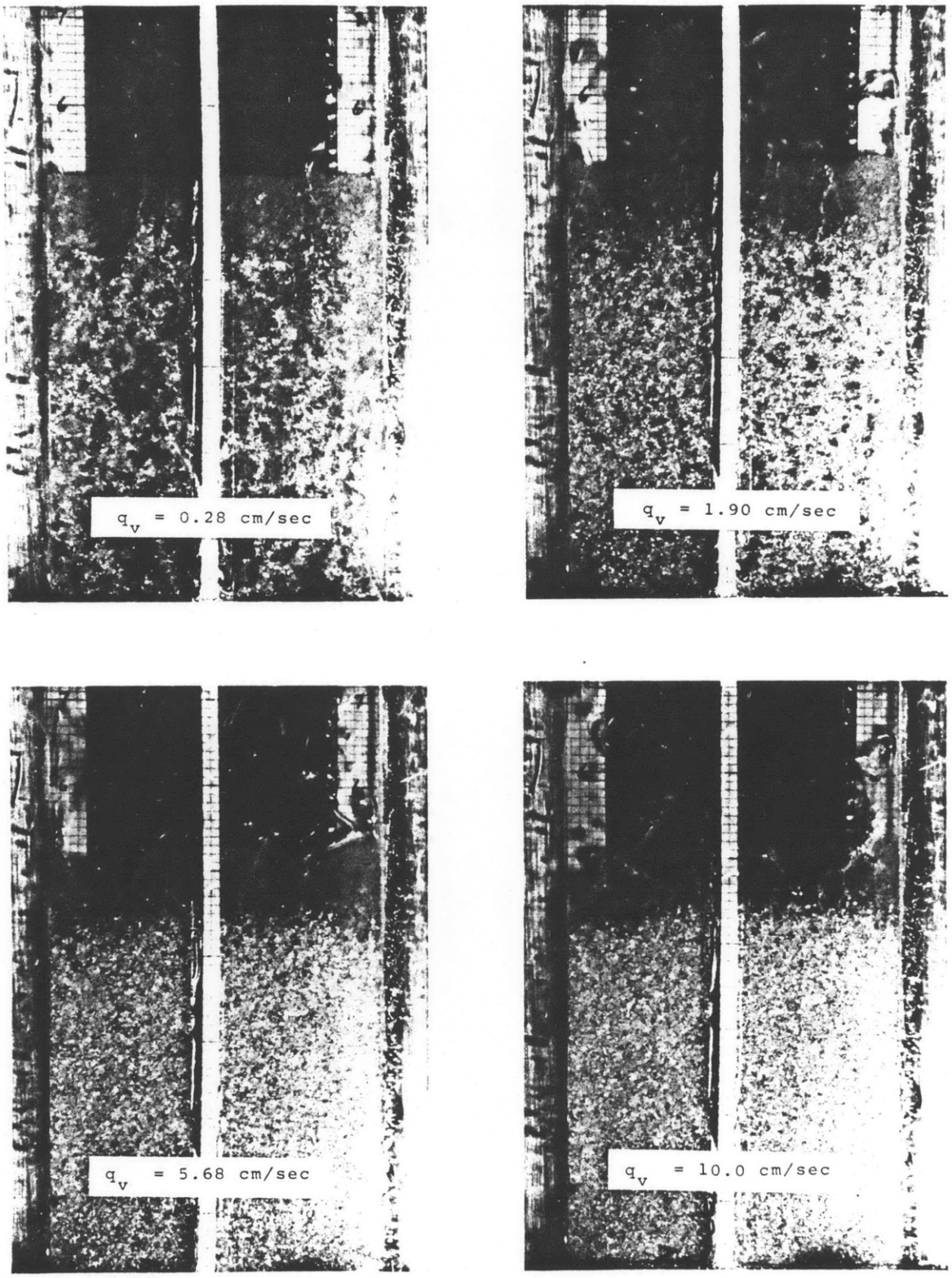

Fig. 15. Gas Flow in Unconsolidated Alcohol-Glass Matrix ($\overline{d}$ = 651 μm)

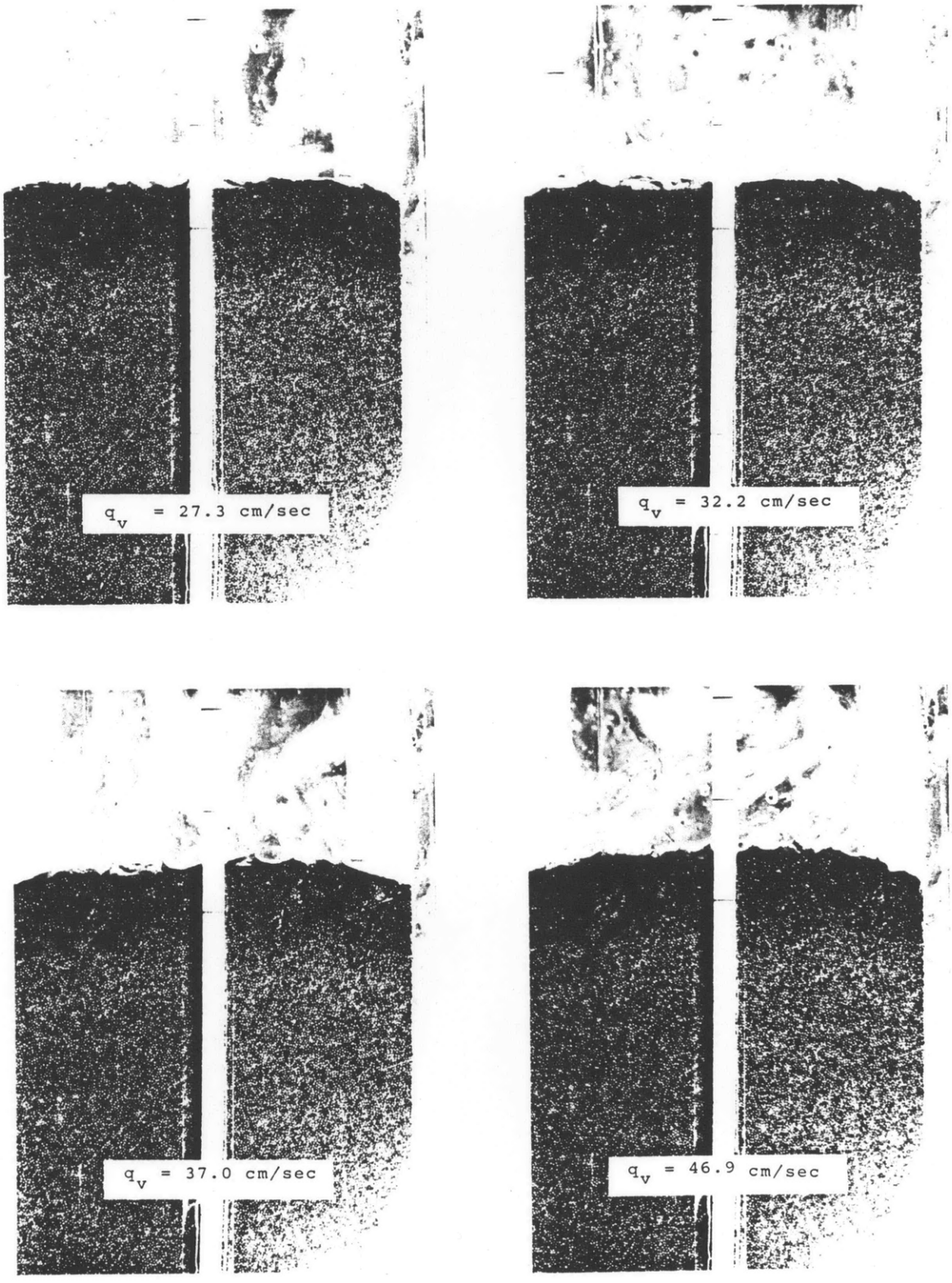

Fig. 16. Gas Flow in Unconsolidated Water-Iron Matrix ($\overline{d}$ = 651 μm)

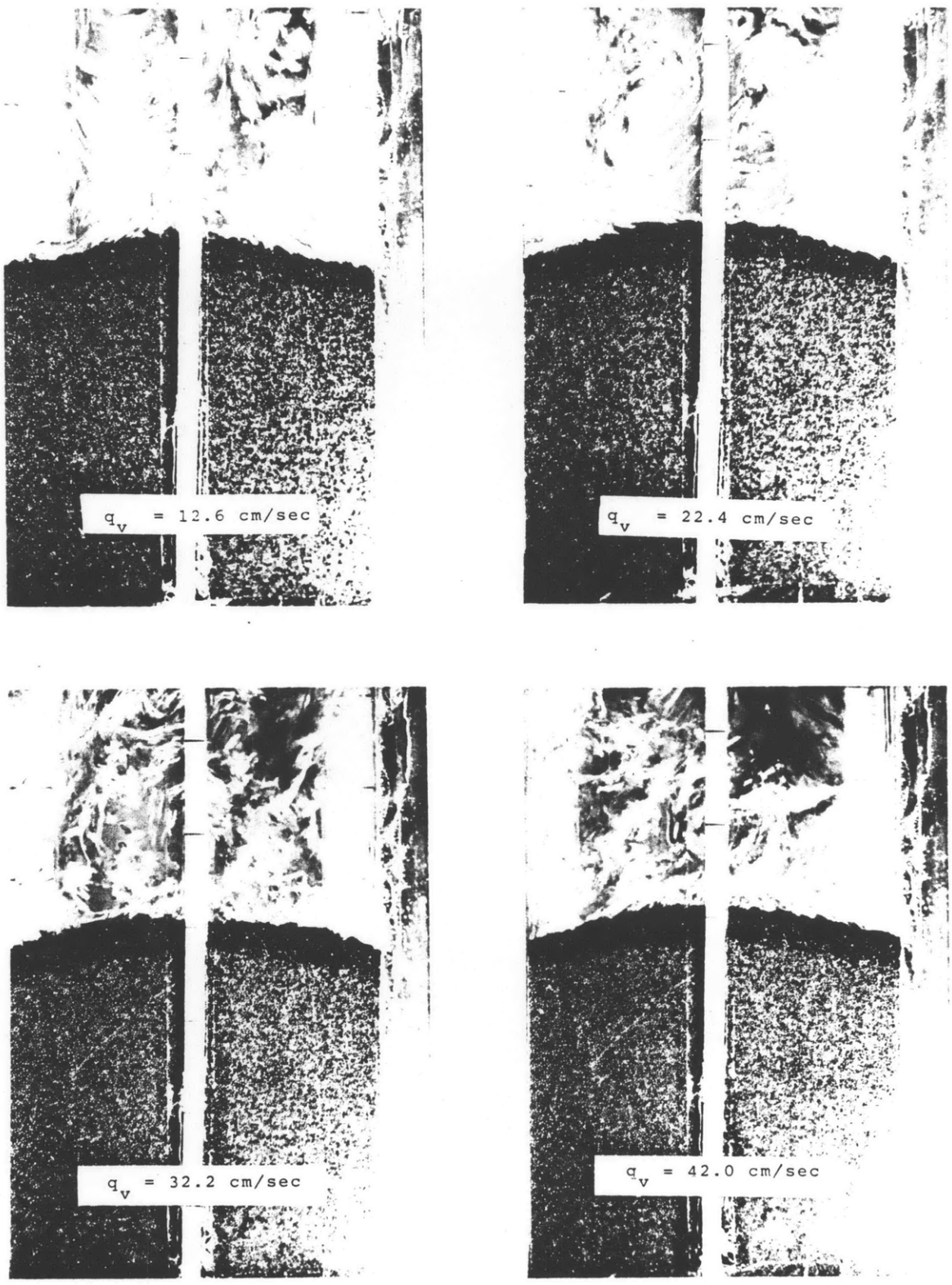

Fig. 17. Gas Flow in Unconsolidated Alcohol-Iron Matrix ($\overline{d}$ = 651 μm)

In the vicinity of the bottom of the channels, the saturation approaches unity. This forces the vapor relative permeabilities to approach zero and therefore cause the saturation gradient to be a large negative number. Away from the channels, the saturation gradient drops in magnitude and becomes more dependent on the gas flow rate. It can therefore be concluded that the interface between the two zones corresponds to bottom of the channels.

Plots of channel depth as a function particle diameter are shown in Figures 18 and 19. The solid line is the analytical prediction of channel depth assuming a stress ratio of unity. For this case

$$h = h_o \quad \frac{P_c \ (S = 0.99)}{(\rho_s - \rho_\ell)(1 - \varepsilon)g} \quad . \qquad 3.18$$

Using equation 2.5 and 2.8 for P_c and equation 2.2 for k, the channel depth reduces to

$$h = \frac{0.3771 \sqrt{150} \ \sigma \cos\theta}{(\rho_s - \rho_\ell) g \ d \ \varepsilon} \qquad 3.19$$

The predictions shown in Figures 18 and 19 are based on a zero contact angle. The iron-water data would be better fitted if a 45^o contact angle were assumed.

A stress ratio of unity carries with it an interesting implication. The Mohr's circle for this state reduces to a point. No shear forces exist in any coordinate frame. A fluid is a material which is unable to statically maintain a shear force. Hence the solid matrix might be expected to behave like a fluid.

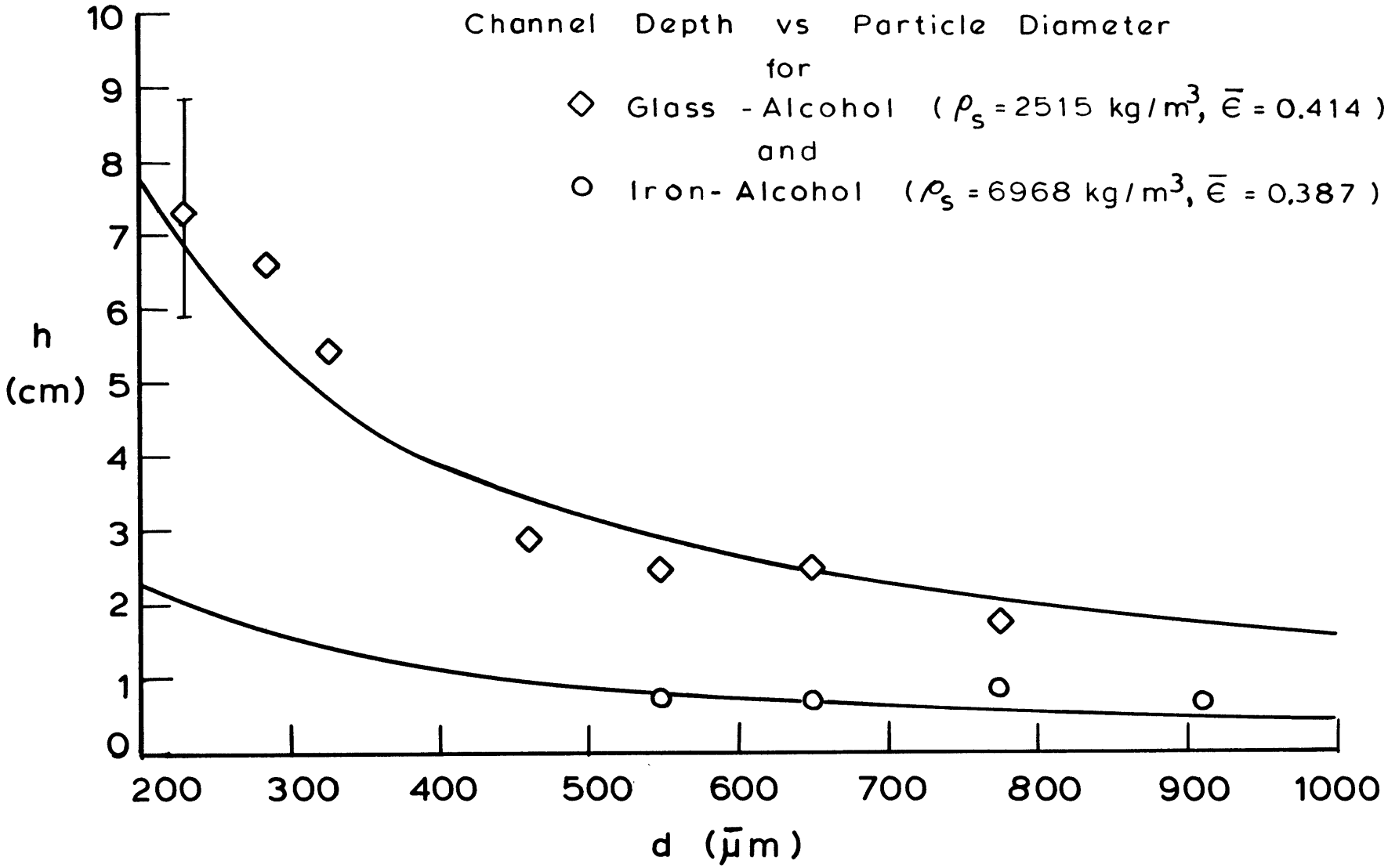
Channel Depth vs Particle Diameter
for
◇ Glass - Alcohol (ρ_s = 2515 kg/m^3, $\bar{\epsilon}$ = 0.414)
and
○ Iron - Alcohol (ρ_s = 6968 kg/m^3, $\bar{\epsilon}$ = 0.387)
h (cm)
0
1
2
3
4
5
6
7
8
9
10
200
300
400
500
600
700
800
900
1000
d (μm)

Fig 18

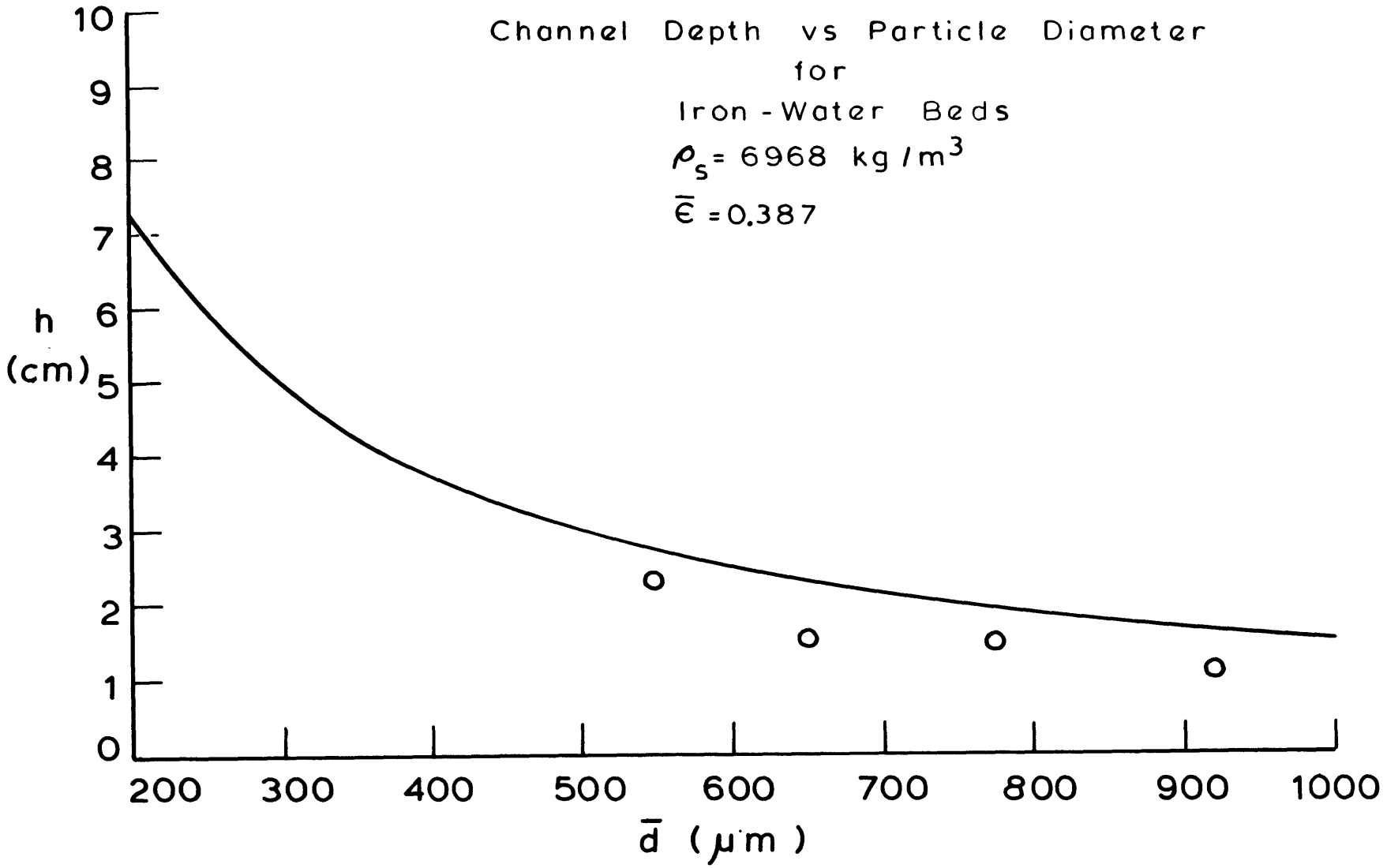
Channel Depth vs Particle Diameter
for
Iron - Water Beds
ρ_s = 6968 kg / m^3
$\bar{\epsilon}$ = 0.387
h (cm)
10
9
8
7
6
5
4
3
2
1
0
200
300
400
500
600
700
800
900
1000
$\bar{d}$ (μm)

Fig 19

The absence of shear forces can be explained mechanisticly. The channeled region is characterized by vigorous particle motion where the vapor enters the overlying liquid pool. The channels alternately expand and collapse at a high frequency. If these motions cause the particles to bounce against each other, then frictional forces can not be transmitted between particles because of the lack of sustained contact. Without these frictional forces, the solid matrix cannot maintain a shear force.

This model explains a number of observations. In previous test sections, a channel would sometimes form against the transparent wall. Frequently, a particle at the channel wall was spinning. The drag force from the vapor in the channel produced a torque on the particle. In the absence of any frictional forces from neighboring particles, the observed particle was free to spin.

Secondly, the analytical model was originally based on a vertical channel. However, channels exist at all angles, including the horizontal. The analysis remains unchanged for inclined channels in the absence of solid shear forces.

Finally, the model addresses the problem of fluidization in the channeled region. The region is not fluidized in the classical sense. However, the solid matrix cannot maintain a shear force statically, and therefore takes on the appearance of a fluid.

The obvious omissions from Figures 18 and 19 are data from a glass shot-water test. This combination yielded unstable channels. At gas superficial velocities of less than about 20 cm/sec, the flow seemed to behave similarly to other systems. When the gas flow was increased, one channel would begin to propagate downward. A fully saturated zone surrounded the propagating channel. When the channel reached the bottom of the bed, the plenum pressure dropped rapidly and the channel collapsed. The plenum pressure would then increase until the channel opened, and the pressure once again dropped. This "burping" is characteristic of a channel which has penetrated a gas pocket.

The cause of the instability is unknown. Two parameters were changed when water was substituted for alcohol in the glass shot bed. The glass-liquid density difference decreased by 12% and the surface tension increased by a factor of 3. However, when iron shot was used with water, the increased solid-liquid density difference suppressed the instability. Liquid sodium has a surface tension which is two to four times greater than that of water. Whether or not this will result in unstable channels in sodium-fuel debris beds is unknown.

Some final remarks about particle motion at the surface of the bed are in order. It has been observed that particles were blown out of the channel. The number of these particles was small. However, the bubbles rising through the pool created secondary flows in the liquid, When the velocity of the liquid in the pools reached the

terminal velocity of the particles at the bed surface, particles were entrained by the liquid. These were carried up the bubble stream and deposited away from the channel (Fig. 20).

When the vapor flux was sufficiently high and the particles sufficiently small, mounds were created where the particles were deposited. When these grew tall enough, particles would flow down the slope back to the vapor channel where they were entrained again. When the vapor flow was shut off, the smaller particles were the last to settle and formed a layer of fines on the top of the bed.

It is possible for the particle entrainment to be significant. Mounds approximately 1/2" high were observed when iron shot was used. The height was obviously affected by the test section width. Larger mounds were observed with glass shot beds. In a separate experiment, in which a nichcome robbon was placed at the bottom of a 3" high, 75 μm glass shot bed immersed in Freon II, the entire bed was fluidized by the secondary flows in the liquid freon pool. Whether or not mounds will form in three dimensional beds is not clear.

Flow Equations in the Channeled Region

If it is assumed that the cross-sectional area of the vapor channels is negligible, then equation (2.3) for liquid pressure drop applies. The reported[4,9] channel density and diameter were about 1 channel every 4 cm^2 and 0.25 cm respectively. The channel cross-sectional area accounts for about 1.3% of the total cross-sectional area. The assumption seems justifiable.

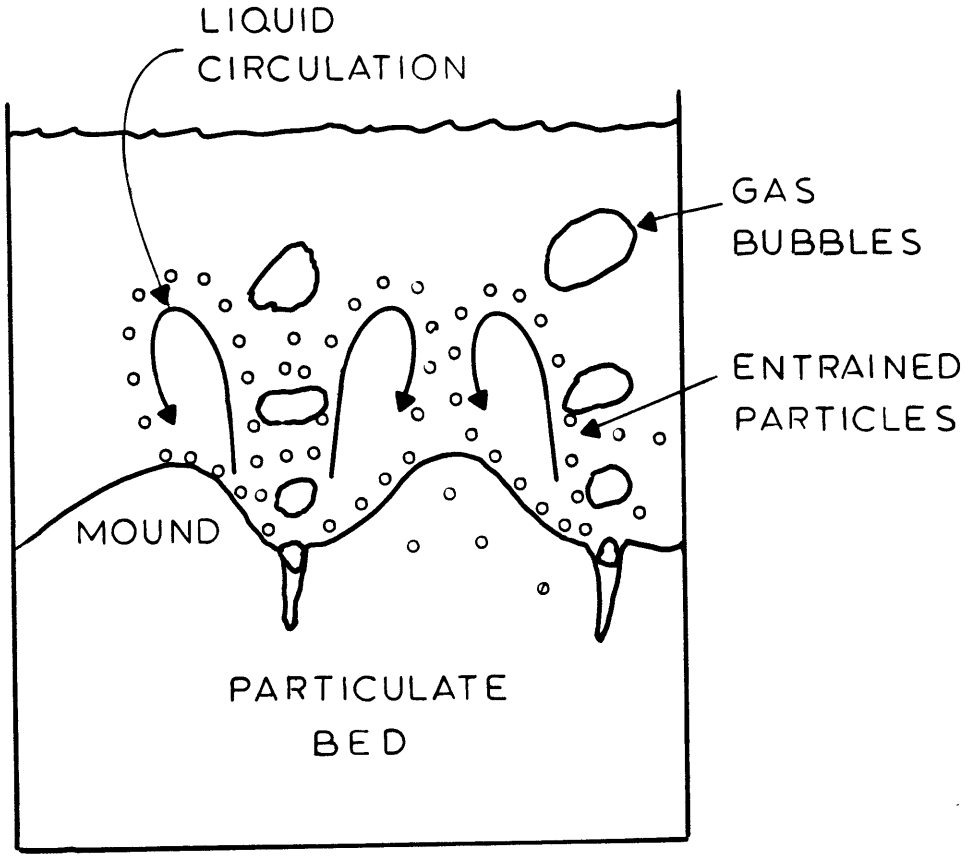

Fig. 20 Mound Formation in a Debris Bed

IV. RESULTS

The results of sections II and III were combined to form a one-dimensional, two region model of a debris bed. A program was developed (Appendix III) which, for a given bed geometry, determined the saturation profile as a function of heating rate. The heating rate was varied in the program until dryout, as defined in Appendix II, was obtained.

Predicted saturation profiles for two different bed geometries are plotted in Figures 21 and 22. The channeled region at the top has a saturation of unity. Since the beds differ in height only, the channel depths for the two cases are the same. The channels' impact is far greater on the smaller bed because they occupy a higher percentage of the bed.

Immediately below the channeled region is a severe saturation gradient which sits at the top of the unchanneled region. At power levels below those required for dryout, the saturation profile tends to be concave. Within a very small range of energy generation rates, the saturation profile changes drastically and the bottom of the bed dries out.

These characteristics can be used to explain the initiation of dryout at a point above the bottom of the bed. Suppose a power level has been set in an experiment which is a few percent below the dryout point. A concave saturation profile will exist. Then suppose that the power level is increased to a few percent above the dryout point.

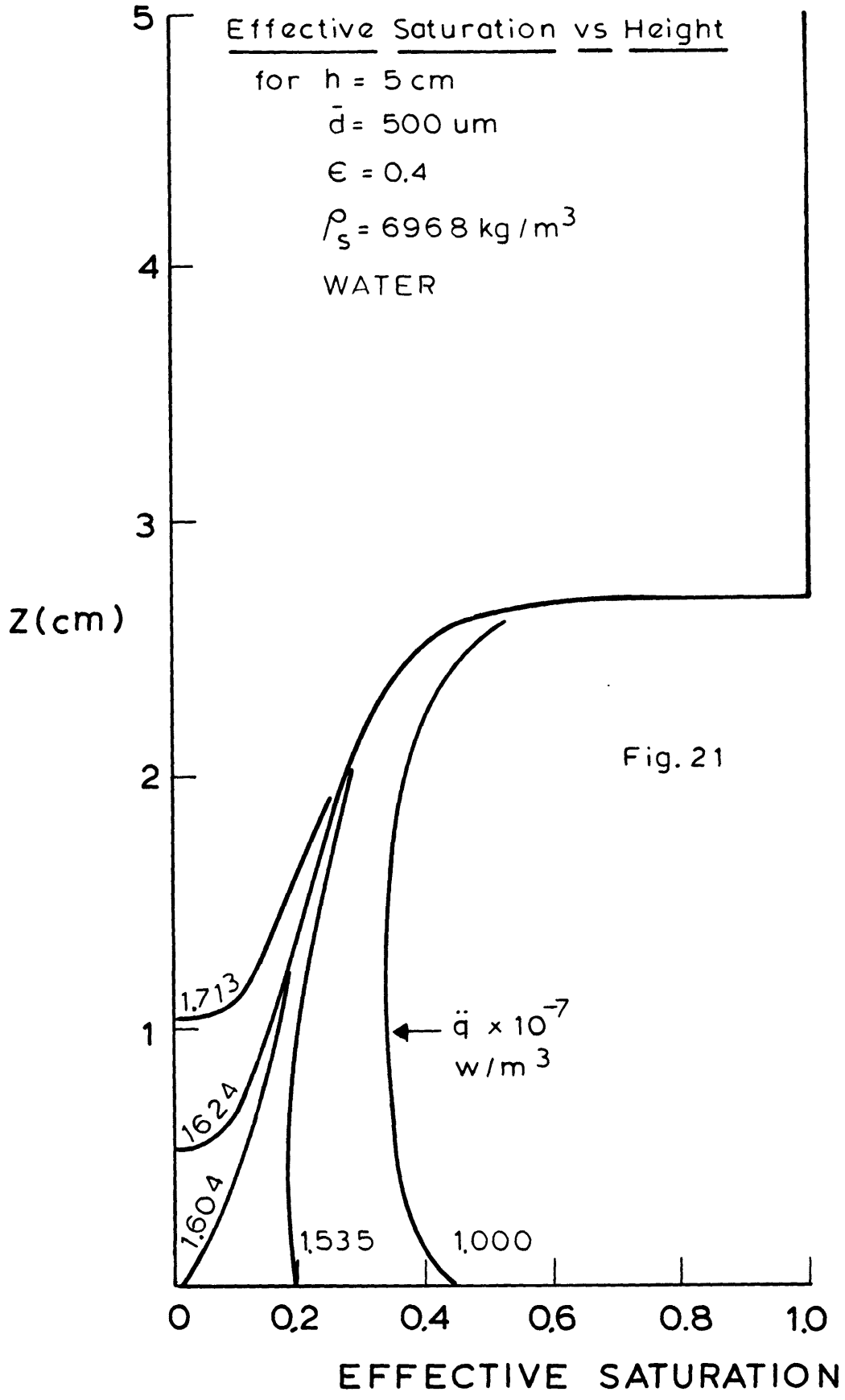
Effective Saturation vs Height
for h = 5 cm
d̄ = 500 um
ϵ = 0.4
ρs = 6968 kg/m3
WATER
Z(cm)
5
4
3
2
1
0
0.2
0.4
0.6
0.8
1.0
EFFECTIVE SATURATION
1.713
1.624
1.604
1.535
1.000
q̈ x 10-7
w/m3

Fig. 21

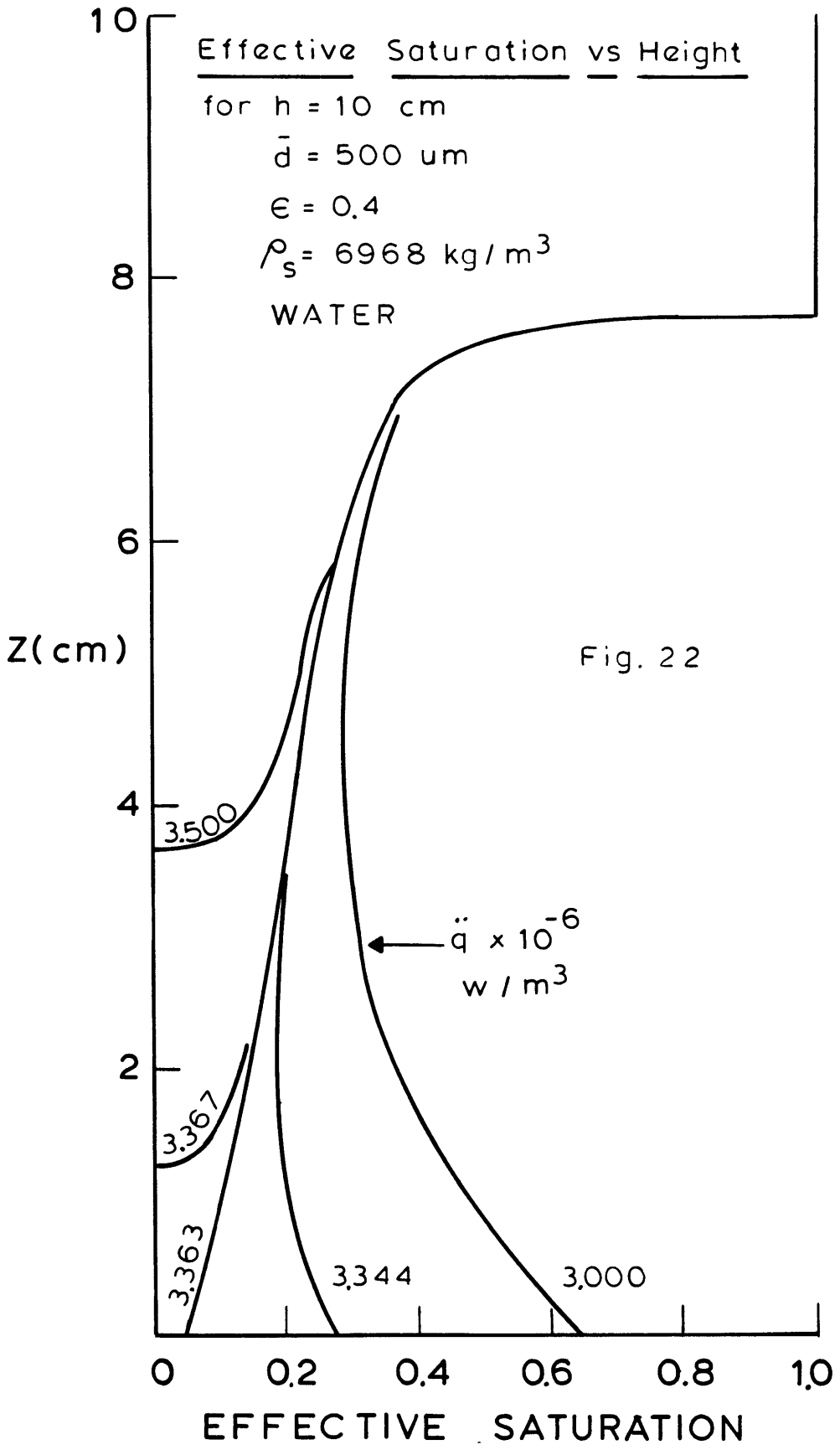
Effective Saturation vs Height
for h = 10 cm
$\bar{d}$ = 500 um
ϵ = 0.4
ρ_s = 6968 kg/m^3
WATER
10
8
6
4
2
Z(cm)
3.500
3.367
3.363
3.344
3.000
$\ddot{q}$ x 10^{-6}
w/m^3
0
0.2
0.4
0.6
0.8
1.0
EFFECTIVE SATURATION

Fig. 22

The saturation curve must change drastically. It is quite possible that, during the transient, the former point of minimum saturation will be the first to reach a zero saturation. The rest of the bed below this level should reach dryout in a matter of minutes. This behavior was first predicted by Lipinski.[16]

Plots of predicted vs measured dryout powers are shown in Figures 23 through 42. The experimental data is taken from the works of Keowen,[31] Dhir and Catton[31], and Trenberth and Stevens.[12] Four predictions are made for each data set. The relative permeabilities, based on the works of Burdine and Brooks and Corey (eqns. 2.11 and 2.14), are used in two predictions. Those cited in Scheidegger and used by Lipinski (eqns. 2.10 and 2.13) are used in the others. A channeled and an unchanneled model are used with each relative permeability model.

In general, a channeled model predicts a higher dryout flux than an unchanneled model. The magnitude of the difference depends on the bed depth and average particle size. Channels are most important in shallow beds of small particles. Also, the model using Scheidegger/ Lipinski relative permeabilities predicts greater dryout fluxes than the Brooks and Corey/Burdine model.

Keowen's experimental dryout fluxes are generally higher than the analytical predictions. The channeled model with the relative permeabilities recommended by Lipinski (Fig. 25) fits these data best. However, Dhir and Catton's later data reflect values of dryout fluxes below those of Keowen. For these data, the channeled model using the Brooks and Corey correlations (Figs. 27, 31, 35) and the

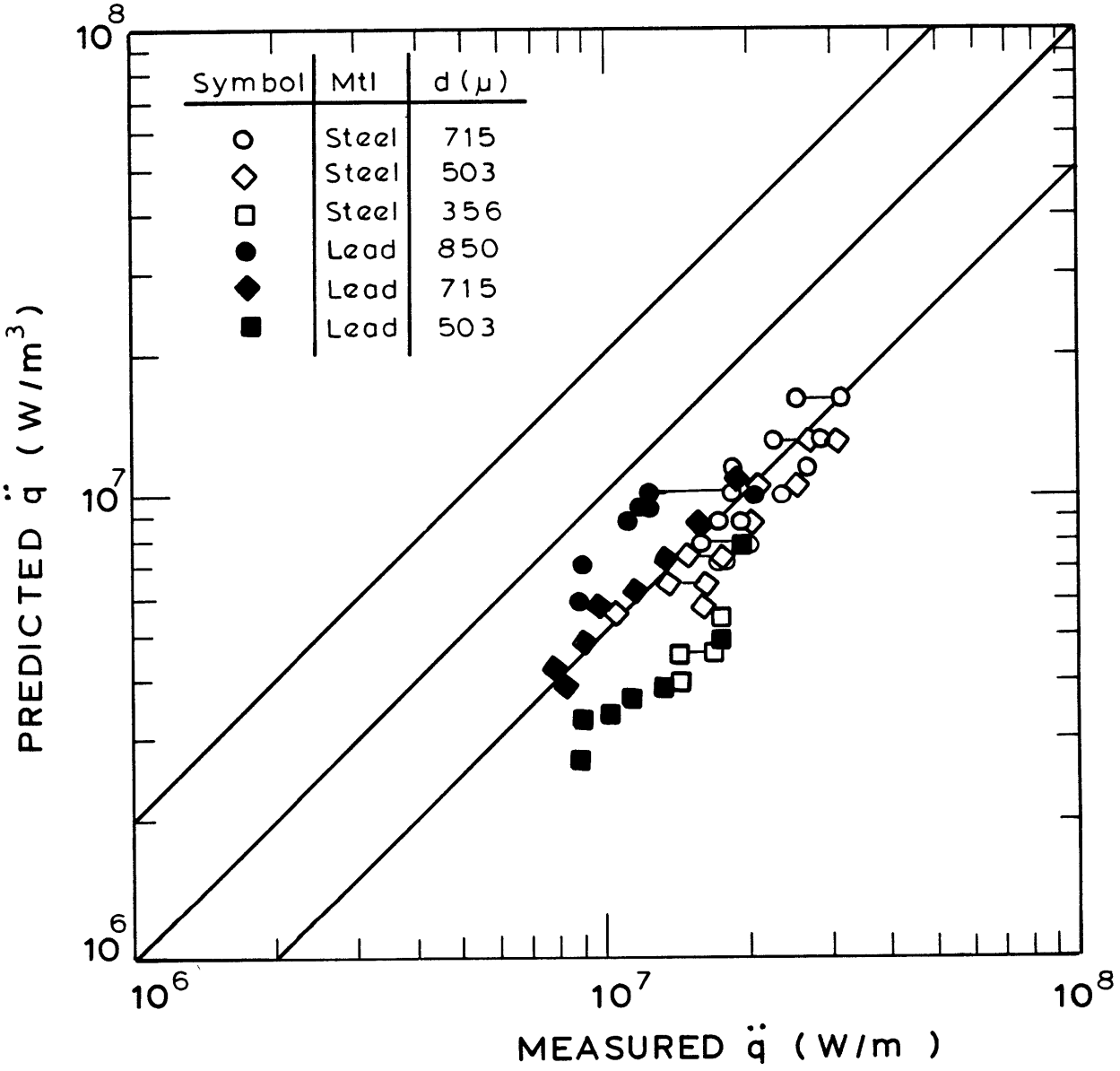

Fig 23. Keowen Data Channeled Model, $k_\ell = S_e^{3.486}$,

$k_v = (1 - S_e)^2(1 - S_e^{1.486})$, $K_\ell = S_e^{5.243}$,

$K_v = (1 - S_e)^3(1 - S_e^{1.7215})^2$

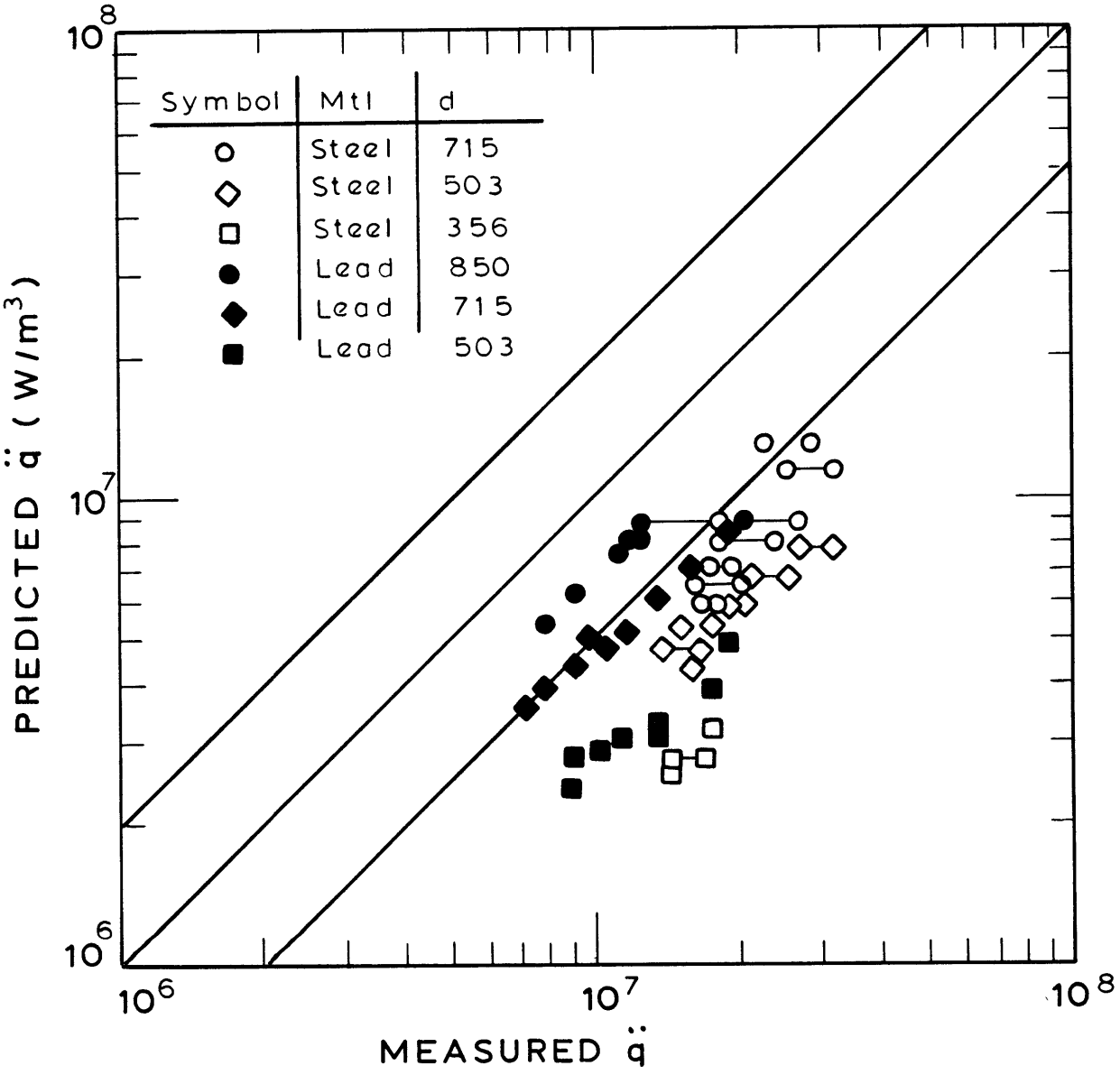

Fig 24 Keowen Data Unchanneled Model $k_\ell = S_e^{3.486}$

$k_v = (1 - S_e)^2 (1 - S_e^{1.486})$, $K_\ell = S_e^{5.243}$,

$K = (1 - S_e)^3 (1 - S_e^{1.1215})^2$

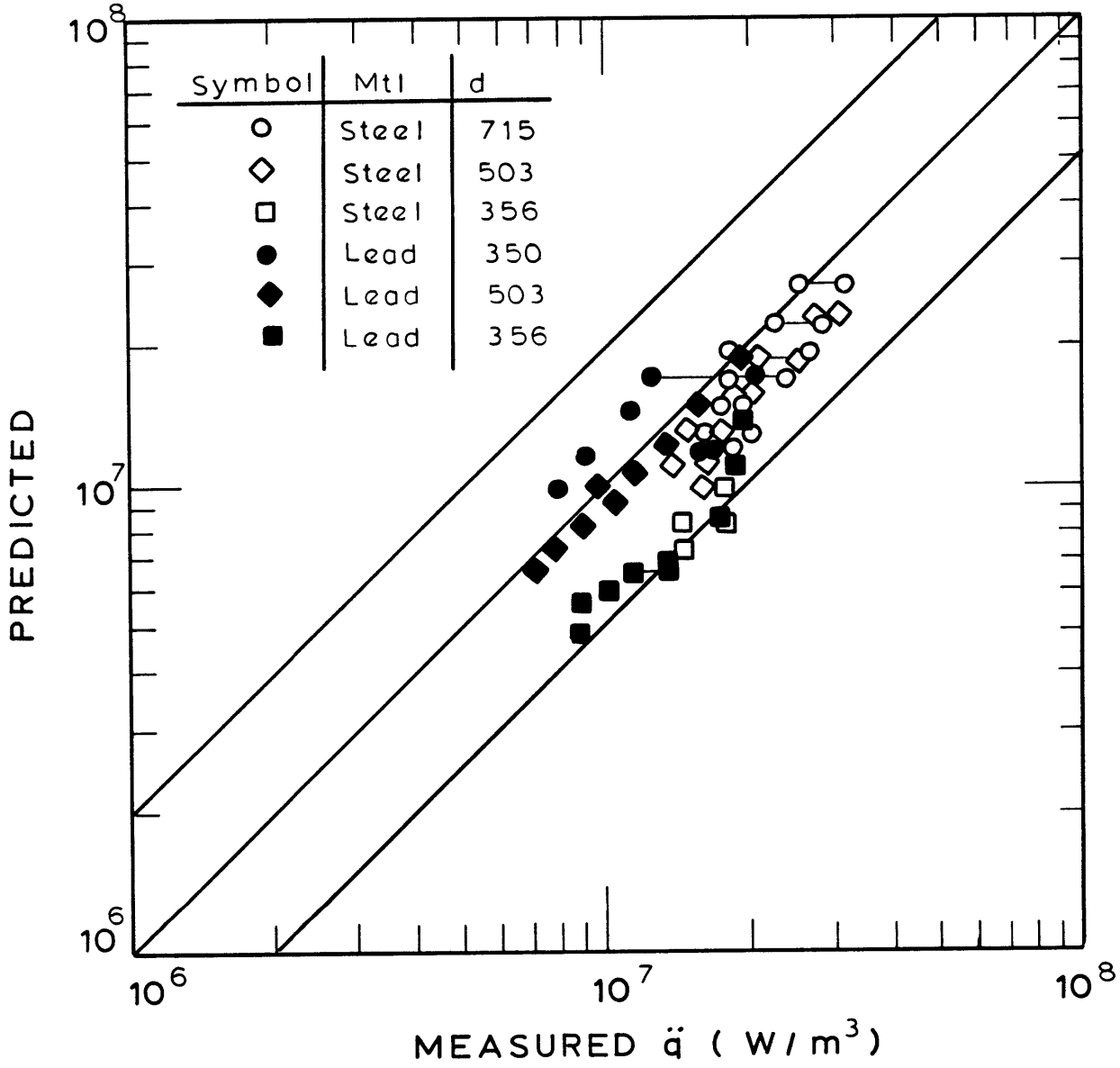

Fig 25 Keowen Data Channeled Model, $k_\ell = S^3$, $k_v = 1 - 1.11\ S$, $K_\ell = S^3$, $K_v = (1-S)^3$

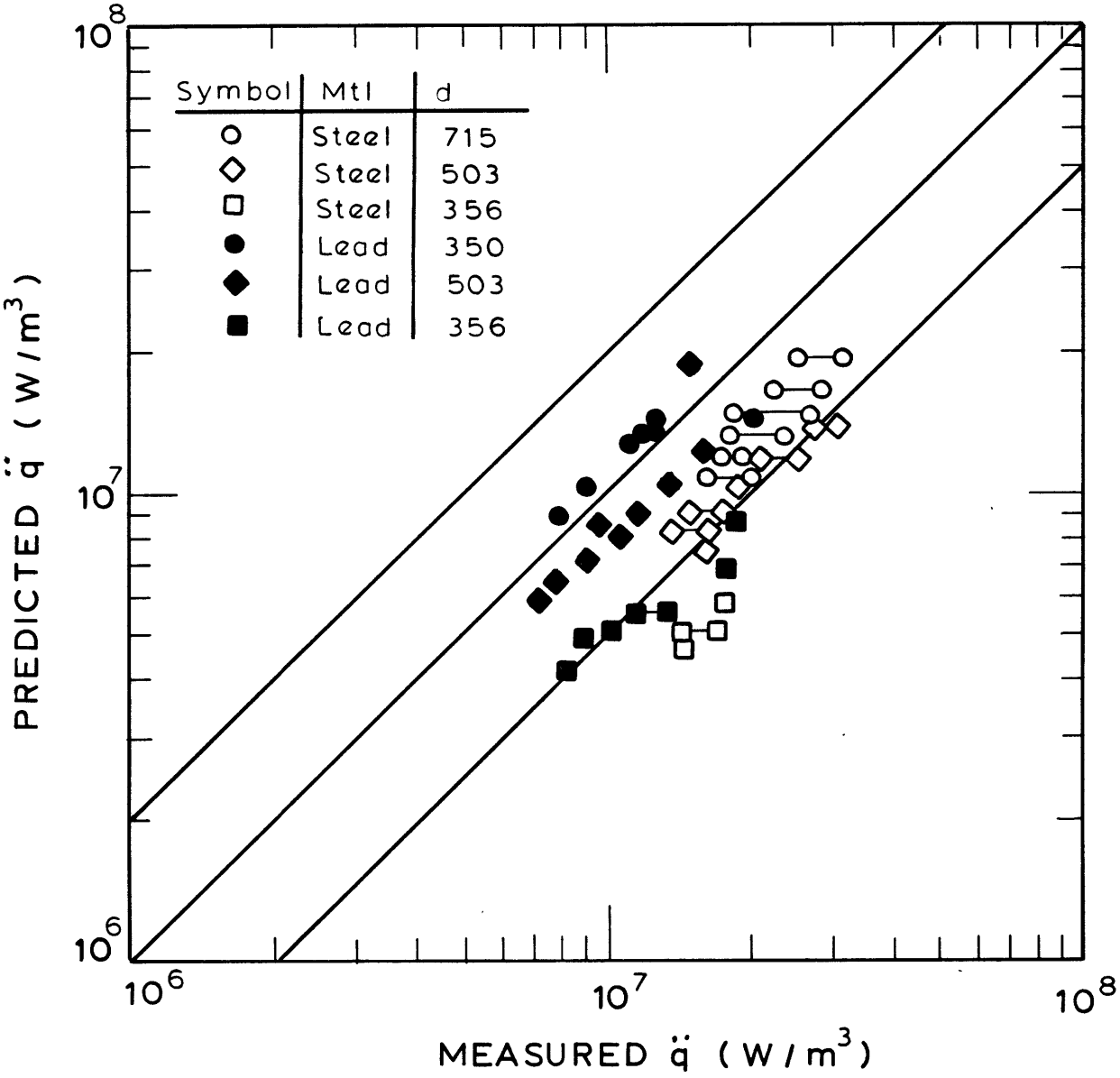

Fig 26 Keowen Data, $k_\ell = S_e^3$, $k_V = 1 - 1.11S$, $K_\ell = S^3$, $K_V = (1 - S)^3$

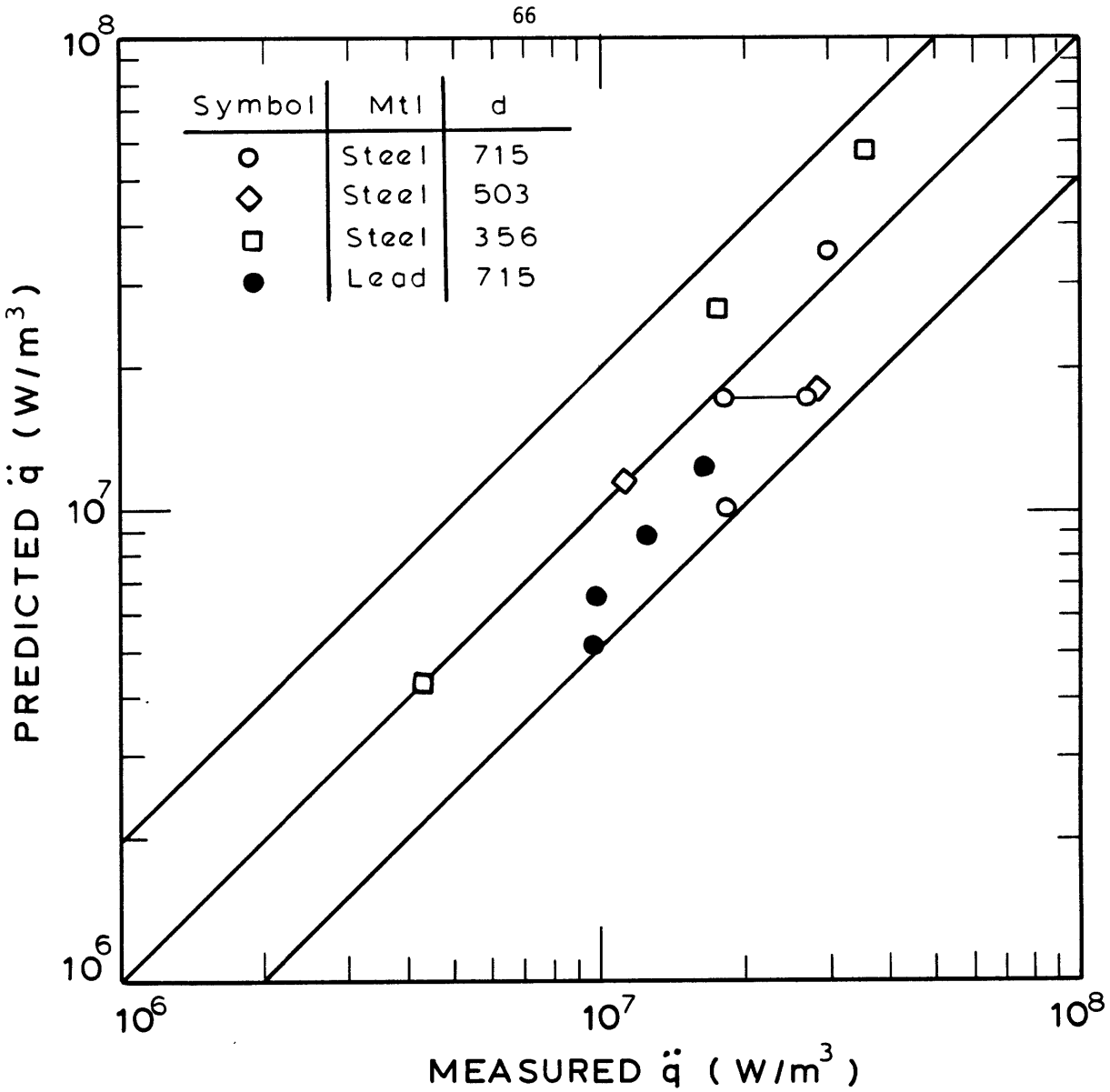

Fig 27 Dhir & Catton Data (Water) Channeled Model
$k_\ell = S_e^{3.486}$, $k_v = (1 - S_e)^2(1 - S_e^{1.486})$, $K_\ell = S_e^{5.243}$
$K_v = (1 - S_e)^3(1 - S_e^{1.1215})^2$

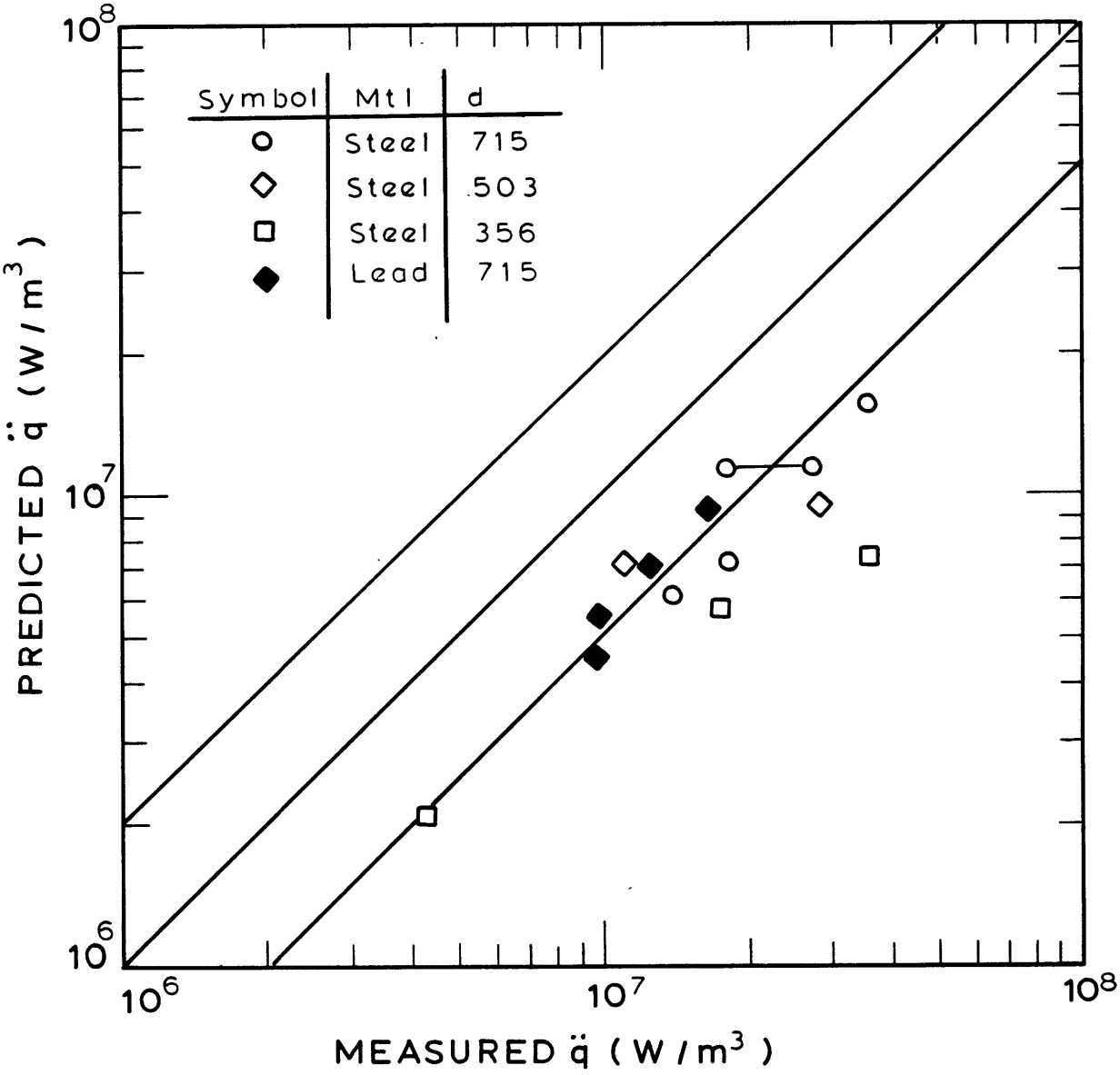

Fig 28 Dhir & Catton Data (Water) Unchanneled Model
$k_\ell = S_e^{3.486}$, $k_V = (1-S_e)^2(1-S_e^{1.486})$, $K_\ell = S_e^{5.243}$,
$K_V = (1-S_e)^3(1-S_e^{1.1215})^2$

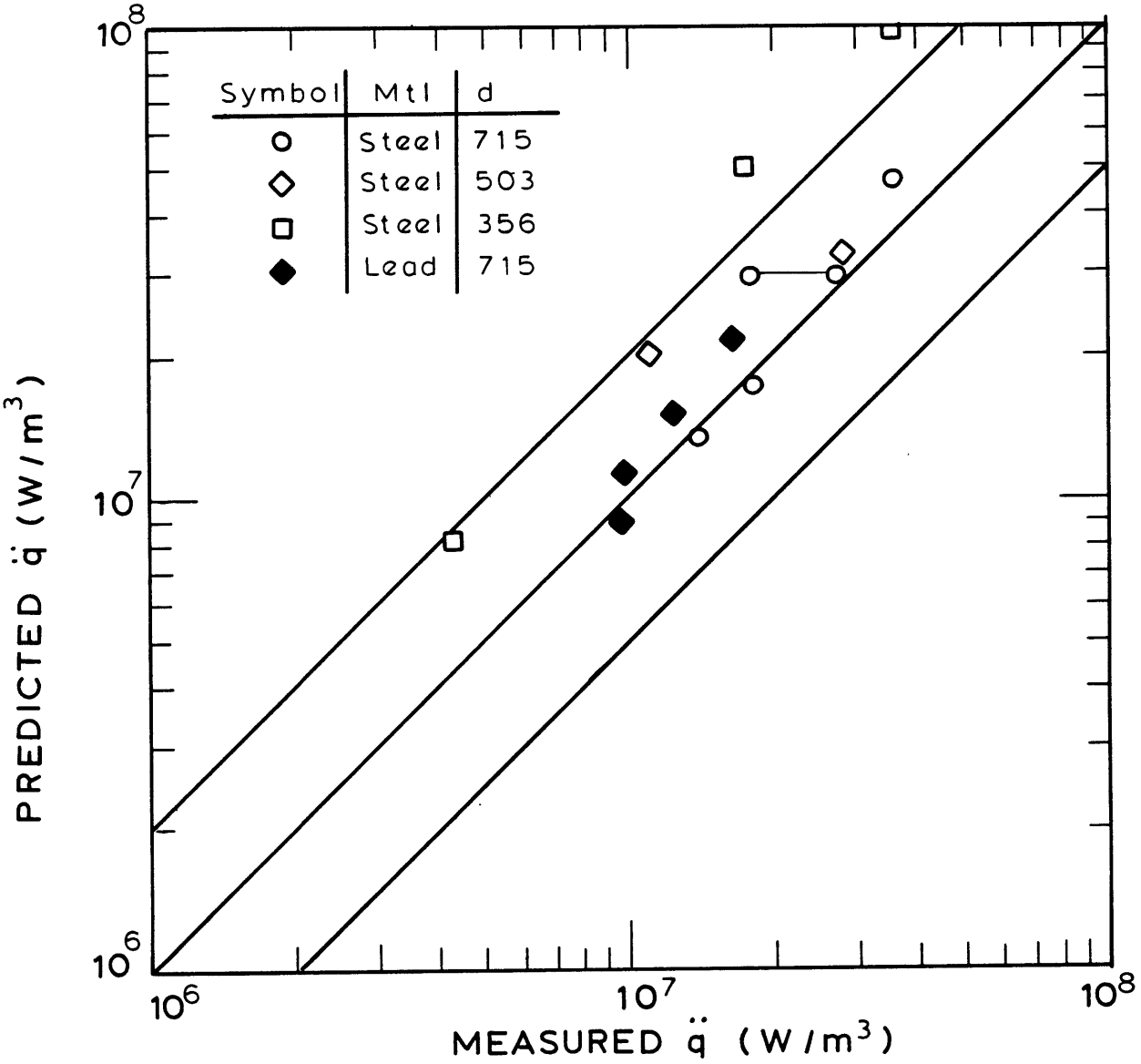

Fig 29 Dhir & Catton Data (Water) Channeled Model
$k_\ell = S^3$, $k_V = 1\text{-}1.11S$, $K_\ell = S^3$, $K_V = (1-S)^3$

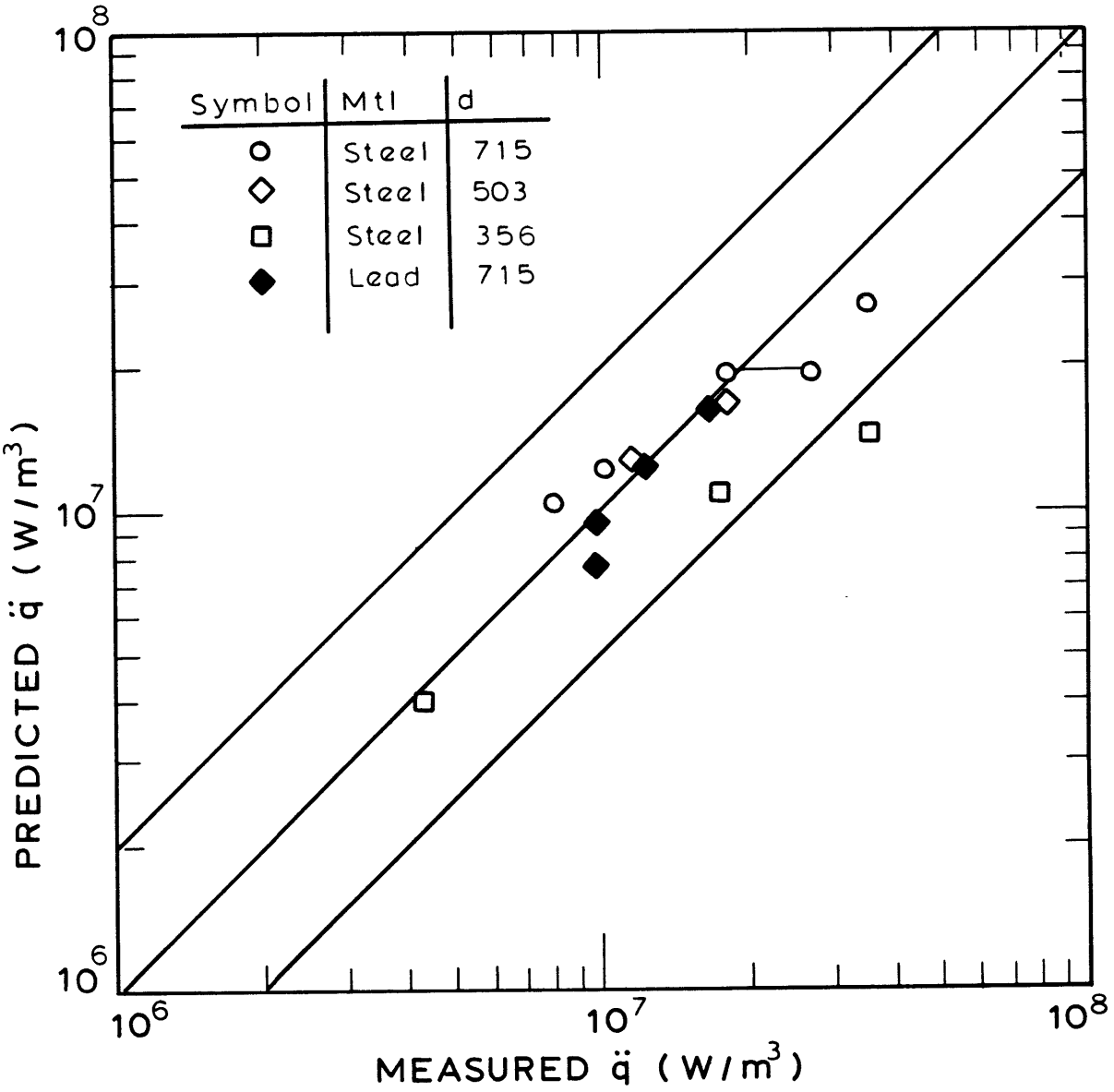

Fig 30 Dhir & Catton Data (Water) Unchanneled Model
$k_\ell = S^3$, $k_v = 1-1.11\,S$, $K_\ell = S^3$, $K_v = (1-S)^3$.

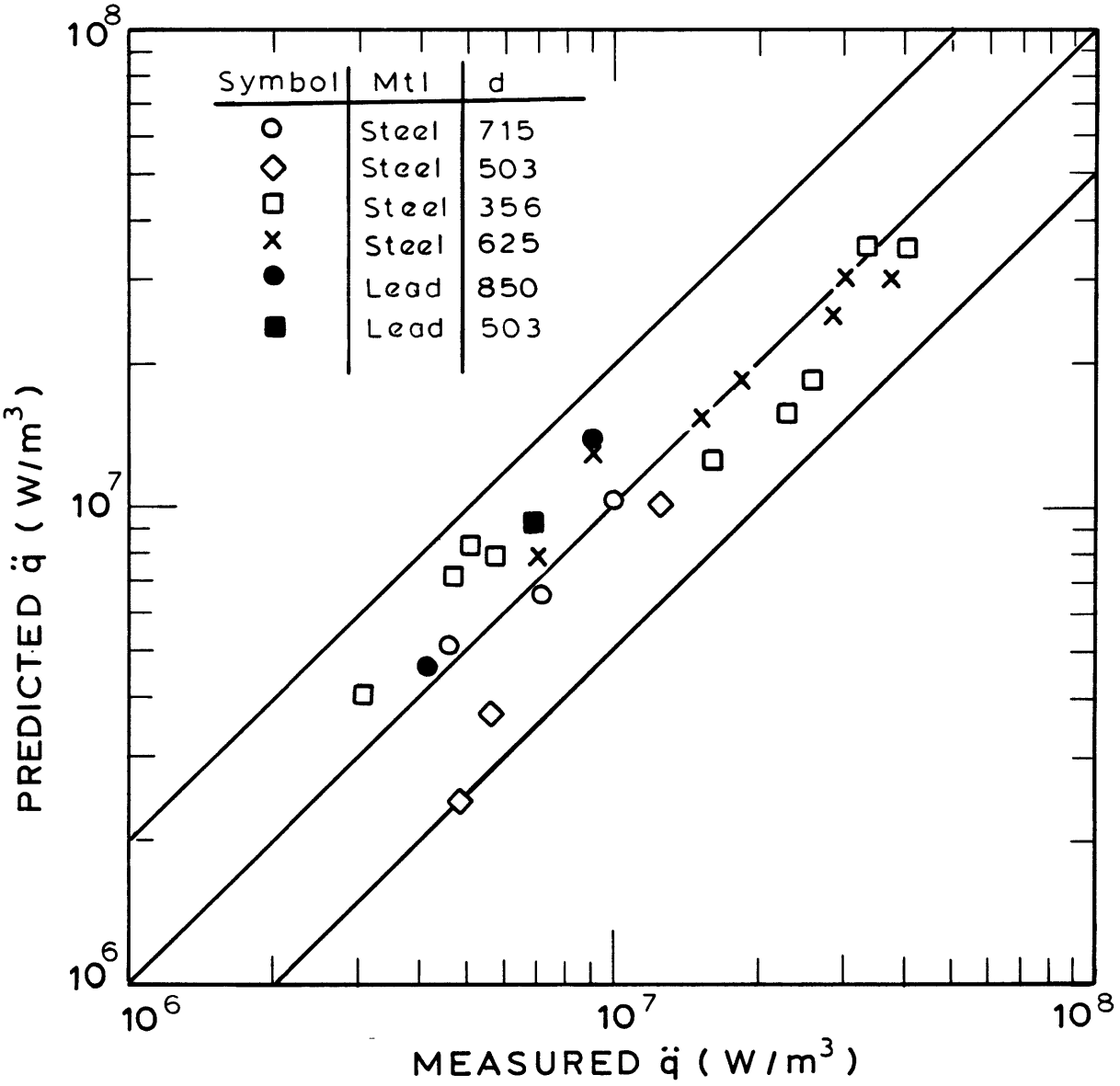

Fig 31 Dhir & Catton Data (Acetone) Channeled Model
$k_\ell = S_e^{3.486}$, $k_v = (1 - S_e)^2 (1 - S_e^{1.486})$, $K_\ell = S_e^{5.243}$,
$K_v = (1 - S_e)^3 (1 - S_e^{1.1215})^2$

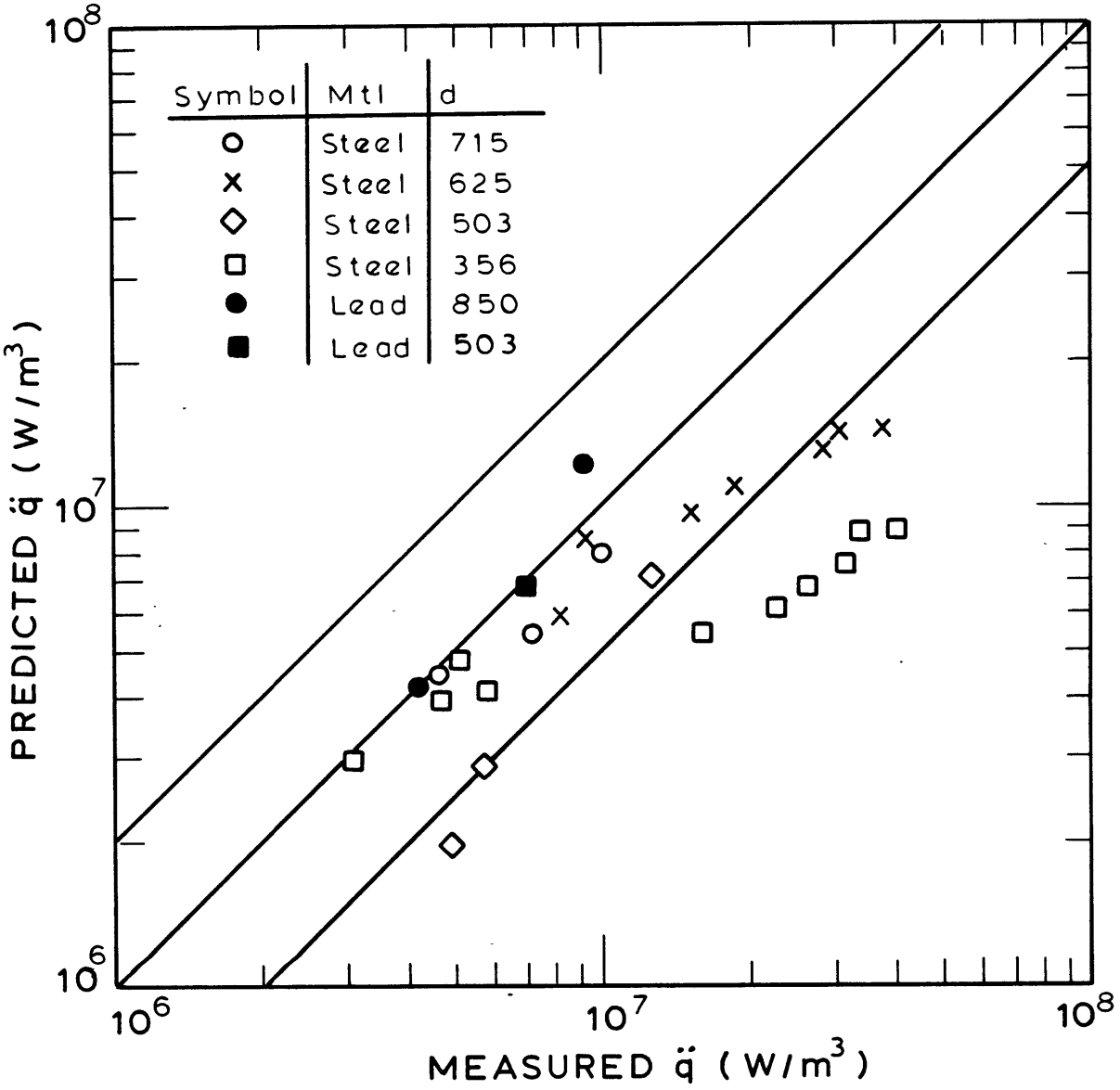

Fig 32 Dhir & Catton Data (Acetone) Unchanneled
Model $k_\ell = S_e^{3.486}$, $k_v = (1 - S_e)^2 (1 - S_e^{1.486})$,
$K_\ell = S_e^{5.243}$, $K_v = (1 - S_e)^3 (1 - S_e^{1.1215})^2$.

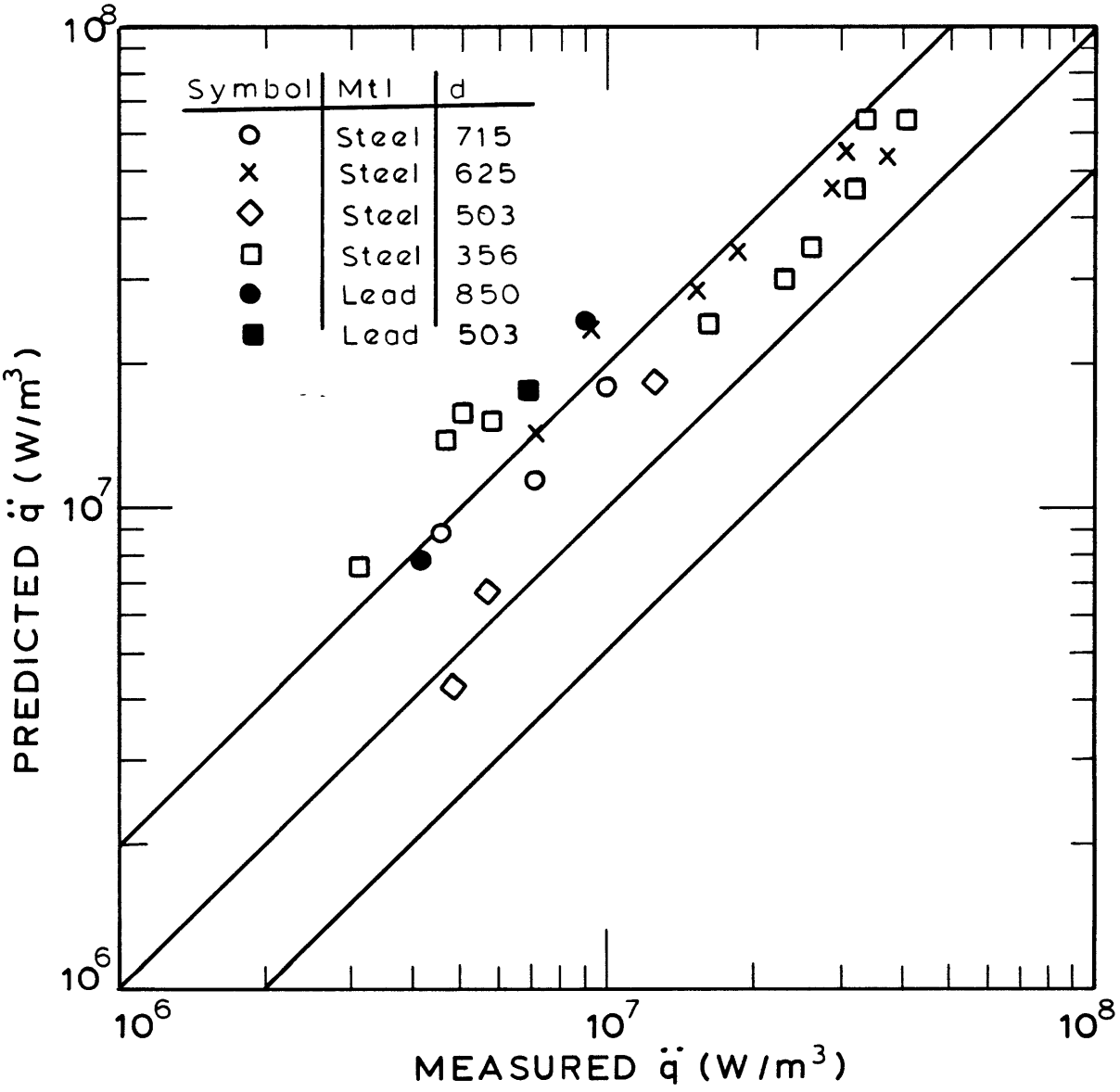

Fig 33 Dhir & Catton Data (Acetone) Channeled Model
$k_\ell = S^3$, $k_V = 1-1.11S$, $K_\ell = S$, $K_V = (1-S)^3$.

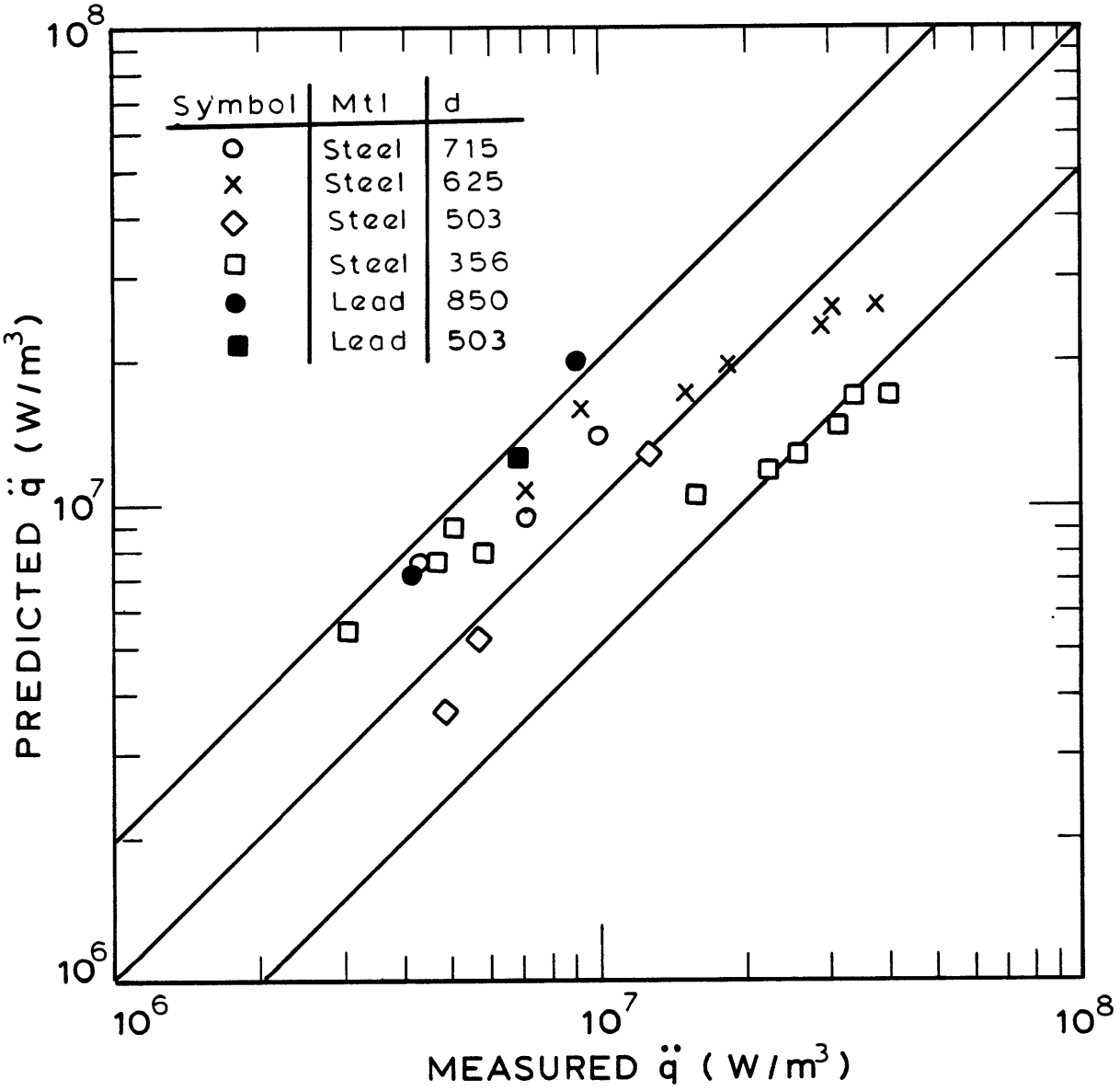

Fig 34 Dhir & Catton Data (Acetone) Unchanneled
Model $k_\ell = S^3$, $k_v = 1 - 1.11S$, $K_\ell = S$, $K_v = (1-S)^3$

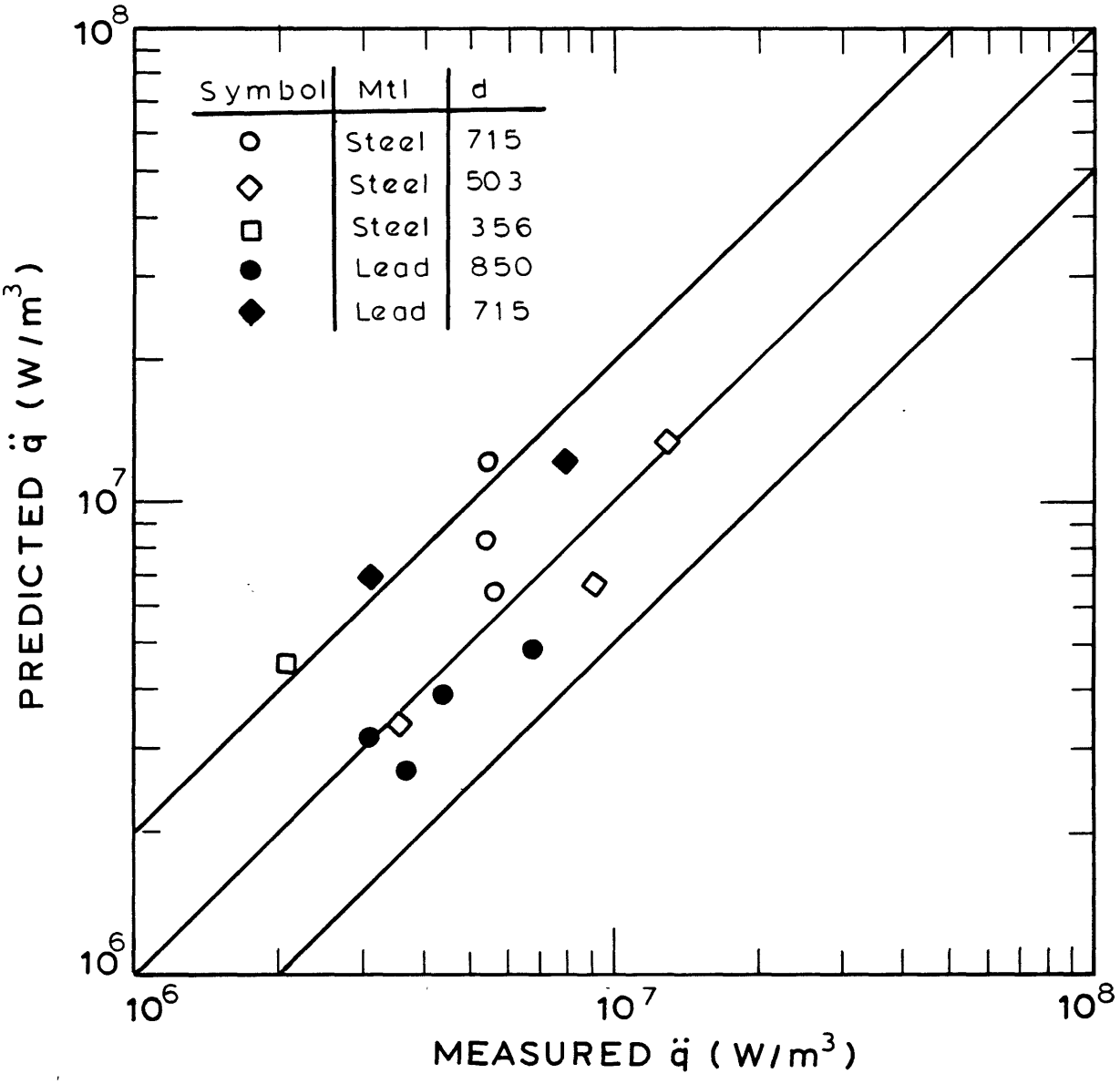

Fig 35 Dhir & Catton Data (Methanol) Channeled Model

$k_l = S_e^{3.486}$, $k_v = (1 - S_e)^2 (1 - S_e^{1.486})$, $K_l = S_e^{5.243}$,

$K_v = (1 - S_e)^3 (1 - S_e^{1.1215})^2$

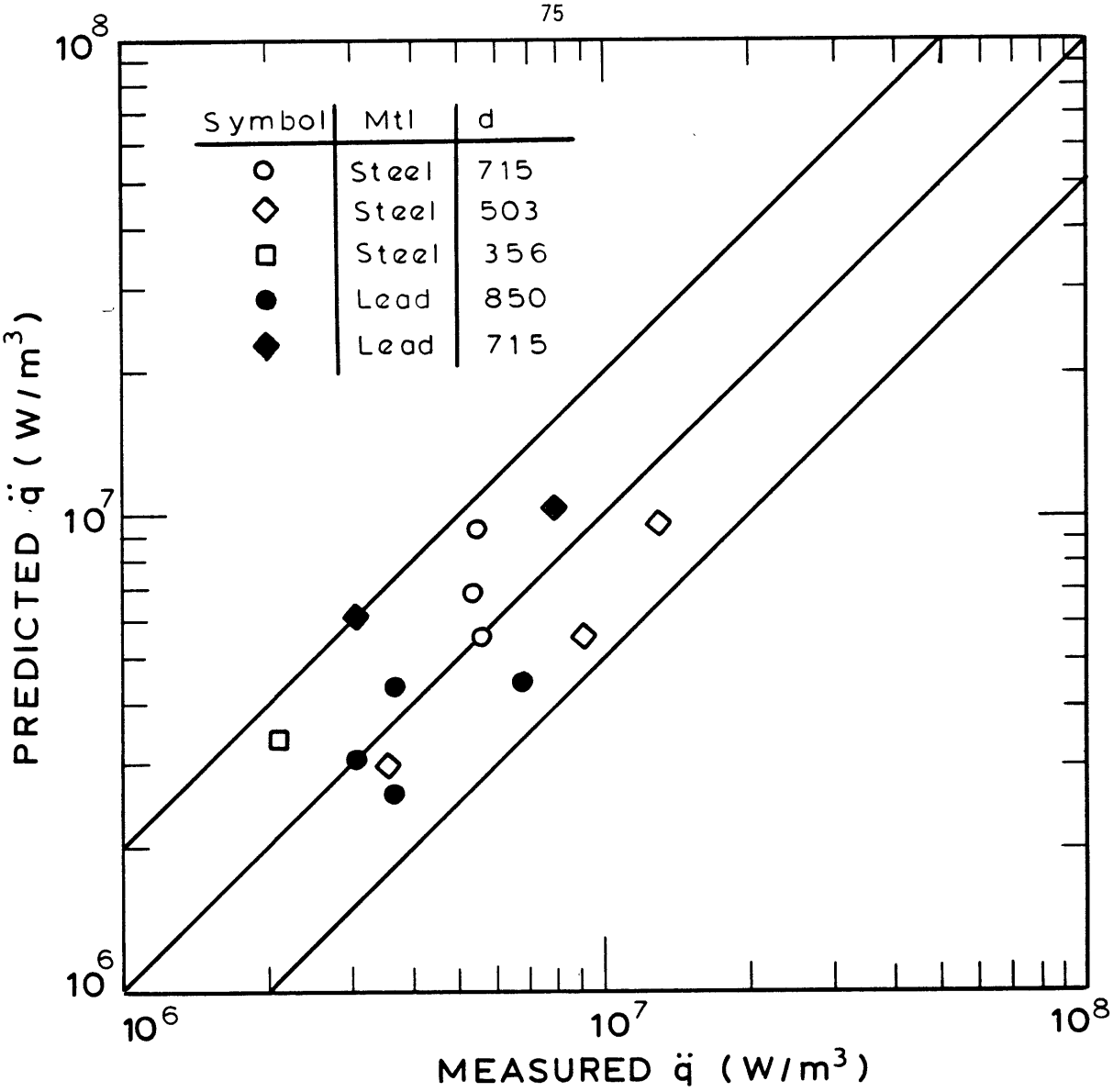

Fig 36 Dhir & Catton Data (Methanol) Unchanneled
Model $k_\ell = S^{3.486}$, $k_v = (1-S_e)^2(1-S_e^{1.486})$,
$K_\ell = S_e^{5.243}$, $K_v = (1-S_e)^3(1-S_e^{1.1215})^2$

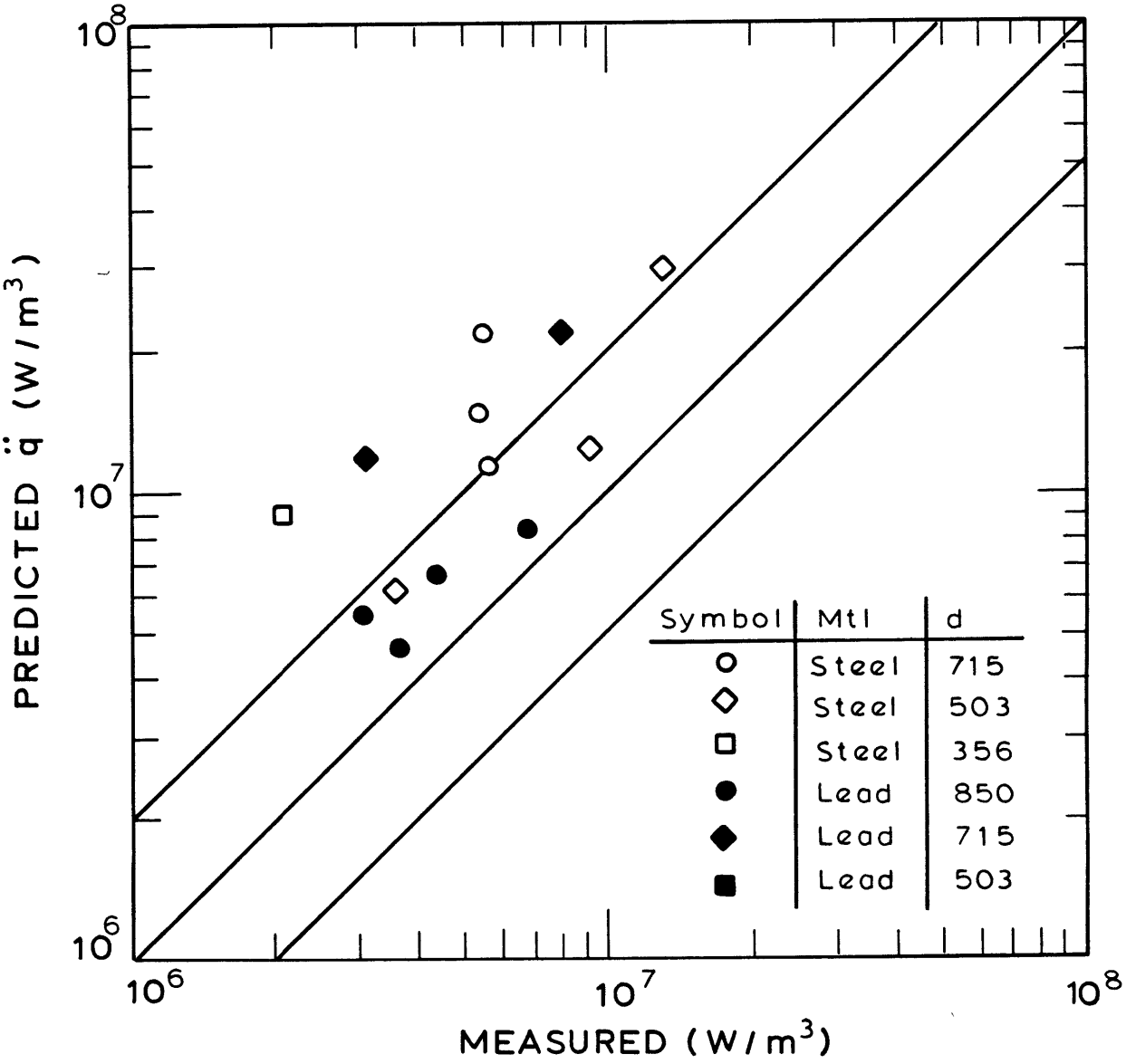

Fig 37 Dhir & Catton Data (Methanol) Channeled Model $k_\ell = S^3$, $k_v = 1-1.11S$, $K_\ell = S^3$, $K_v = (1-S)^3$

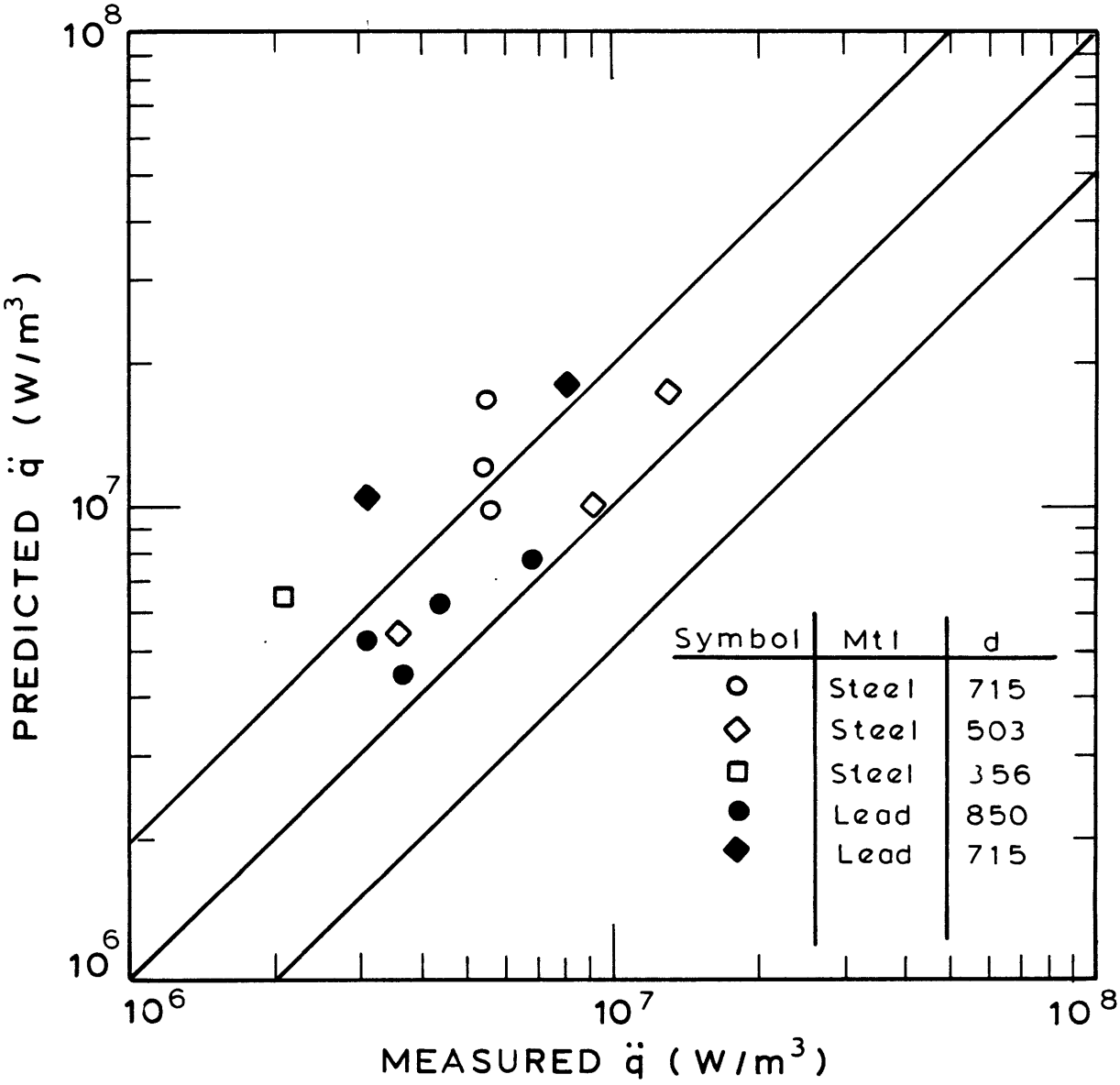

Fig 38 Dhir & Catton Data (Methanol) Unchanneled
Model $k_\ell = S^3$, $k_v = 1-1.11S$, $K_\ell = S^3$, $K_v = (1-S)^3$

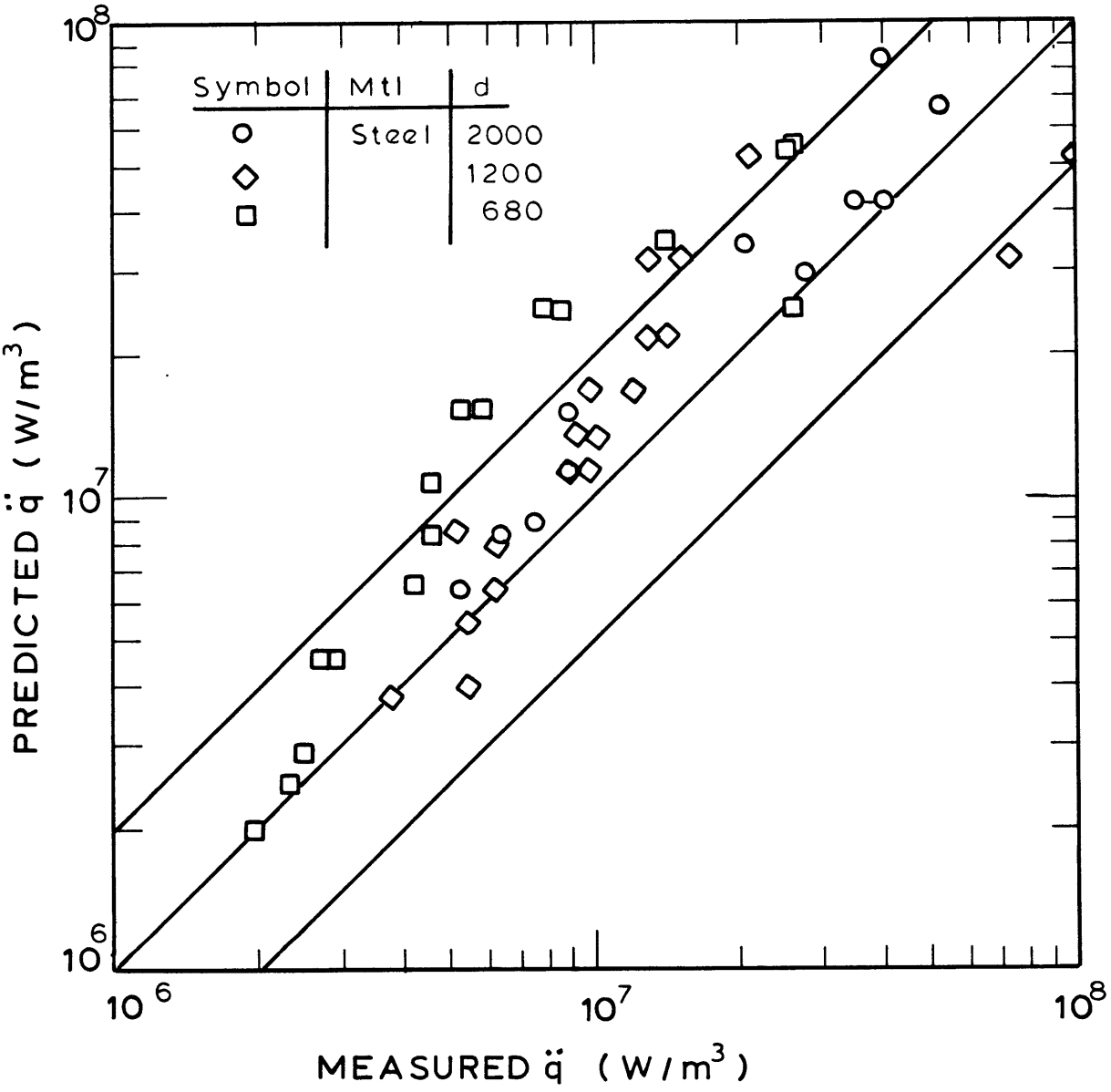

Fig 39 Trenberth Data, Channeled Model, $k_\ell = S_e^{3.486}$
$k_v = (1 - S_e)(1 - S_e^{1.486})$, $K_\ell = S_e^{5.243}$,
$K_v = (1 - S_e)^3 (1 - S_e^{1.1215})^2$

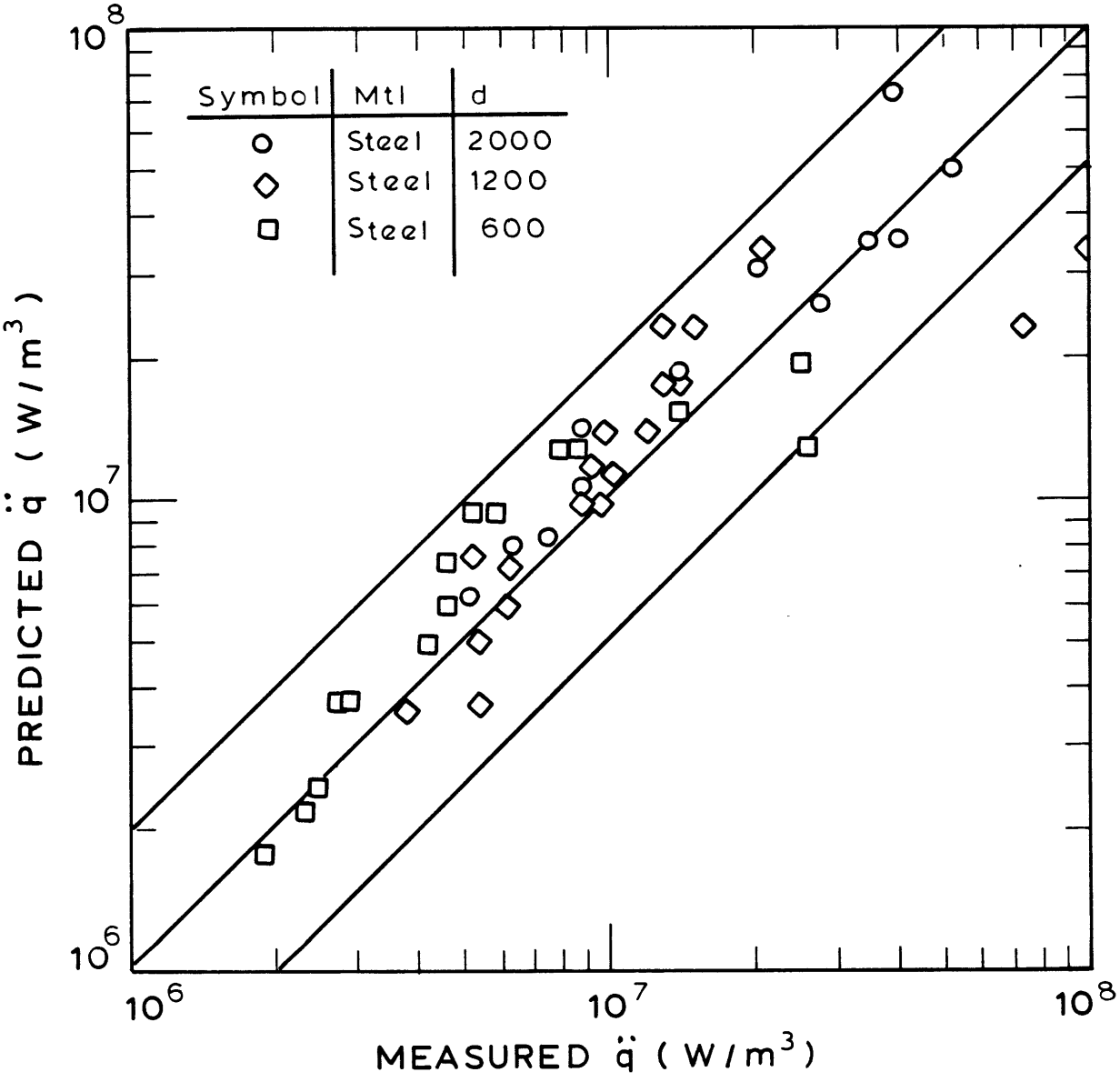

Fig 40 Trenberth Data Unchanneled Model, $k_\ell = S_e^{3.486}$,
$k_v = (1-S)^2(1-S_e^{1.486})$, $K_\ell = S_e^{5.243}$,
$K_v = (1-S)^3(1-S_e^{1.1215})^2$

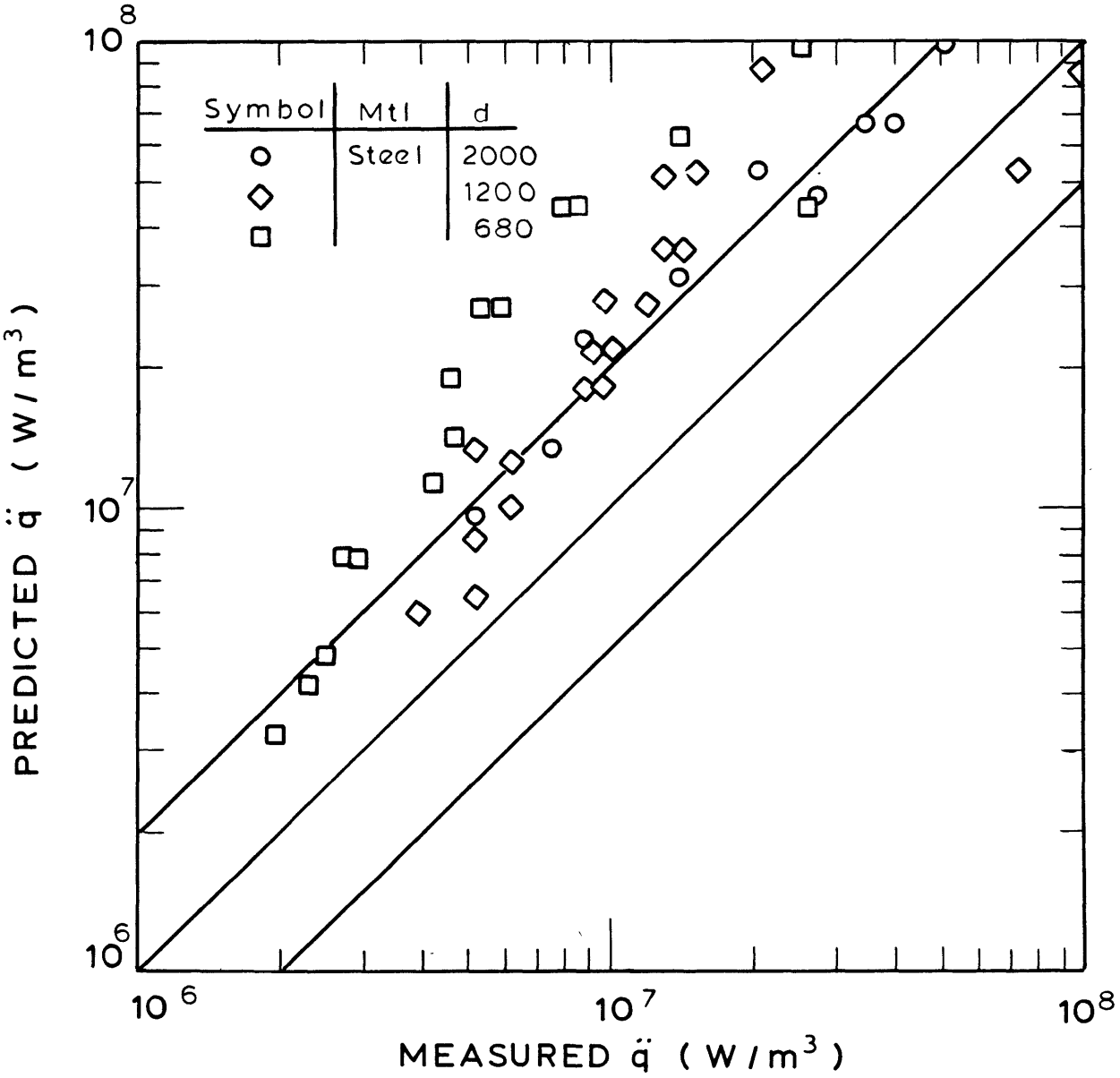

Fig 41 Trenberth Data, Channeled Model , $k_\ell = S^3$, $k_V = 1 - 1.11S$, $K_\ell = S^3$, $K_V = (1-S)^3$

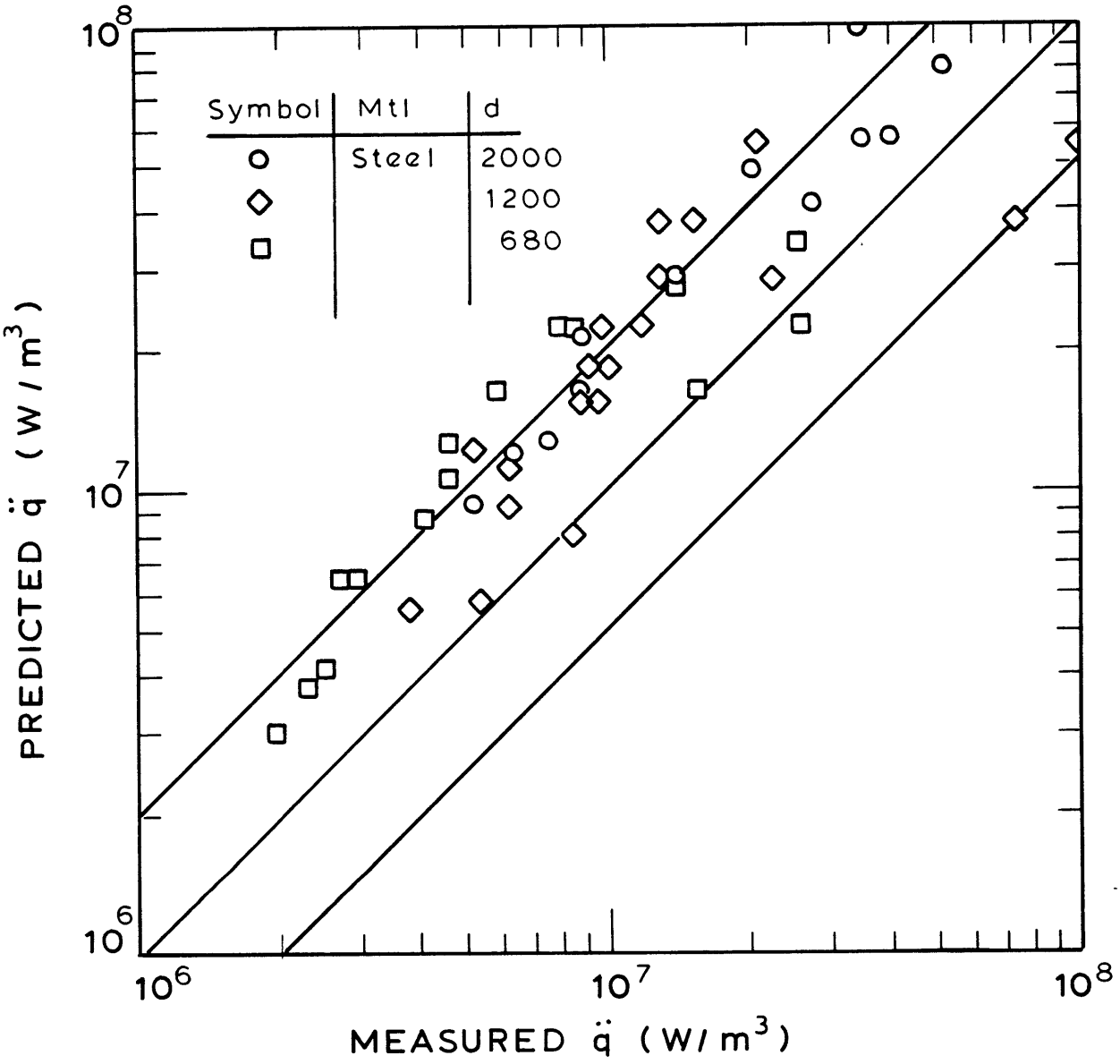

Fig 42 Trenberth Data, Unchanneled Model, $k_\ell = S^3$, $k_V = 1 - 1.11S$, $K_\ell = S^3$, $K_V = (1-S)^3$

unchanneled model with Scheidegger/Lipinski relative permeabilities (Figs. 30, 34) yield data fits of equal quality. Trenberth and Steven's data are fit best by the unchanneled model using Brooks and Corey's correlations (Fig. 40).

The scatter in the predicted vs measured graphs is large. Part of this is due to the uncertainity in the correlations within the model. The predicted dryout flux is sensitive to the channel depth, which is sensitive to the contact angle. The contact angle for iron-water-vapor combinations varies from 0 to 90 degrees.

The model is also sensitive to the relative permeabilities. The data gathered by Brooks and Corey strongly supports the Burdine equations. However, Leverett's capillary pressure-saturation curve contains a large amount of scatter. The data should probably have been plotted against residual saturation. Also, the nondimensionalization of the capillary pressure should be re-examined. An improved capillary pressure curve would improve the accuracy of the relative permeabilities.

A good deal of scatter exists within the data itself. Some of this could be due to the nebulous definition of dryout. At low, but non-zero saturations, the bed is largely dry, but still has tendrills of liquid winding their way to the bottom. Since the local porosity at the wall is higher than in the bed, low saturation regions may appear to be dry from the outside.

The use of thermocouples to detect global dryout is questionable in some cases. Regions that are unsaturated must have temperatures above the saturation temperature so that the energy generated therein can be conducted to the saturated zones. Consider the case of the 5 cm deep bed described in Figure 21. At a decay heat level of 10^4 kW/m^3, the saturation is as low as 34%. Now assume that the liquid zone is 5 particle diameters wide. This would cause the vapor zone to be about 5 mm wide. (Fig. 43).

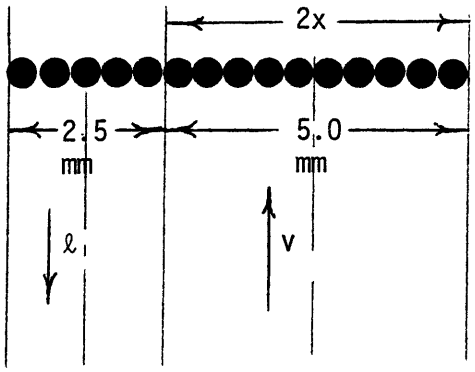

$\overline{K}_{iron}$ = 52 W/m-K

$\overline{K}_{steam}$ = .025 W/m-K

Fig. 43. Microscopic View of Dry Patch in a Partially Saturated Zone

For this bed, the composite thermal conductivity in the unsaturated region is about 0.25 W/mK.[32] The temperature difference between the centerline of the unsaturated zone and the liquid is then about

$$\Delta T = \frac{[\ddot{q}\ (1 - \varepsilon)] \times [\frac{x}{2}]}{\overline{K}_{bed}}$$

$$\simeq 75K \quad .$$

Larger unsaturated zones will have larger temperature differences. In the extreme case, it might be possible to have melted pockets of solid material before global dryout is achieved. The importance of this superheat is uncertain, and can be determined only by more quantitative knowledge of the characteristic dimensions in the unsaturated zone.

V. CONCLUDING REMARKS

Summary

An analytical model of two phase flow in unconsolidated porous beds is formulated. The model is one-dimensional and divides the porous bed into two regions. In the unchanneled region, the flow is described by the porous two phase flow equations. The relative permeabilities are important parameters in this part of the bed. If the capillary pressure-saturation curve is known accurately, these relative permeabilities can be calculated.

In the channeled region, vapor escapes through channels which are devoid of particles. The liquid flow is described by the single phase porous flow equations. The depth of the channeled region and the vapor pressure in the channels is predicted from the statics of particulate beds. Experimental data confirms the validity of the channel depth analysis.

Predictions of the analysis are compared to existing experimental data. The uncertainty of certain values within the analysis are noted. Difficulties in the experimental determination of dryout are described.

Conclusions

1. For purposes of analysis, a debris bed can be divided into a channeled region and an unchanneled region. The two-phase porous flow equations are valid in the unchanneled region. The single phase porous flow equation describes the liquid in the channeled region.

2. The channel depth is predicted by the relationship

$$h = \frac{4.6\ \sigma \cos\theta}{(\rho_s - \rho_\ell) g\ \bar{d}\ \varepsilon}$$

when the channels are stable. Because of the high surface tension of sodium, it is not known if the channels in a sodium uranium fuel bed will be stable.

3. The solid matrix in the channeled region cannot support shear forces. This causes the region to resemble a fluid. However, the particles are not fluidized in the sense of drag forces overcoming body forces.

4. Secondary flows in the liquid entrain particles off the top of the bed. If the particles are sufficiently small and the secondary flows sufficiently large, it is possible to entrain the entire bed. This has been observed only in glass-freon beds.

5. The predicted dryout flux is dependent on the relative permeability model. If the Burdine equations are used, a better knowledge of the capillary pressure-saturation curve is needed.

6. The unsaturated portions of a partially saturated bed have temperatures higher than the saturation temperature. Localized melting could occur if these unsaturated regions are sufficiently large.

7. The existence of an unsaturated region near a wall does not guarantee that global dryout has taken place.

Recommendations

The major uncertainty in the analysis is in the values of the relative permeabilities. The validity of the Burdine equations should be determined. Turbulent relative permeabilities should be measured.

A more exact definition of dryout is necessary. If the total cessation of downward liquid flow is important, then the saturation at the bottom of an experiment should be measured. If local dryout is found to be important, then the physical dimensions of the unsaturation zone in a partially saturated media must be determined.

REFERENCES

1. Kazimi, M.S., Chen, J., "A Condensed Review of the Technology of Post-Accident Heat Removal for the Liquid-Metal Fast Breeder Reactor," Nuclear Technology, vol. 38, pp. 339-366, (May 1978).

2. Fistedis, S.H., "Response of Breeder Reactor Components and Systems to Abnormal Events," Nuclear Engineering and Design, vol. 49, pp. 3-15, (1978).

3. Sowa, E.S., et.al., "Studies of the Formation and Cooling of Particulate Fuel Debris in Sodium," Proc. Int. Mgt. Fast Reactor Safety and Related Physics, CONF-761001, p 2036, U.S. Energy Research and Development Administration (1976).

4. Gabor, J.D. et. al., "Studies and Experiments on Heat Removal from Fuel Debris in Sodium," Proc. Fast Reactor Safety Conf., CONF-740401, p 823, U.S. Atomic Energy Commission (1974).

5. Rivard, J.B., "In-Reactor Experiments on the Cooling of Fast Reactor Debris," Nuclear Technology, vol. 46, pp. 344-349 (1979).

6. Brown, G.G., and Associates, Unit Operations, Wiley, New York, pp. 210-228, 1950.

7. Perry, J.H., Chilton, C.H., and Kirkpatrick, S.D., Chemical Engineer's Handbook, 4th ed., McGraw-Hill Book Co., pp. 18-26 and 18-30, 1963.

8. Keowen, R.S., "Dryout of a Fluidized Particle Bed with Internal Heat Generation," M.S. Thesis, University of California, Los Angeles, 1974.

9. Dhir, ViJay, and Catton, I., "Dryout Heat Fluxes for Inductively Heated Particulate Beds", ASME Winter Annual Meeting, Houston, 1975.

10. Lee, D.O., and Nilson, R.H., "Flow Visualization in Heat-Generating Porous Media," SAND76-0614, Sandia Laboratories, Albuquerque, N.M., 1976.

11. Hardee, H.C., and Nilson, R.H., "Natural Convection in Porous Media with Heat Generation," Nuclear Science and Engineering, 63, pp. 119-132, 1977.

12. Shires, G.L., and Stevens, G.F., "Dryout During Boiling in Heated Particulate Beds," AEEW-M1779, 1979.

13. Trenberth, R. and Stevens, G.F., "An Experimental Study of Boiling Heat Transfer and Dryout in Heated Particulate Beds,: AEEW-R1342, 1980.

14. Lipinski, R.J., "A Laminar-Turbulent Gravitational Capillary Particle Bed Dryout Model," SAND80-1452A, Sandia Laboratories, Albuquerque, 1980.

15. Lipinski, R.J., "A Model for Downward Boiling in Particle Beds," SAND80-1513A, Sandia Laboratories, Albuquerque, N.M., 1980

16. Lipinski, R.J., "A One-Dimensional Particle Bed Fryout Model," A.N.S. Transactions, vol. 38, pp. 386-387 (1981).

17. Rivard, J.B., "First In-Reactor Experiment with Simulated LMFBR Debris Bed," A.N.S. Transactions, vol. 27, pp. 653-654, 1977.

18. Rivard, J.B., "Debris Bed Studies and Experiments at Sandia Laboratories,"NUREG/CR-0263, 1978.

19. Sandia Laboratories, "Advanced Reactor Research Quaterly Report, April-June 1979,"NUREG/CR-0984, 1979.

20. Scharz, M., Gronager, J.E., and Lipinski, R.J., "Particle Bed Heat Removal with Subcooled Sodium: D4 Analysis," SAND80-1640A, 1980.

21. Scheidegger, A.E., The Physics of Flow in Porous Media, 3rd ed., University of Toronto Press, 1974.

22. Bear, Jacob, Dynamics of Fluids in Porous Media, American Elsevier Publishing Company, Inc., New York, 1972.

23. Ergun, Sabri, "Fluid Flow Through Packed Columns," Chemical Engineering Progress, 48, no. 2, February, 1952, pp. 89-94.

24. Leverett, M.C., "Capillary Behavior in Porous Solids," Transactions of AIME 142, pp. 152-169, 1941.

25. Rose, W. and Bruce, W.A., "Evaluation of Capillary Character in Petroleum Reservoir Rock," Petroleum Transactions, AIME, T.P. 2594, pp. 127-142 (May, 1949).

26. Brooks, R.H., and Corey, A.T., "Hydraulic Properties of Porous Media," Hydrology Papers, Colorado State University, No. 3., March, 1964.

27. Brooks, R.H., and Corey, A.T., "Properties of Porous Media Affecting Fluid Flow," Journal of the Irrigation and Drainage Division, Proceedings of the ASCE, IR2, June, 1966, pp. 61- 88.

28. Versluys, J., "Can Absence of Edge-Water Encroachment in Certain Oil Fields be Ascribed to Capillarity?", Bull. Amer. Assoc. Petrol. Geol. 15, pp. 189-200 (1931).

29. Chatenever, Alfred, "Visual Examinations of Fluid Behavior in Porous Media - Part I," Petroleum Transactions, AIME, vol. 195, pp. 149-156 (1952).

30. Lambe, T.W., and Whitman, R.V., An Introduction to Soil Mechanics, John Wiley & Sons, Inc., New York (1966).

31. Dhir, V.K., et. al., "Study of Dryout Heat Fluxes in Beds of Inductively Heated Particles," NUREG-0262 (June, 1977).

32. McAdams, W.H., Heat Transmission, McGraw-Hill Book Company, New York, 3rd edition (1954).

33. Burdine, N.T., "Relative Permeability Calculations for Pore Size Distribution Data," Petroleum Transactions, AIME, vol. 198, pp. 71-78 (1953).

APPENDIX I. Calculation of Relative Permeability

The correlation for laminar relative permeability favored by Brooks and Corey[26] is the Burdine equation.[33] From a parallel tube analogy, Burdine derived the identities

$$k_{wetting} = S_e^2 \int_0^{S_e} \frac{dS_e}{P_c^2} \Big/ \int_0^1 \frac{dS_e}{P_c^2} \qquad \text{A1.1}$$

$$k_{non\text{-}wetting} = (1 - S_e)^2 \int_{S_e}^1 \frac{dS_e}{P_c^2} \Big/ \int_0^1 \frac{dS_e}{P_c^2} \qquad \text{A1.2}$$

where S_e is the effective saturation, defined as

$$S_e = \frac{S - S_r}{1 - S_r} \qquad \text{A1.3}$$

In the manner of Brooks and Corey[26,27] the dimensionless capillary pressure can be fitted to the form

$$P = a\, S_e^{-b} \qquad \text{A1.4}$$

where

$$P = \frac{P_c}{\sigma \cos\theta} \left(\frac{k}{\epsilon}\right)^{1/2} \qquad 2.5$$

For the drainage curve

$a = 0.3771$

$b = 0.2430$

$S_r = 0.03$

For the imbibition curve

$a = 0.2353$

$b = 0.4230$

$S_r = 0.02$

Carrying out the integration,

$$k_w = k_\ell = S_e^{2b+3}$$

$$k_{nw} = k_v = (1 - S_e)^2 (1 - S_e^{2b+1}) \qquad \text{A1.5}$$

Lipinski[14] has used a relationship cited in Scheidegger.[21]

$$k_\ell = S^3$$

$$k_v = 1 - 1.11\ S \qquad \text{A1.6}$$

This relationship is based on oil-water data, and would seem to be less applicable than the Burdine equation which was backed with gas-liquid data. The relative permeabilities are shown in Figure 43.

An upper bound on the turbulent permeability can be derived by considering flow areas only, and ignoring tortuosity. Doing this, the bed can be viewed as having separate flows (Fig. 44).

The single phase flow equations apply to each region

$$\frac{dP_i}{dz} = \frac{\rho_i}{\kappa} |q_i^*| q_i^* = \frac{\rho_i}{\kappa \kappa_i} |q_i| q_i \quad , \ i=\ell, \ v \qquad \text{A1.7}$$

$$\therefore \quad \kappa_i = \left(\frac{q_i}{q_i^*}\right)^2 = \left(\frac{A_i}{A}\right)^2$$

$$\kappa_\ell = S^2$$

$$\kappa_v = (1 - S)^2 \qquad \text{A1.8}$$

A second model, proposed by Lipinski[14] is

$$\kappa_\ell = S^3$$

$$\kappa_v = (1 - S)^3 \qquad \text{A1.9}$$

The model is unexplained.

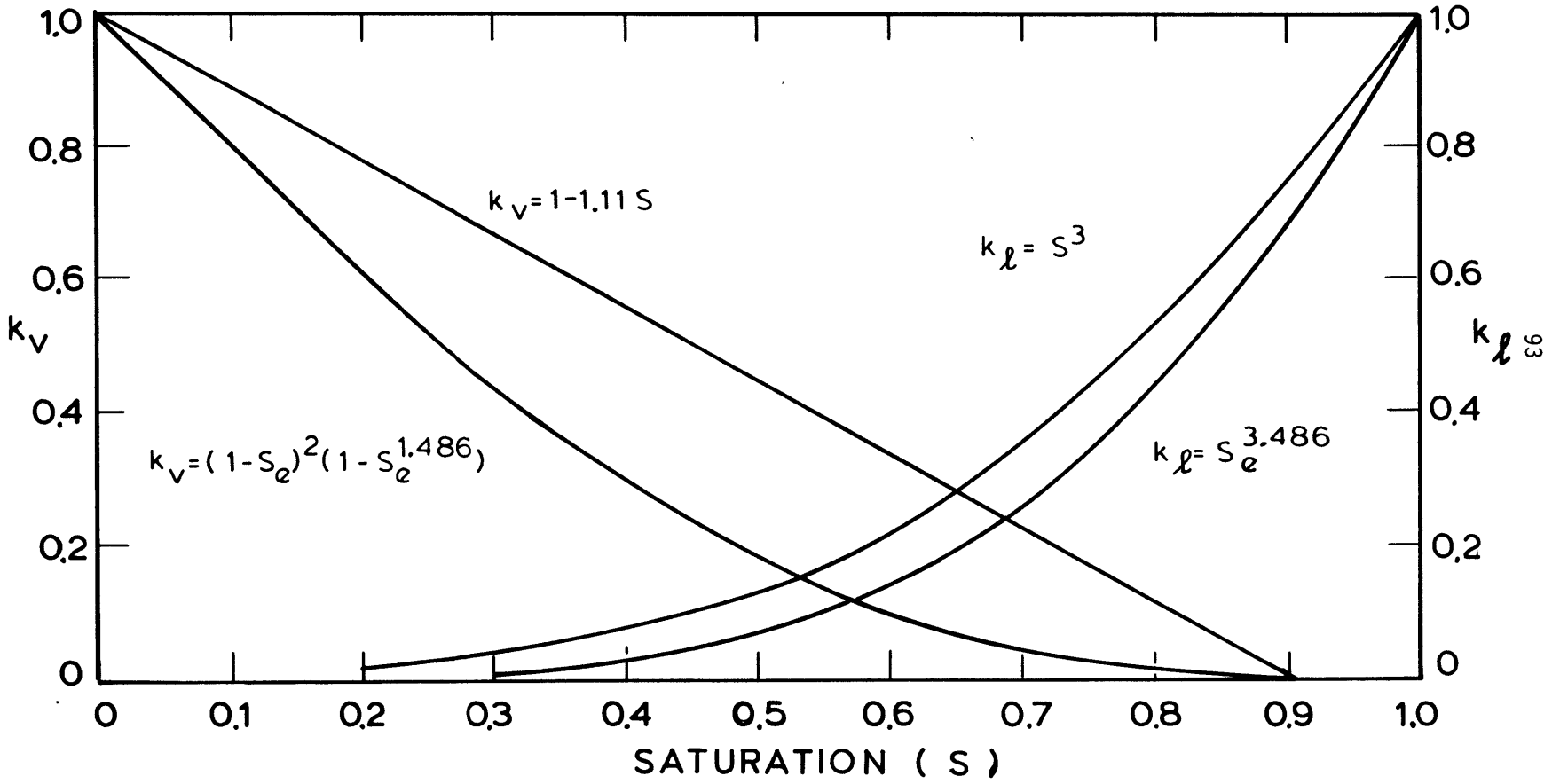

Fig 44 Laminar Relative Permeability vs Saturation

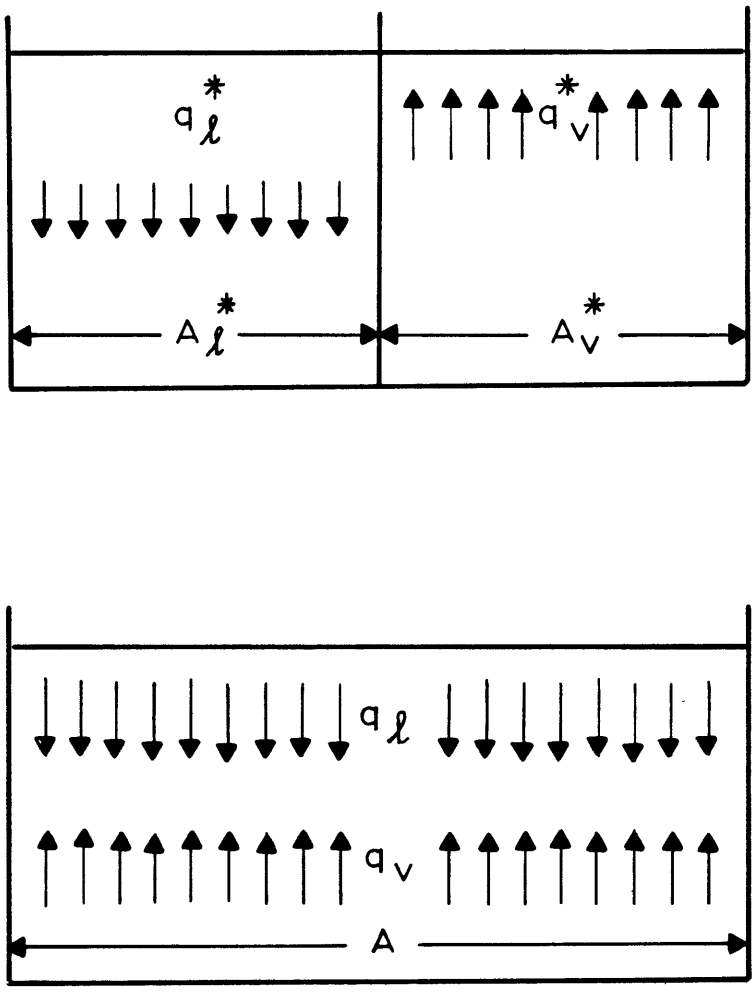

Fig 45 Turbulent Relative Permeability Derivation

A third model can be derived using the same approach as Burdine. Although the form of the turbulent term in the Ergun equation was derived using flow over a sphere, the same form can be obtained assuming flow through a tube bundle in which the friction factor is constant.

For a single tube

$$\frac{dP}{dx} = \frac{f}{D} \frac{V_x^2}{2} \rho \qquad \text{A1.10}$$

where x is the microscopic flow direction. Converting to the net flow direction (z)

$$\frac{1}{\tau_{1.0}} \frac{dP}{dz} = \frac{f}{D} \frac{\rho}{2} (\tau_{1.0} V_z)^2 \qquad \text{A1.11}$$

where

$$\tau_{1.0} = \frac{dz}{dx} = \frac{\ell_z}{\ell_{actual}} \qquad \text{A1.12}$$

This is the definition of tortuosity that Burdine uses and not the more commonly recognized form.

Rewriting

$$V_z(R) = \left[\frac{1}{\tau_{1.0}^3} \frac{4}{f\rho} \frac{dP}{dz}\right]^{1/2} \sqrt{R} \qquad \text{A1.13}$$

The velocity must be averaged over the tube bundle. For a saturation of unity and a tube radius distribution of $\overline{P}(R)$

$$V_z(S = 1.0) = \frac{\int_{R_{min}}^{R_{max}} V_z(R)\, \Pi R_H^2\, \overline{P}(R)\, dR}{\int_{R_{min}}^{R_{max}} \Pi R^2\, \overline{P}(R)\, dR} \qquad \text{A1.14}$$

Converting to a saturation integral:

$$S = \frac{\int_{R_{min}}^{R} \Pi R^2\, \overline{P}(R)\, dR}{\int_{R_{min}}^{R_{max}} \Pi R^2\, \overline{P}(R)\, dR} \qquad \text{A1.15}$$

$$dS = \frac{R^2\, \overline{P}(R)\, dR}{\int_{R_{min}}^{R_{max}} R^2\, \overline{P}(R)\, dR} \qquad \text{A1.16}$$

Substituting into A1.13

$$\overline{V}_z(S = 1.0) = \int_0^1 V_z(R)\, dS \qquad \text{A1.17}$$

$$= \left[\frac{1}{\tau_{1.0}} \frac{4}{3} \frac{1}{f\rho} \frac{dP}{dz}\right]^{1/2} \int_0^1 \sqrt{R}\, dS \qquad \text{A1.18}$$

For a tube

$$R = \frac{2\,\sigma\,\cos\theta}{P_c} \qquad \text{A1.19}$$

Substituting into A1.18

$$\overline{V}_z(S = 1.0) = \left[\frac{1}{\tau_{1.0}^3}\ \frac{8}{f\rho}\ \frac{dP}{dz}\ \sigma\cos\theta\right]^{1/2} \int_o^1 \frac{dS}{P_c^{1/2}} \qquad \text{A1.20}$$

and

$$\frac{dP}{dz} = \frac{\rho}{\kappa}\ q^2 \qquad \text{A1.21}$$

where

$$\kappa = \frac{8\,\varepsilon^2}{\tau_{1.0}^3\ f}\ \sigma\cos\theta\ \left[\int_o^1 \frac{dS}{P_c^{1/2}}\right]^2 \qquad \text{A1.22}$$

Similarly for a partially saturated media

$$\overline{V}_{z_\ell}(S) = \frac{q_\ell}{S\varepsilon} = \left[\frac{1}{\tau_\ell^3(S)}\ \frac{8}{f\rho_\ell}\ \frac{dP_\ell}{dz}\ \sigma\cos\theta\right]^{1/2} \frac{1}{S}\int_o^S \frac{dS}{P_c^{1/2}} \qquad \text{A1.23}$$

and

$$\overline{V}_{z_v}(S) = \frac{q_v}{(1 - S)\varepsilon} = \left[\frac{1}{\tau_v^3(S)}\ \frac{8}{f\rho_v}\ \frac{dP_v}{dz}\ \sigma\cos\theta\right]^{1/2} \left[\frac{1}{(1-S)}\int_S^1 \frac{dS}{P_c^{1/2}}\right]^2$$

Also

$$\frac{dP_i}{dz} = \frac{\rho_i}{\kappa\kappa_i} q_i^2 \quad , \quad i = \ell, v \qquad \text{A1.24}$$

where

$$\kappa\kappa_\ell = \frac{8\,\varepsilon^2}{\tau_\ell^3(S)f}\,\sigma\cos\theta\,\left[\int_o^S \frac{dS}{P_c^{1/2}}\right]^2 \qquad \text{A1.25}$$

and

$$\kappa\kappa_v = \frac{8\,\varepsilon^2}{\tau_v^3(S)f}\,\sigma\cos\theta\,\left[\int_S^1 \frac{dS}{P_c^{1/2}}\right]^2$$

Comparing A1.25 to A1.22

$$\kappa_\ell = \frac{\left(\frac{\tau_{1.0}}{\tau_\ell(S)}\right)^3\left[\int_o^S \frac{dS}{P_c^{1/2}}\right]^2}{\left[\int_o^1 \frac{dS}{P_c^{1/2}}\right]^2} \qquad \text{A1.26}$$

and

$$\kappa_v = \frac{\left(\frac{\tau_{1.0}}{\tau_v(S)}\right)^3\left[\int_S^1 \frac{dS}{P_c^{1/2}}\right]^2}{\left[\int_o^1 \frac{dS}{P_c^{1/2}}\right]^2}$$

According to Burdine's experiments

$$\frac{\tau_{1.0}}{\tau_\ell(S)} = S_e \qquad \text{A1.27}$$

an

$$\frac{\tau_{1.0}}{\tau_v(S)} = 1 - S_e$$

Substituting these into A1.26

$$\kappa_\ell = \frac{S_e^3 \left[\int_0^{S_e} \frac{dS_e}{P_c^{1/2}} \right]^2}{\left[\int_0^1 \frac{dS_e}{P_c^{1/2}} \right]^2} \qquad \text{A1.28}$$

and

$$\kappa_v = \frac{(1 - S_e)^3 \left[\int_S^1 \frac{dS}{P_c^{1/2}} \right]^2}{\left[\int_0^1 \frac{dS}{P_c^{1/2}} \right]^2}$$

If $P = a\, S_e^{-b}$ A1.4

then $\kappa_\ell = S_e^{5+b}$ A1.29

and

$$\kappa_v = (1 - S_e)^3 \left(1 - S_e^{1+b/2}\right)^2$$

The derivation used here is not rigorous. The tortuosity ratios, which are functions of saturation, are excluded from the averaging process. This is, however, consistent with Burdine's analysis, and may be consistent with his measurement. Additionally, the averaging took place while considering only the turbulent term. This implies an additive behavior for laminar and turbulent terms in the modified Ergun equation which is probably wrong.

APPENDIX II. Criterion for Dryout

The term "dryout" has typically been construed to mean a condition of zero saturation at the bottom of a debris bed. While this is fundamentally correct, the topic deserves some elaboration.

The residual saturation is that saturation at which the wetting fluid can no longer flow. The small pockets of wetting fluid are not in contact with one another, so no flow path exists (Fig. 45).

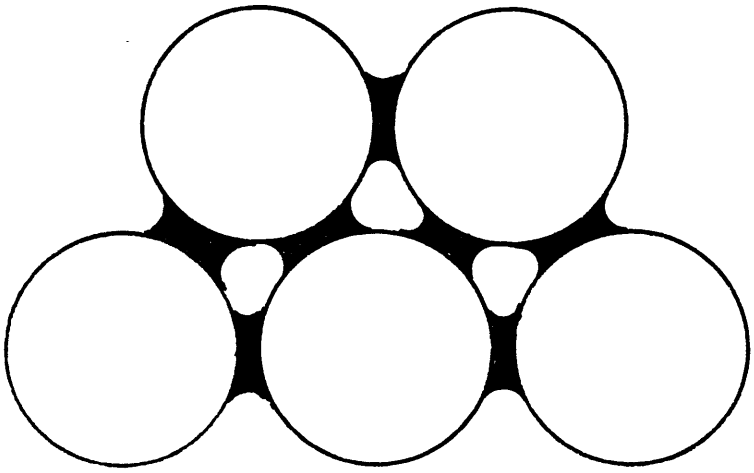

Fig. 46. Schematic of Residual Saturation

The residual saturation can be significant. According to the correlation supplied in Brown and Associates[6], a debris bed composed of 300 micron particles and having a porosity of 40% has a residual saturation of about 20% when water is the wetting fluid. For such a bed, dryout occurs when the bottom of the bed reaches the residual saturation. At this point, liquid flow to the particles at the bottom of the bed ceases, and the residual liquid is evaporated shortly thereafter.

A somewhat more mathematical problem occurs when the residual saturation is used as the boundary condition at the bottom of a debris bed. The liquid absolute pressure at the bottom of the bed approaches negative infinity. The dilemma is artificial. Logically, the capillary pressure must have an upper limit, although its value is unknown. If this correction were not enough to prevent the prediction of negative pressures, then a model which describes the change in the boiling temperature as a function of liquid pressure would be needed.

The problem of negative liquid pressure can be circumvented if a lower bound is established. Dryout is then redefined to occur when the minimum allowed liquid pressure is reached somewhere in the bed. The two obvious bounds for the minimum absolute pressure are the liquid pressure at the top of the bed and zero. When the liquid pool is assumed to exist at atmospheric pressure, the differences in predicted dryout heat fluxes that these two bounds produce are minuscule. This might not be the case if the liquid pool is highly pressurized.

The liquid pressure at any point in the bed can be calculated by integrating equation 2.3 from the top of the bed.

$$\frac{dP_\ell}{dz} = -\left(\rho_\ell g + \frac{\mu_\ell}{kk_\ell} q_\ell + \frac{\rho_\ell}{\kappa k_\ell} |q_\ell| q_\ell\right) \qquad 2.3$$

Substituting the energy relation (eq. 2.15)

$$\frac{dP_\ell}{dz} = -\rho_\ell g + \frac{\mu_\ell}{kk_\ell} \int_0^z \frac{\ddot{q}\,(1-\varepsilon)}{\rho_\ell\, h_{fg}} + \frac{\rho_\ell}{\kappa k_\ell} \left(\int_0^z \frac{\ddot{q}\,(1-\varepsilon)}{\rho_\ell\, h_{fg}} dz \right)^2 \qquad A2.1$$

Integrating and rearranging

$$P_\ell(z) = P_\ell(z=L) + \rho_\ell g\,(L-z) + \int_L^z \left[\frac{\nu_\ell}{kk_\ell} \frac{\ddot{q}}{h_{fg}} \int_0^z (1-\varepsilon)dz + \frac{1}{\rho_\ell\, \kappa k_\ell} \left[\frac{\ddot{q}}{h_{fg}} \int_0^z (1-\varepsilon)dz \right]^2 \right] dz \qquad A2.2$$

```
C
C     APPENDIX III.  PROGRAM
C
C
      DIMENSION SM(1001),S(2000),ETA2(2000).PIPL(3000)
C
C     LIQUID MATERIAL PROPERTIES
C
      ROEG=0.596
      ROEL=961.54
      G=9.8
      SIG=5.88E-2
      GNUL=3.00E-7
      GNUG=2.17E-5
      RATIO=GNUG/GNUL
      ROERATI=ROEL/ROEG
      HFG=2.26E6
C
C     BED PROPERTIES
C
      WRITE(6,1)
    1 FORMAT(1X,'THE MEAN PARTICLE DIAMETER IS (IN MICRONS):  ')
      READ(5,2) D
    2 FORMAT(v)
      D=D*10.**(-6)
      WRITE(6,3)
    3 FORMAT(1X,'THE PARTICLE SPHERICITY IS: ')
      READ(5,2) SPH
      WRITE(6,4)
    4 FORMAT(1X,'THE SOLID DENSITY IS (IN SI UNITS): ')
      READ(5,2) ROES
      WRITE(6,5)
    5 FORMAT(1X,'THE BED POROSITY IS :  ')
      READ(0,2) EPS
      WRITE(6,6)
    6 FORMAT(1X,'THE BED DEPTH IS (IN METRES):  ')
      READ(5,2) XL
C      WRITE(6,7)
C    7 FORMAT(1X,'THE BED TOP LIQUID PRESSURE IS (PSI) ')
C      READ(5,2) PLL
      PLL=14.7
C      WRITE(6,8)
C    8 FORMAT(1X,'THE MINIMUM LIQUID PRESSURE IS (PSI): ')
C      READ(5,2) PLMIN
      PLMIN=0.
      WRITE(6,30)
   30 FORMAT(1X,'THE CONTACT ANGLE IS (DEG): ')
      READ(5,2) DEG
      COSDEG=COS(DEG*2.*3.1415927/360.)
      WRITE(6,99)
   99 FORMAT(1X,'AN INITIAL GUESS FOR Q IS(W/M*3) :  ')
      READ(5,2) QGUESS
      WRITE(6,9)
    9 FORMAT(1X,'END OF DATA')
C
C     Porosity
C
C     EPS=1.-XLOAD*10./ROES/XL
      A=0.3771
      SR=0.
```

```
      B=0.2430
      XK=D**2*EPS**3/150./(1.-EPS)**2*SPH**2
      XKAPPA=D*SPH*EPS**3/(1.-EPS)/1.75
      BA=2*B+1
      BB=2.*B+3
      BC=B+1.
C
C     CONSTANTS
C
      COEF=GNUL/SIG/HFG*XL
      PIK=XK/XL**2
      PIKAPPA=XKAPPA*ROEL*GNUL**2/SIG/XL**2
      PIG=ROEL*G*XL**2/SIG
      PIGNU=GNUG/GNUL
      PIROVA=ROEG/ROEL
      ROEBED=(1.-EPS)*ROES+EPS*ROEL
      PIROBA=ROEBED/ROEL
      PIPLL=(PLL*6895.)*XL/SIG
      PIPMIN=(PLMIN*6895.)*XL/SIG
      WRITE(0,101)
  101 FORMAT(10X,'PIQ',10X,'PIQNEW',17X,'FCN',//)
C
C     CALCULATION OF PIQDRY
C
      PIQ=QGUESS*COEF
      DPIQ=PIQ
  400 ETAMAC=0.
      PIQMAX=10.**25
      PIQMIN=0.
      DO 10 I=1,20
      IFLAG=1
   15 CALL CHANNEL(PIQ,PIK,PIG,PIROBA,EPS,SM,A,B,NMAX,PIKAPPA,COSDEG,SR)
      CALL DEPTH(PIQ,PIK,PIG,PIROBA,PIROVA,PIGNU,EPS,A,B,
     1SM,SMAC,ETAMAC,NMAX,I,PIKAPPA,COSDEG,SR)
      CALL PRESSUR(PIPLL,PIPLO,PIG,PIQ,PIK,SM,SMAC,PIPL,NTOT,SR,
     1ETAMAC,A,B,PIROVA,PIGNU,EPS,ETA2,MMAX,IFLAG,S,PIKAPPA,COSDEG)
      IF(IFLAG.EQ.1) GO TO 16
      PIQMAX=AMIN1(PIQMAX,PIQ)
      WRITE(0,302) IFLAG
  302 FORMAT(1X,I10)
      DPIQ=DPIQ/2.
      PIQ=PIQ-DPIQ
      GO TO 15
   16 FCN=PIPMIN-PIPLO
      IF(FCN.LT.0.) PIQMIN=AMAX1(PIQMIN,PIQ)
      IF(FCN.GT.0.) PIQMAX=AMIN1(PIQMAX,PIQ)
      PIQ1=PIQ-0.90*ABS(DPIQ)
      CALL CHANNEL(PIQ1,PIK,PIG,PIROBA,EPS,SM.A,B,NMAX,PIKAPPA,COSDEG,SR
     1)
      CALL DEPTH(PIQ1,PIK,PIG,PIROBA,PIROVA,PIGNU,EPS,A,B,
     1SM,SMAC,ETAMAC,NMAX,I,PIKAPPA,COSDEG,SR)
      CALL PRESSUR(PIPLL,PIPLO,PIG,PIQ1,PIK,SM.SMAC,PIPL,NTOT,SR,
     1ETAMAC,A,B,PIROVA,PIGNU,EPS,ETA2,MMAX,IFLAG,S,PIKAPPA,COSDEG)
      FCN1=PIPMIN-PIPLO
      DERIV=(FCN1-FCN)/(PIQ1-PIQ)
      IF(ABS(DERIV).LE.5.*10.**5) PIQ=2.*PIQ
      DPIQ=PIQ/2.
      IF(ABS(DERIV).LE.5.*10.**5) GO TO 400
      DPIQ=-1.*FCN/DERIV
      PIQNEW=PIQ+DPIQ
```

```
      IF(PIQNEW.GT.PIQMAX) PIQNEW=(PIQMAX+PIQ)/2.
      IF(PIQNEW.LT.PIQMIN) PIQNEW=(PIQMIN+PIQ)/2.
      DPIQ=PIQNEW-PIQ
      WRITE(0,102) PIQ,PIQNEW,FCN,DERIV
  102 FORMAT(1X,F15.12,5X,F15.12,5X,F10.1,5X,F14.1)
      IF(ABS((PIQNEW-PIQ)/AMIN1(PIQNEW,PIQ)).LE.0.01
     2.OR.(PIQMAX-PIQMIN)/PIQMIN.LE.0.01
     1) GO TO 20
   10 PIQ=PIQNEW
      WRITE(0,205)
  205 FORMAT(1X,'THE ITERATION FOR PIQ DID NOT CONVERGE')
   20 PIQDRY=PIQNEW
      QDOT=PIQDRY/COEF
      SO=S(MMAX+1)
      WRITE(0,103) QDOT,SO,ETAMAC,SMAC
  103 FORMAT(//,1X,"QDOT= ",F12.1,"  W/M**3",/,
     13X,"SO= ",F7.5,/,1X,"ETAM= ",F5.3,/,1X,"SM= ",F5.3)
      NNMAX=NMAX+1
C      WRITE(0,500) (SM(I),I=1,NNMAX,10)
  500 FORMAT(1X,10(F5.3,1X))
      MMMAX=MMAX+1
      J=MMMAX-10
C      WRITE(0,700) (ETA2(I),S(I),I=1,MMMAX,25)
C      WRITE(0,700) (ETA2(I),S(I),I=J,MMMAX)
  700 FORMAT(10(F4.3,1X,F5.3,2X))
C
C     CONVERT PIPL TO PRESSURES IN PSI
C
      DO 600 I=1,NTOT
  600 PIPL(I)=PIPL(I)*SIG/XL/6895.
      N1=NTOT-(MMAX+1)
C      WRITE(0,601) (PIPL(I),I=1,N1,10)
C      WRITE(0,601) (PIPL(I+1),ETA2(I-N1+1),I=N1,NTOT,10)
C      WRITE(0,601) (PIPL(NTOT-10+I),ETA2(NTOT-10+I-N1),I=1,10)
  601 FORMAT(15(F7.4,1X))
      STOP
      END
C
C
C
      SUBROUTINE CHANNEL(PIQ,PIK,PIG,PIROBA,EPS,SM.A,B,NMAX,PIKAPPA,
     1COSDEG,SR)
      DIMENSION SM(1001)
C
C     FIND SM AS A FUNCTION OF ETAM USING THE
C     CHANNELED MOMENTUM EQUATION
C
      BB=2.*B+3
      BC=B+1
      ABNEG=-1.*A*B
      N=1000
      DETAM=-1./(1.*N)
      SM(1)=1.
      ETAM=1.
      UN1=PIQ/PIK*(1.-EPS)
      UN2=PIG*(PIROBA-1.)
      UN3=(PIK/EPS)**0.5
      UN4=(PIQ*(1.-EPS))**2/PIKAPPA
      DO 10 I=1,1000
      ETAM=1.+(I-0.5)*DETAM
```

```
      SEFF=(SM(I)-SR)/(1.-SR)
      XKL=SEFF**BB
      XKAPPAL=SEFF**(5+B)
      PS=ABNEG/SEFF**BC
      IF(SEFF.GE.0.999)  PS=-A/0.001
      SM(I+1)=SM(I)-(UN1*ETAM/XKL+UN2+UN4*ETAM**2/XKAPPAL)*UN3/PS*DETAM
     1/COSDEG
      IF(SM(I+1).LT.SR) GO TO 20
   10 CONTINUE
   20 NMAX=I
      RETURN
      END
C
C
C
      SUBROUTINE DEPTH(PIQ,PIK,PIG,PIROBA,PIROVA,PIGNU,EPS,A,B,
     1SM,SMACN,ETAMACN,NMAX,MARK,PIKAPPA,COSDEG,SR)
      DIMENSION SM(1001)
C
C     FIND THE ACTUAL SM AND ETAM
C
      DO 10 I=1,NMAX
      SMACN=SM(I+1)
      ETAMACN=1.-(I-0.)/1000.
      IF(SM(I).GE.0.999.AND.SM(I+1).LE.0.999) GO TO 20
   10 CONTINUE
      WRITE(0,30)
   30 FORMAT(1X,'SUBROUTINE DEPTH DOES NOT WORK')
   20 RETURN
      END
C
C
C
      SUBROUTINE PRESSUR(PIPLL,PIPLO,PIG,PIQ,PIK,SM.SMAC.PIPL,NTOT,SR,
     1ETAMAC,A,B,PIROVA,PIGNU,EPS,ETA2,MMAX,IFLAG,S,PIKAPPA,COSDEG)
      DIMENSION SM(1001),S(2000),ETA2(2000).PIPL(3000)
      N=1000
      BA=2*B+1
      BB=2*B+3
      BC=B+1
      BD=B/2.+1.
      ABNEG=-1.*A*B
C
C     INTEGRATION FOR CHANNELED REGION
C
      SUB1=PIK*PIQ/PIKAPPA*(1.-EPS)
      SUB2=PIQ*(1.-EPS)/PIK
      DETA=1./(1.*N)
      N1=(1-ETAMAC)*N+1
      NN=N1-1
      ETAM1=1.-(N1-1.)/(1.*N)
      ETA=(ETAM1+ETAMAC)/2.
      SMB=(SMAC+SM(N1))/2.
      SEFF=(SMB-SR)/(1.-SR)
      XKL=SEFF**BB
      XKAPPAL=SEFF**(5+B)
      SUM=0.
      PIPL(1)=PIPLL
      TOTAL1=(ETA/XKL+SUB1*ETA**2/XKAPPAL)*(ETAM1-ETAMAC)
      DO 10 I=1,NN
```

```
      ETA=1.-(I-0.5)*DETA
      SB=(SM(I)+SM(I+1))/2.
      SEFF=(SB-SR)/(1.-SR)
      XKL=SEFF**BB
      XKAPPAL=SEFF**(5+B)
      SUM=SUM+(ETA/XKL+SUB1*ETA**2/XKAPPAL)
   10 PIPL(I+1)=PIPLL+PIG*(1.-(ETA-DETA/2.))
     1-SUM*SUB2*DETA
      TOTAL=TOTAL1+SUM*DETA
      PIPL(N1+1)=PIPLL+PIG*(1.-ETAMAC)
     1-TOTAL*SUB2
C
C     SATURATIONS IN UNCHANNELED REGION
C
      N=1000
      S(1)=SMAC
      UN1=PIG*(1.-PIROVA)*PIK**0.5/EPS**0.5
      UN2=PIQ/PIK**0.5/EPS**0.5*(1.-EPS)
      UN3=(PIK/EPS)**0.5*(PIQ*(1.-EPS))**2/PIKAPPA
      DETA2MX=-1.*ETAMAC/(1.*N)
      DSMAX=0.005
      ETA2(1)=ETAMAC
      DO 20 I=1,2000
      SEFF=(S(I)-SR)/(1.-SR)
      PS=ABNEG/SEFF**BC
      XKL=SEFF**BB
      XKV=(1.-SEFF)**2*(1.-SEFF**BA)
      XKAPPAL=SEFF**(5+B)
      XKAPPAV=(1.-SEFF)**3*(1.-SEFF**BD)**2
      FACT=(UN1-UN2*ETA2(I)*(1./XKL+PIGNU/XKV)-
     1UN3*ETA2(I)**2*(1./XKAPPAL+1./PIROVA/XKAPPAV))/PS/COSDEG
      DETA2=DETA2MX
      DS=FACT*DETA2
      IF(ABS(DS).LT.DSMAX) GO TO 22
      DS=DSMAX*FACT/ABS(FACT)*(-1)
      DETA2=DS/FACT
   22 ETA2(I+1)=ETA2(I)+DETA2
      IF(ETA2(I+1).LT.0.) GO TO 24
      S(I+1)=S(I)+DS
      IF(S(I+1).LT.SR) IFLAG=IFLAG*2.
      JJ=I+1
      IF(S(I+1).LT.SR) GO TO 40
   20 CONTINUE
      WRITE(0,203)
  203 FORMAT(1X,'SOMETHING WRONG WITH UNCHANNELED
     1SATURATIONS IN SUBROUTINE PRESSUR')
   24 DETA2=0.-ETA2(I)
      ETA2(I+1)=0.
      DS=FACT*DETA2
      S(I+1)=S(I)+DS
      IF(S(I+1).LT.SR) IFLAG=IFLAG*2
      IF(S(I+1).LT.SR) GO TO 40
      IFLAG=1
      MMAX=I
C
C     INTEGRATION IN UNCHANNELED REGION
C
      DO 30 I=1,MMAX
      SB=(S(I)+S(I+1))/2.
      SEFF=(SB-SR)/(1.-SR)
```

```
      XKL=SEFF**BB
      XKAPPAL=SEFF**(5+B)
      DETA2=ETA2(I+1)-ETA2(I)
      ETA=ETA2(I)+DETA2/2.
      TOTAL=TOTAL-(ETA/XKL+SUB1*ETA**2/XKAPPAL)*DETA2
   30 PIPL(N1+1+I)=PIPLL+PIG*(1.-(ETA+DETA/2.))-TOTAL*SUB2
C
C     THE REASON FOR THE ABOVE MINUS SIGN IS
C     THE DIRECTION OF INTEGRATION
C
C
C     IT IS ASSUMED THAT THE PRESSURE OF INTEREST
C     IS IN A CONCAVE UP REGION OF AT Z=0.  IT IS FURTHER ASSUMED
C     THAT THERE IS AT MOST ONE CONCAVE UP REGION.
C
      NTOT=N1+MMAX+1
      NTOTM1=NTOT-1
      PIPLO=10.**10
      DO 50 I=2,NTOTM1
   50 IF(PIPL(I-1).GT.PIPL(I).AND.PIPL(I+1)
     1.GT.PIPL(I)) PIPLO=PIPL(I)
      PIPLO=PIPL(NTOT)
C     PIPLO=AMIN1(PIPLO,PIPL(NTOT))
C     WRITE(0,200) (PIPL(I),I=1,NTOT)
  200 FORMAT(9F8.0)
   40 J=JJ-10
      WRITE(0,700) (ETA2(I),S(I),I=1,JJ,25)
      WRITE(0,700) (ETA2(I),S(I),I=J,JJ)
  700 FORMAT(10(F4.3,1X,F5.3,2X))
C
      RETURN
      END
```

APPENDIX IV. Dryout Equations for Bottom Heating

In the unchanneled region, equation 2.18 still applies

$$\frac{dS}{dz} = \left(\frac{1}{\frac{dP}{dS}\sqrt{\frac{\varepsilon}{k}}}\right)\left\{\frac{1}{\sigma\cos\theta}\left[(\rho_\ell - \rho_v)g + \frac{1}{k}\left(\frac{\mu_\ell}{k_\ell}q_\ell - \frac{\mu_v}{k_v}q_v\right)\right.\right.$$

$$\left.\left. + \frac{1}{\kappa}\left(\frac{\rho_\ell}{\kappa_\ell}|q_\ell|q_\ell - \frac{\rho_v}{\kappa_v}|q_v|q_v\right)\right] - P\,\frac{d\sqrt{\varepsilon/k}}{dz}\right\} \qquad 2.18$$

The combined energy and continuity equations are

$$q_\ell = \frac{\dot{q}}{\rho_\ell h_{fg}}$$

$$q_v = \frac{\dot{q}}{\rho_v h_{fg}} \qquad A3.1$$

Substituting

$$\frac{dS}{dz} = \left(\frac{1}{\frac{dP}{dS}\sqrt{\varepsilon/k}}\right)\left\{\frac{1}{\sigma\cos\theta}\left[(\rho_\ell - \rho_v)g - \left(\frac{\dot{q}}{k\,h_{fg}}\right)\left(\frac{\nu_\ell}{k_\ell} + \frac{\nu_v}{k}\right)\right.\right.$$

$$\left.\left. - \frac{1}{\kappa}\left(\frac{\dot{q}}{h_{fg}}\right)^2\left(\frac{1}{\rho_\ell\kappa_\ell} + \frac{1}{\rho_v\kappa_v}\right)\right] - P\,\frac{d\sqrt{\varepsilon/k}}{dz}\right\} \qquad A3.2$$

Non-dimensionalizing

$$\frac{dS}{d\eta} = \left(\frac{1}{\frac{dP}{dS}\sqrt{\varepsilon/k}}\right)\left\{\frac{1}{\sigma\cos\theta}\left[\Pi_g\left(1-\Pi_{\rho_v}\right)-\frac{\Pi_{\dot{q}}}{\Pi_k}\left(\frac{1}{k_\ell}+\frac{\Pi_\nu}{k_v}\right)\right.\right.$$

$$\left.\left.-\frac{\Pi_{\dot{q}}}{\Pi_\kappa}\left(\frac{1}{\kappa_\ell}+\frac{1}{\Pi_{\rho_v}\kappa_v}\right)\right]-P\,\frac{d\sqrt{\varepsilon/\Pi_k}}{d\eta}\right\} \qquad \text{A3.3}$$

where

$$\Pi_{\dot{q}} = \frac{\dot{q}\,\nu_\ell}{\sigma\,h_{fg}}$$